JAERI - M
88-101

EXPERIMENTAL STUDY OF ANGULAR NEUTRON FLUX SPECTRA ON A SLAB SURFACE TO ASSESS NUCLEAR DATA AND CALCULATIONAL METHODS FOR A FUSION REACTOR DESIGN

June 1988

Yukio OYAMA

日 本 原 子 力 研 究 所
Japan Atomic Energy Research Institute

JAERI-Mレポートは，日本原子力研究所が不定期に公刊している研究報告書です。
入手の問合わせは，日本原子力研究所技術情報部情報資料課（〒319-11茨城県那珂郡東海村）あて，お申しこしください。なお，このほかに財団法人原子力弘済会資料センター（〒319-11 茨城県那珂郡東海村日本原子力研究所内）で複写による実費頒布をおこなっております。

JAERI-M reports are issued irregularly.
Inquiries about availability of the reports should be addressed to Information Division, Department of Technical Information, Japan Atomic Energy Research Institute, Tokai-mura, Naka-gun, Ibaraki-ken 319-11, Japan.

編集兼発行　日本原子力研究所
印　　刷　㈱原子力資料サービス

JAERI-M 88-101

Experimental Study of Angular Neutron Flux Spectra on a Slab Surface to Assess Nuclear Data and Calculational Methods for a Fusion Reactor Design

Yukio OYAMA

Department of Reactor Engineering
Tokai Research Establishment
Japan Atomic Energy Research Institute
Tokai-mura, Naka-gun, Ibaraki-ken

(Received May 12, 1988)

This paper presents an experimental approach to interpret the results of integral experiments for fusion neutronics research. The measurement is described of the angular neutron flux on a restricted area of slab assemblies with D-T neutron bombardment by using the time-of-flight (TOF) method with an NE213 neutron detector over an energy range from 0.05 to 15 MeV. A two bias scheme was developed to obtain an accurate detection efficiency over a wide energy range. The detector-collimator response function was introduced to define the restricted surface area and to determine the effective measured area.

A series of measurements of the angular neutron flux on slabs of fusion blanket materials, i.e., Be, C, and Li_2O, as functions of neutron leaking angle and slab thickness have been performed to examine neutron transport characteristics in bulk materials. The calculational analyses of the experimental results have been also carried out by using Monte Carlo neutron transport codes, i.e., MORSE-DD and MCNP. The existing nuclear data files, i.e., JENDL-3PR1, -3PR2, ENDF/B-IV and -V were tested by comparing with the experimental results.

From the comparisons, the data on C and ^7Li in the present files are fairly sufficient. Those on beryllium, however, is insufficient for the estimation of high threshold reactions such as tritium production in a fusion reactor blanket design. It is also found that

the total and elastic cross sections are more important for accurate predictions of neutronic parameters at deep position. The comparisons between the measured and calculated results provide information to understand the results of the previous integral experiments for confirmation of accuracy of fusion reactor designs.

Keywords: Angular Neutron Flux, TOF Fusion Blanket Neutronics, DT Neutrons, NE213 Scintillator, MORSE-DD, MCNP, Nuclear Data, JENDL-3PR1, ENDF/B-IV

核融合炉設計に用いる核データ・計算手法評価のための平板体系表面中性子角度束スペクトルの実験的研究

日本原子力研究所東海研究所原子炉工学部
大山　幸夫

（1988年5月12日受理）

本論文は核融合中性子工学研究における積分実験について，そこでこの中性子輸送についてより詳細に調べるための実験的研究について述べたものである。

本研究では，ＤＴ中性子を照射した平板の裏面限定領域から漏洩する中性子角度束を0.05からMeVのエネルギー範囲で測定する方法の開発を行った。この中で，ＮＥ213シンチレータを中性子飛行時間法に用いた時に広範なエネルギー領域にわたって正確な検出器効率を得るため２パイアス法を開発した。また，平板裏面の実効的被測定面積を決定するための検出器・コリメータ応答関数の導入を行なった。

ここで開発した測定系を用いて，核融合ブランケット材料であるＢｅ，Ｃ及びLi_2Oからなる平板体系について中性子角度束スペクトルの測定を漏洩角と体系厚さの関数として行ない，バルク物質体系中での中性子輸送特性を調べた。さらに，これらの測定結果に対してＭＯＲＳＥ－ＤＤとＭＣＮＰによるモンテカルロ計算を行ない，ＪＥＮＤＬ－３ＰＲ１，－３ＰＲ２及びENDF／Ｂ－Ⅳ，－Ⅴの核データを検証した。実験と計算の結果の比較から，現在の核データファイルはＣと^7Liについてはかなり良いが，Ｂｅについては核融合炉設計におけるトリチウム生成率のような高しきい反応の評価には不充分な結果を与えることがわかった。また，体系深層での中性子効果の予測には全断面積と弾性散乱断面積が重要な役割をすることがわかった。

本研究でなされた実験と計算の系統的な比較検討から，核融合炉の設計精度を確認する目的で従来実施されてきた積分実験の結果を説明するための有用な情報を得ることができる。

東海研究所：〒319－11 茨城県那珂郡東海村白方字白根２－４

Contents

目　　次

1. Introduction

1.1 Review and Background of the Present Study

One of the critical issues in the technical development of commercial D-T fusion reactors is the optimization of the nuclear design. The tritium breeding ratio in the breeding blanket should allow tritium self-sufficiency in the overall recovery system.[1] Nuclear heating profiles should be designed to produce efficient electric power generation. The radiation dose must be kept within a limited value for maintenance and safety. These nuclear parameters have been studied so far in a number of conceptual design studies, e.g., UWMAK,[2] FER,[3] INTOR,[4] etc. The optimization of blanket constituents has also been discussed in the BCSS study.[5]

These design studies have been carried out using neutron transport calculation codes, neutron scattering cross sections and response data for neutron parameters. Since the feasibility of a commercial reactor is dependent on its economy and safety, the reliability of the data and the method of neutronic calculations must be established to optimize cost and performance in advance of construction of a demonstration reactor. An example of typical accuracies required for prediction of the nuclear design parameters is listed in Table 1.1, retrieved from reference (6). This table shows only approximate values; other comparisons may indicate somewhat different requirements. The highest accuracies are required for prediction of the tritium breeding ratio and nuclear heating. The required accuracies given in the Table 1.1 are generally comparable with those of cross sections, i.e., considerably smaller than the present status of the calculational predictions.

The sources of uncertainties involved in the calculated result may be listed as follows:

1) Nuclear data:

Evaluated nuclear data of neutron scattering cross sections, energy and angular distributions of emitted neutrons, are used to calculate neutron transport. These include partial cross sections, e.g., (n,n), (n,n'), (n,γ), etc.

2) Response data:

Nuclear heating and radiation damage are calculated from a

kerma (kinetic energy released in matter) factor and an atomic displacement (dpa) cross section. However, the physical processes determining these factors are not well-understood.

3) Methodological deficiency:

Monte Carlo method is the most accurate neutron transport calculational method known at present, but requires a very long computing time to obtain sufficient statistical accuracy for a large system. On the other hand, a deterministic calculation requires a computer whose memory size is large enough for a reactor design calculation. In general, certain mathematical and numerical approximations have to be introduced in either calculational method.

4) Modeling (Simplification of physical conditions):

An actual reactor is constructed of an enormous number of components, including even small bolts and nuts. Since it is evidently impossible to model the system in full detail, simplification is required to carry out a feasible neutron transport calculation.

The above uncertainties involved in calculational procedures have motivated many integral experiments for a bulk system, using 14 MeV fusion neutrons. The integral experiments had the general aim of testing the overall validity of neutronic calculations in various systems that emulate fusion reactor design, and can be classified in three categories:[7]

(i) "Basic Benchmark"; used to test the microscopic data in the evaluated nuclear data files, using a rather simple geometry but including integral effects arising from neutron transport in a bulk material (spectrum change, multiple scattering, etc.). The goal here is to adjust the microscopic data in an evaluated nuclear data file for application to a practical design so as to decrease discrepancies between calculation and measurement,

(ii) "Engineering Benchmark"; used to test the accuracy of calculational predictions for important parameters in blanket/shield designs, e.g., neutron and gamma-radiation spectra, tritium production rate, nuclear heating, radiation dose,...etc. The goal of this type of experiment is to predict the uncertainties in the reactor designs by extrapolation.

(iii) "Mock-up"; used to test the detailed performance and feasibility of specific engineering designs.

The integral experiments reported to date are generally of "basic benchmark" and "engineering benchmark" types. Figure 1.1 shows the relation between experiments and calculational procedures in diagrammatical form. Experimental classes are associated with the importance of each input, e.g., nuclear data file, code and modeling. Thus, the "mock-up" level requires much effort in modeling, while the "basic benchmark" requires for less modeling effort because a simple geometry is used.

Integral experiments for fusion reactor design have been initiated by Spangler[8] at MIT (1965) with a FLIBE blanket test and Wyman[9] at LANL (1958) with a lithium-deuteride sphere experiment. Hansen et al.[10,11] at LLNL have carried out spectrum measurements by the time-of-flight method for spheres of various materials since 1969. Recently they compared their results with Monte Carlo calculations as a test of evaluated nuclear data files. Hiraoka et al.[12,13] at JAERI measured the fission rate distribution in pseudo-spheres of Li, Li-C and U-Li-C in 1973 to 1978. Kappler et al.[14,15] at KFK carried out a series of directional spectrum and tritium production rate (TPR) measurements for a Li-sphere by mean of a re-entrant hole scheme, in 1973 to 1978. In that work, they tried to identify the calculation errors arising from approximations, e.g., simplifications in material distributions, reduction in geometric co-ordinates, discretizations, treatment of anisotropies, description of non-elastic processes, etc., through differences between the measured and calculated results. Herzing et al.[16,17] at Jülich made TPR and spectrum measurements for a cylindrical geometry, using lithium, in 1974 to 1981. These reports commonly concluded that a high S_n (order of angular co-ordinate discretization) and anisotropic treatment of a scattering kernel are necessary for deterministic calculation, to avoid oscillation due to strong anisotropy.

For the above problems of anisotropic treatment of the scattering kernel, Takahashi et al. made the angle-dependent spectrum measurements leaking from Li and C slab assemblies[18,19] in 1977 to 1980 and they proved that the use of a double differential cross section (DDX) representation in the scattering kernel was effective for fusion

neutron transport calculations.[20,21] They also pointed out that the differential cross sections, for non-elastic scattering with respect to the scattering angle and emitted energy of secondary neutrons, were very poorly available in existing evaluated nuclear data files for treatment of anisotropic scattering. Hence, they have emphasized the necessity of the DDX data and moved to the measurements[22] on DDX since 1980.

On the other hand, the precise integral experiments[23-25] have been performed mainly at the FNS in JAERI and the OKTAVIAN in Osaka university in the 1980s. In those experiments, the source neutron characteristics, which one had not previously noted, were precisely determined to compare accurately with the calculated results, and the measurements were carried out with sufficient counting statistics by the intense neutron source. The calculational methods have also progressed for two dimensional codes using the DDX library[26] and Monte Carlo codes[27,28] which are fairly free from a mathematical approximation. These experimental results, however, still showed the discrepancies with the calculations. Some of those discrepancies were ascribed to the cross section, e.g., $^{7}Li(n,n'\alpha t)$, but the others have not been resolved yet for a final goal of the accuracy of $\sim$5 %. Thus, an effort should be required to relate the DDX measurements to the integral experiments.

1.2 Objectives of the Present Study

Most of the previous experiments are in the "basic" and "engineering" benchmark categories. However their discussions on the discrepancies between the experiment and the calculation were not clear because of mixing of the problems associated with nuclear data and methodological deficiency. From this point of view, the followings can be pointed out for those experiments.

1) Neutron source conditions are not well-defined enough to allow a precise calculation for comparison with experiment.
2) The measured quantity do not correspond directly to the calculated one: the experimental arrangement is not appropriate for calculation.
3) The measured values are too heavily compounded by various effects of neutron transport to identify those errors. Hence,

usual cross section sensitivity analysis is not practical.

The previous experiments generally adopted a spherical geometry placing a neutron source at the center, where a simple, one dimensional calculational model is an acceptable first approximation. However, in the spherical system utilizing an accelerator-based neutron source, the neutron interaction with the target assembly should be accounted for. The angular distribution of neutrons emitted from the target is distorted due to scattering on target structure materials. On the other hand, in a neutron current measurement, e.g., Hansen's work[10], the measured flux includes a lot of uncollided neutrons, masking the scattering effect. Also the re-entrant hole experiment as done for fission reactor materials by Profio[29], which measures an in-system neutron angular spectrum, might cause a perturbation effect due to the experimental hole on the actual in-system angular spectrum.

The slab experiment by Takahashi et al. is good to examine the anisotropic scattering. However, the spectrum measured by them corresponds to neutrons emitted from the whole surface of the slab, and the angle-dependent spectrum is affected by the geometrical boundary of the finite-sized slab and the uncollided neutrons directly from the target. Since the measured angle-dependent spectrum does not represent the angular neutron flux, it is difficult to compare accurately with the deterministic transport calculations. In addition, a systematic measurement of angular flux with thickness and angle is necessary to trace the source of discrepancies in the integral experiments, through neutron transport associated with the double differential cross sections.

From these points of view, we will focus our attention on the collided flux and separate the system from the influence of target structure. It is, then, essential to restrict the measured area on the experimental assembly and to locate the assembly far from the target. In addition, for the time-of-flight measurement, time spread due to variation in the emission depth is smaller than that in a sphere. Thus, a slab geometry is the best for those requirements.

Angular neutron flux, i.e., neutron spectrum and angular distribution, are the most basic quantities to understand neutron behavior in a bulk system concerned in nuclear engineering. Especially

in fusion reactor design, the angular distribution of secondary neutrons plays an important role in neutron transport calculations, in contrast to neutron behavior in the fission reactor, because the effect of anisotropic scattering of high-energy neutrons by light nuclei in the blanket materials is emphasized through the directivity of the neutron current from the core plasma to the blanket region.

In the "engineering benchmark" experiments such as Li_2O/Be blanket experiment[24], the results were fully compounded by various parameters in neutron transport over large experimental system. Thus, it is difficult to identify the error sources when the discrepancies between the measured and calculated results are found for those experiments. However, a series of experiments providing a continuous change of phenomena emphasized by from scattering cross section to macroscopic neutron transport, according to penetrating length, would allow us to interpret the discrepancies found in the engineering benchmark experiments. Thus we can feed back the results of those experiments to the individual deficiencies in the calculational procedures.

Consequently, the objectives of the present study are summarized as follows:

1) To develop experimental method to measure neutron angular flux spectra on a slab as functions of leaking angle and slab thickness,
2) To relate the results of comparisons between the measured and calculated results for slabs with nuclear data libraries and calculational methods through the systematics of angle and thickness,
3) To test the validity of the present calculation system for estimation of neutronic parameters, e.g., tritium production, heating, damage, etc, in a fusion reactor design, using Monte Carlo codes and preliminary nuclear data files of JENDL-3.[30]

In the present thesis, the experimental method[31] is described for measuring a neutron angular flux on the restricted area of slab assemblies with D-T neutron bombardment by using the time-of-flight (TOF) method with an NE213 neutron detector over the energy range from 0.05 to 15 MeV. A two-bias TOF scheme has been proposed to deal with problems associated with detector efficiency determination. The

detection efficiency was examined by a neutron field from a graphite pile with a D-T source.[32] The detector-collimator response function was introduced to define the angular flux and examined in detail by the experiment.

We performed experiments with slabs of fusion blanket materials, i.e., graphite, beryllium and lithium-oxide, of thicknesses 0.5-5 mfp (mean free path), at five leaking angles.[33,34] The experimental results were analyzed by the calculation using the evaluated nuclear data files, e.g.,the preliminary versions of JENDL-3, ENDF/B-IV and -V[35]. The Monte Carlo codes, MORSE-DD[27] and MCNP[28] were adopted to precisely simulate the experimental arrangement and to test the validity of the nuclear data libraries and the transport codes directly by excluding modeling uncertainty. Then the systematics of the discrepancies between the measured and the calculated results were examined and discussed.

References

1) Abdou M. A., et al.: Fusion Technol., 9, 250 (1986)
2) Badger B., et al.: " UWMAK-I, A Wisconsin Toroidal Fusion Reactor Design," UWFDM-68, University of Wisconsin (1974)
3) Sako K., et al.: "Conceptual Design of a Gas-Cooled Tokamak Reactor," Nucl. Fusion, Special Suppl., Fusion Reactor Design Problems, 27 (1974); JAERI-M 5502(1973); JAERI-M 7300 (1977) (in Japanese)
4) INTOR group: "International Tokamak Reactor : Phase One," Proc. Report Int. Tokamak Reactor Workshop, STI/PUB/619, International Atomic Energy Agency, Vienna (1982); See also Nucl. Fusion, 22 135 (1982)
5) Smith D. L., et al.: Fusion Technol., 8 ,p.1-162 (1985)
6) Abdou M. A., et al.: "Technical Issues and Requirements of Experiments and Facilities for Fusion Nuclear Technology; FINESSE Phase I Report," UCLA-ENG-85-39, University of California, Los Angeles (1985)
7) Oyama Y., et al.:"Neutronics Tests," Chapter 7 in the report, "FINESSE-A Study of the Issues, Experiments and Facilities for Fusion Nuclear Technology Research & Development (Interim Report)," editted by Abdou M. A., UCLA-ENG-84-30 (1984)

8) Spangler P. S.: "Fusion Reactor Blanket Experiment," Technical Report 437, Research Laboratory of Electronics, M.I.T. (1965)

9) Wyman M. E.: "An Integral Experiment to Measure the Tritium Production from ^{7}Li by 14-MeV Neutrons in a Lithium-Deuteride Sphere," USAEC Report LA-2234 (rev.) (1972). (Originally published in 1958)

10) Hansen L. F., et al.: "Summary of Measurements and Calculations of Neutron and Gamma-Ray Emission Spectra from Spheres Pulsed with 14-MeV Neutron," UCID-19604 (1982)

11) Wong C., et al.: "Livermore Pulsed Sphere Program; Program Summary through July 1971," UCRL-551144, Rev.I (1972)

12) Hiraoka T., et al.: "Integral Experiments on a Spherical Lithium Metal Blanket System," Proc. Symp. Fusion Reactor Design Problem, CONF-740131, pp363-3876, IAEA (1974)

13) Maekawa H., et al.: J. Nucl. Sci. Technol., 14 , 87 (1977), ibid. 16 , 377 (1979)

14) Kappler F. K., et al.: Nucl. Instr. Meth., 111 , 83 (1973)

15) Backmann H., et al.: Nucl. Sci. Eng., 67 , 74 (1978)

16) Herzing R., et al.: ibid. 60 169 (1976); ibid., 63, 341 (1977)

17) Kuyjper L., et al.: Nucl. Instr. Meth., 144, 215 (1977)

18) Takahashi A., et al.: J. Nucl. Sci. Technol., 14, 308 (1977)

19) Yamamoto J., et al.: ibid., 17, 255 (1980)

20) Takahashi A., et al.,: ibid.,16, 1 (1979)

21) Yamamoto J., et al.,: ibid., 19, 276 (1982)

22) Takahashi A., et al.,: ibid., 21, 577 (1984)

23) Maekawa H., et al.,:" Measurement of Tritium Production-Rate Distribution in a 60 cm-Thick Li_2O Slab Assembly and Its Analysis", Proc. 7th Topical Meeting on the Technology of Fusion Energy, Reno, Nevada, June 15-19, 1986, Fusion Technol., 10, 1460 (1986)

24) Nakamura T. and Abdou M.A.: "Summary of Recent Results for JAERI/US Neutronics Phase I Experiment," , ibid., 10, 541 (1986); and Trans. Am. Nucl. Soc., 52, 106 (1986)

25) Sugiyama K., et al.,: " Integral Experiments in a 120 cm Lithium Sphere," ibid., 10, 1491 (1986)

26) Suzuki T., et al.: "BERMUDA-2DN: A Two-Dimensional Neutron Transport Code," JAERI-M 82-190 (1982) (in Japanese); Proc. 6th Int. Conf. on Radiation Shielding, Tokyo, May 16-20, p.246 (1983)

27) Nakagawa M. and Mori T.: "MORSE-DD, A Monte Carlo Code Using Multi-Group Double Differential Form Cross Section," JAERI-M 84-126 (1984)

28) Los Alamos Radiation Transport Group (X-6): "MCNP-A General Monte Carlo Code for Neutron and Photon Transport," LA-7396-M,(1981)

29) Profio A.E., Anturez H.M., Huffman D.L.: Nucl. Sci. Eng., 35, 91 (1969)

30) Shibata K. and Kikuchi Y.: "Evaluation of Nuclear Data for Fusion Neutronics," Proc. Int. Conf. Nuclear Data for Basic and Applied Science, Santa Fe, New Mexico, May 13-17, 1985

31) Oyama Y. and Maekawa H.: Nucl. Instr. Meth., A245, 173 (1986)

32) Oyama Y., et al.: "Modification of the Time-of-Flight System for Extending to Lower Energy Range," JAERI-M 86-125, p.124(1986)

33) Oyama Y. and Maekawa H.: Nucl. Sci. Eng., 97, 220 (1987)

34) Oyama Y., Yamaguchi S. and Maekawa H.: to be published in J. Nucl. Sci. Technol.

35) ENDF/B Summary Documentation: BNL-NCS-17541 (ENDF-201), 2nd Edition, compiled by D. Garber (1975)

Table 1.1 Required accuracies and present status of prediction error in nuclear design of fusion reactor[16].

Location/Response	Required Accuracy	Present Status
First Wall/Divertor		
Nuclear heating	Total 2%, local 10%	50%
Atomic displacement	10%	
Gas production	10%	
Transmutation	20%	
Induced activity	30%	50% ~ factor 3
Blanket		
Tritium production rate	gross 3 ~ 5%, local 10%	Gross 10%, local 20%
Nuclear heating	20%	
DPA	20%	
Gas production	20%	
Induced activity	50%	factor 2 ~ 5
Bulk Shield		
Nuclear heating	20%	factor 2 ~ 5
DPA	30%	
Induced activity	factor 2	factor 5 ~ 10
Superconductive Magnet		
Nuclear heating	gross 30%, local 50%	factor 5 ~ 10
DPA	gross 30%, local 50%	
Gas production	gross 50%, factor 2	
Dose	gross 30%, local 50%	
Induced activity	factor 2	
Penetration Functional Equipment (e.g. vacuum, pump, RF, and NBI)		
Nuclear heating	gross 30%, local 50%	gross factor 2, local factor 10
DPA and gas production	50%	
Induced activity	factor 2	
Reactor Room (outside the shield and inside the reactor bldg.)		
Biological dose during operation	factor 3	
Biological dose after shutdown	factor 2	
External Biological Dose (outside plant site)	factor 3	

* Assumed DEMO class reactor

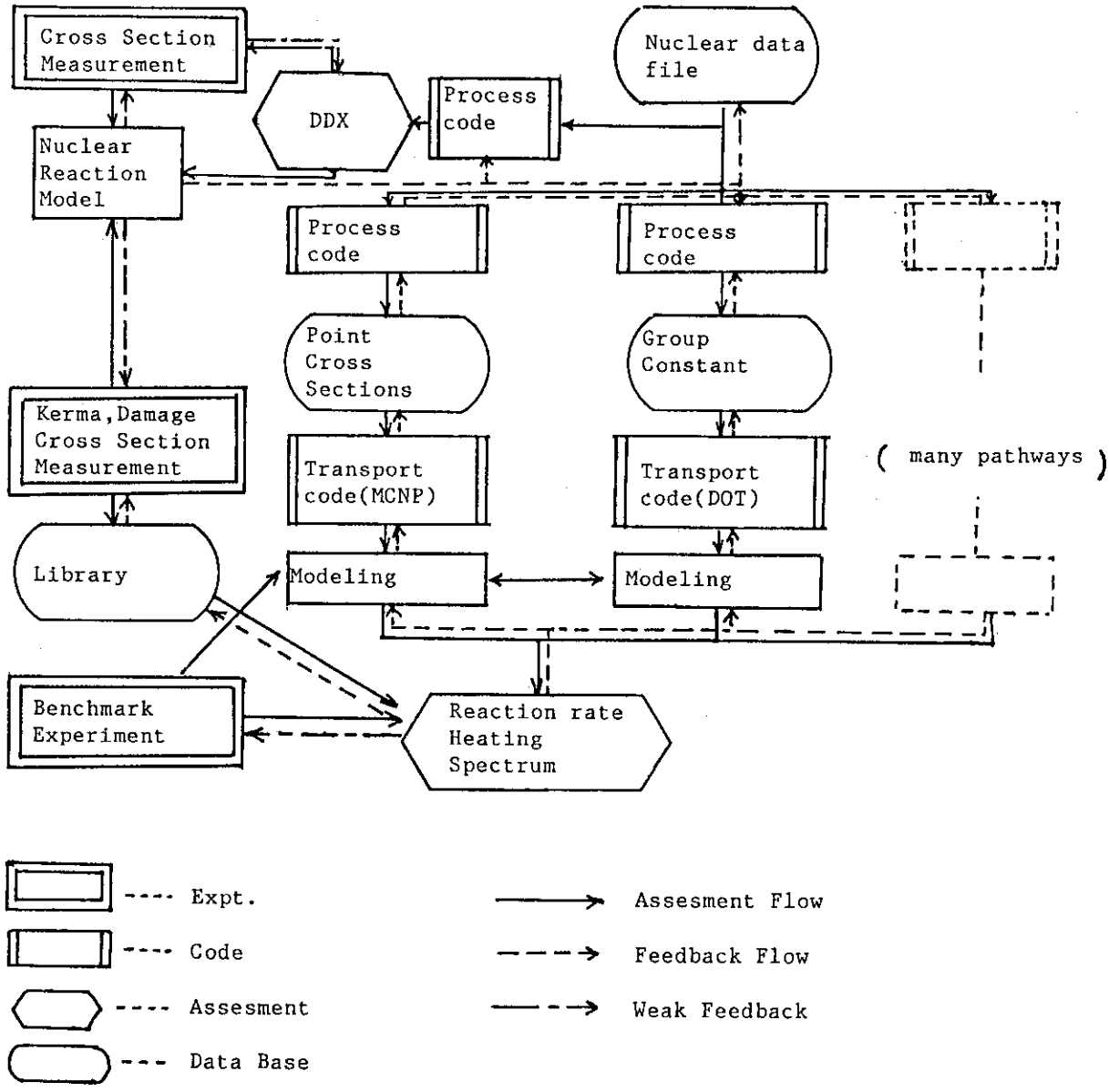

Fig. 1.1 Relation between experiment and calculation in an assessment of fusion neutronic calculation.

2. Characteristics of the Angular Neutron Flux on the Slab Surface

2.1 Introduction

Angular flux at the center of the rear surface of a slab material bombarded by a DT neutron source isolated from the assembly is a relevant quantity to be measured. Composition of that angular flux is related to neutron behavior in the slab.

From time-independent transport theory, the angular flux ϕ is given by a solution of the following equation:

$$\Delta\phi + \sum\phi = \iint dE'd\Omega'\ \phi(\mathbf{r}, E, \Omega) \sum_s(E'\Omega' \rightarrow E\ \Omega) + S, \qquad (2.1.1)$$

where Δ : Laplace operator,
$\sum$: Macroscopic total cross section,
$\sum_s$: Macroscopic scattering cross section,
S : Intensity of neutron source.

The neutron flux $\phi(\mathbf{r}, E, \Omega)$ appearing in Eq. (2.1.1) can be expressed as an integral:

$$\phi(\mathbf{r}, E, \Omega) = \int_0^\infty ds\ \exp(-\sum s)\ Q\ (\mathbf{r}-s\Omega, E, \Omega), \qquad (2.1.2)$$

where $Q(\mathbf{r}-s\Omega, E, \Omega) = \iint dE'd\Omega'\ \phi(\mathbf{r}-s\Omega, E', \Omega') \sum_s(E'\Omega' \rightarrow E\Omega) + S(\mathbf{r}-s\Omega, E, \Omega).$ (2.1.3)

The quantity Q $(\mathbf{r}-s\Omega, E, \Omega)$ represents neutrons starting at $(\mathbf{r}-s\Omega)$ in a direction Ω and with energy E as shown in Fig. 2.1, and the factor $\exp(-\sum s)$ is the probability that those neutrons arrive at the point $\mathbf{r}$ without collision. From equation (2.1.2), it is clear that the angular flux at the surface includes contributions of the in-system flux.

For a thin slab, the in-system angular flux is almost an uncollided flux from the source; the angular flux at the surface is obtained mainly from a macroscopic double differential emission cross section (DDX). For a thick assembly, on the other hand, the angular flux at the surface involves the integration of the term Q along the

line s. Since the term Q is integrated with angle and energy, the angular flux includes neutron information from the entire assembly. Thus, the angular flux at the center of the rear surface is a good probe for internal neutron behavior.

In the next section, changes in the spectrum of angular flux with increase of thickness, and relation of the angular flux to the internal flux, are discussed on the basis of neutron transport calculations.

2.2 Dependence of Spectrum Characteristics on Slab Thickness

The angular flux energy spectrum is related to the macroscopic total cross sections for slab materials. In particular, for a thin slab, the angular flux corresponds directly to secondary neutron emission spectra by the primary reaction as seen in the equation (2.1.2), where most of the internal scalar flux is composed of the uncollided source neutrons. In order to examine the validity of the direct relation of the angular flux to the cross sections for the thin slab case ($\sim$1 mean free path for the incident neutrons), two spectra for 5-cm thick slabs, with the ordinary and 1/10 densities, were calculated and compared. Spectra for the dilute slab is assumed to consist of singly-scattered neutrons.

Calculations were performed by a Monte Carlo neutron transport code[1], as described in the chapter 4. A typical comparison of spectra for the 5 cm-thick graphite assembly is shown in Fig. 2.2.1. Above 0.5 MeV, the spectrum for the ordinary density is very similar to the dilute case. Figures 2.2.2 - 2.2.4 show the ratio between the two cases for various angles and materials. The ratio has to be 0.1 due to the density factor when the material is same. Ratios above 0.5 MeV come to about 0.1, while the ratios below 0.5 MeV deviate from the single-scattering limit. Moreover, the deviations increase with angle, as the effective neutron flight length also increases with angle. The beryllium case, however, is slightly different due to the (n,2n) reaction, resulting in spectrum deviating from the single-scattered one even in the energy range above 0.5 MeV.

The above feature for a thin slab allows us to discuss the angular flux spectra above 0.5 MeV in relation to the secondary emission spectra caused by reactions with incident DT neutrons, while

the consideration of multiple scattering is required to interpret the spectrum below 0.5 MeV.

Increasing the slab thickness affects the integration of both the transmission factor in equation (2.1.2) and the term Q. Since the angular flux is obtained from the term Q by summing the scattering cross sections, weighted by the internal angular flux in the slab as well as from the factor $\exp(-\sum s)$, the leakage flux represents the secondary emission spectra from a region of some depth, where the spectrum is changed by multiple scattering. Therefore, a thick-slab measurement provides a test of cross sections for lower energy neutrons. As an example, figure 2.2.5 shows the spectrum ratio between 5 cm and 20 cm thick slabs of graphite. Since the spectrum is considerably modified by the slab, thick slabs can be effectively divided into two zones: a frontal zone working as a spectrum shifter and a rear zone that provides a testing region of the nuclear data in broad energy range.

2.3 Relation of the Angular Flux to the Internal Neutrons of the Slab

The angular flux leaking from the slab is composed of internal neutrons reaching the surface through various pathways. Hence, this angular flux samples the internal neutron flux distributed throughout the slab. In order to examine the relation of the angular flux to the local internal neutron flux, the contribution flux distributions[2] were calculated by the VIPS code, modified from the VIP[3] code for two-dimensional cross section sensitivity analysis with the neutron transport code DOT3.5[4].

The contribution flux $<\phi\phi^*>$ is the product of forward and adjoint fluxes,

$$<\phi\phi^*> = \int_{\text{mesh}} dv \int_{4\pi} d\Omega\ \phi(E,\Omega,r)\phi^*(E,\Omega,r) \quad . \tag{2.3.1}$$

The adjoint flux signifies the probability with which the detector detects neutrons at the point r and the forward flux signifies the probability for neutrons to reach the point r from the source. Thus, the contribution flux represents the relative importance of the space in the vicinity of point r, for specific source and detector

configuration. If the angular flux within the energy window from E to E+ΔE is considered as the detector response, the contribution spectra for this energy region can be obtained in the same manner. In the present calculation, the 32 group cross section set FSX32[5] and three detector response functions were used, as shown in Table 2.3.1. The calculational model and procedure are shown in Figs. 2.3.1 and 2.3.2.

The results for the three responses, at 12.2 and 66.8 degrees for the graphite, are presented by contour maps of the total contribution, as shown in Figs. 2.3.3-2.3.4. In Fig.2.3.3, the contribution to high energy spectrum distributes along the detector angle, and expands to a whole slab with decreasing the response energy.

From the figures 2.3.3 and 2.3.4, corresponding to the co ntribution distribution for th fluxes at 12.2 and 66.8 degrees, it is seen that the contribution flux distributions for both angles come to be similar for the lower energy response. This suggest that the angular flux in the low energy will show an isotropic dependence. On the other hand, the angular flux above 4.2 MeV show large contribution along the leak angle. Since a neutron traveling length is larger for neutrons leaking with large angle, the angular flux at large angle is attenuated and then decreased with increasing the angle.

Figure 2.3.5 shows the contribution distribution at 66.8 degrees for the beryllium slab. In this case, the contribution for the high energy response is expanded to the front side more than that of the graphite case. Thus, anisotropy of the angular flux will be smaller than that of the graphite. In addition, the large contribution of the front side indicates that the thickness dependence of the angular flux is small.

2.4 Conclusion

The angular flux leaking from the center of slab can provide much information on double differential cross sections (DDX) for a wide energy range by varying the slab thickness. Specifically, for a thin slab, the angular flux corresponds directly to the DDX. On the other hand, the angular flux is associated with the internal scalar flux relating to the reaction rates and the tritium production rate. These two features make it easy to understand the integral properties, spectrum change and multiple scattering, of neutron transport in a

bulk material.

The angular flux for the graphite reflects the internal flux of the region corresponding to the leaking angle, while the angular flux for materials that feature a break-up reaction, e.g., (n,2n), emphasizes scattering in the front zone. These relations of the angular flux to the internal flux can thus help us to understand the previous integral experiments which measured reaction rates and in-system scalar flux[6].

References

1) Los Alamos Radiation Transport Group (X-6): "MCNP-A General Monte Carlo Code for Neutron and Photon Transport," LA-7396-M, (1981)
2) Williams M. L., Engle Jr. W. W.: Nucl. Sci. Eng. 62, 92 (1977)
3) Childs R. L., Bartine D. E., Engle Jr. W. W.: Trans. Am. Nucl. Soc., 21, 542 (1975)
4) Rhoades W. A., and Mynatt F. R.:"The DOT-III Two Dimensional Discrete Ordinates Transport Code," ORNL/TM-4280, Oak Ridge National Laboratory (1973)
5) Kosako K.: private communication (1987)
6) Maekawa H., et al.: "Fusion Blanket Benchmark Experiments on a 60 cm-Thick Lithium-Oxide Cylindrical Assembly," JAERI-M 86-182 (1986)

Table 2.3.1 Source and detector conditions for calculation of contribution flux. Detector responses with three energy windows are taken into the calculation for two angle windows.

	Group No.	Energy range	Angle range
Resp.1	1- 4	13.7-16.5 MeV	7.1-16.8 degrees or 61.8-71.8 degrees
Resp.2	9-11	4.2-10 MeV	
Resp.3	14-17	140-930 KeV	
Source	2	14.6-15.5 MeV	isotropic

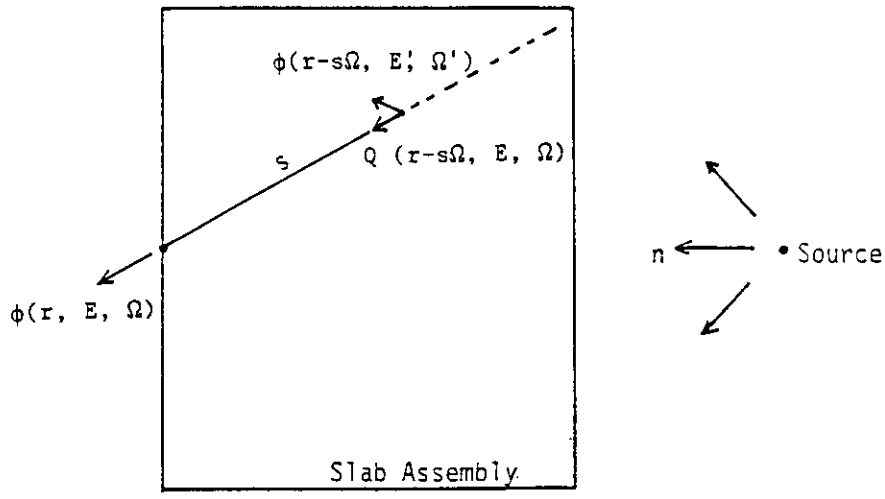

$$\phi(r, E, \Omega) = \int_0^\infty ds \exp(-\Sigma s)\, Q\,(r-s\Omega, E, \Omega),$$

$$Q(r-s\Omega, E, \Omega) = \iint dE'd\Omega'\ \phi(r-s\Omega, E; \Omega')\ \Sigma_s(E'\Omega' \to E\Omega) + S(r-s\Omega, E, \Omega)$$

Fig. 2.1.1 Relation of the angualr flux on the face to the internal neutron flux.

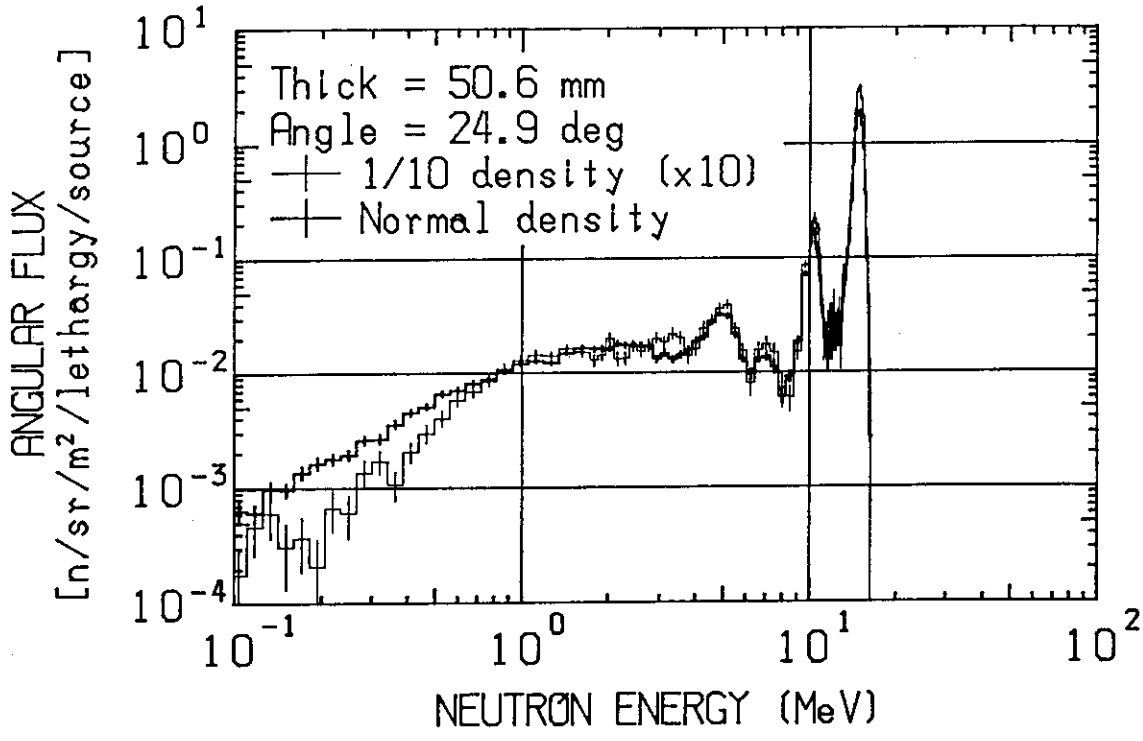

Fig. 2.2.1 Comparison of the spectra from the slabs with normal density graphite and 1/10 dilute graphite.

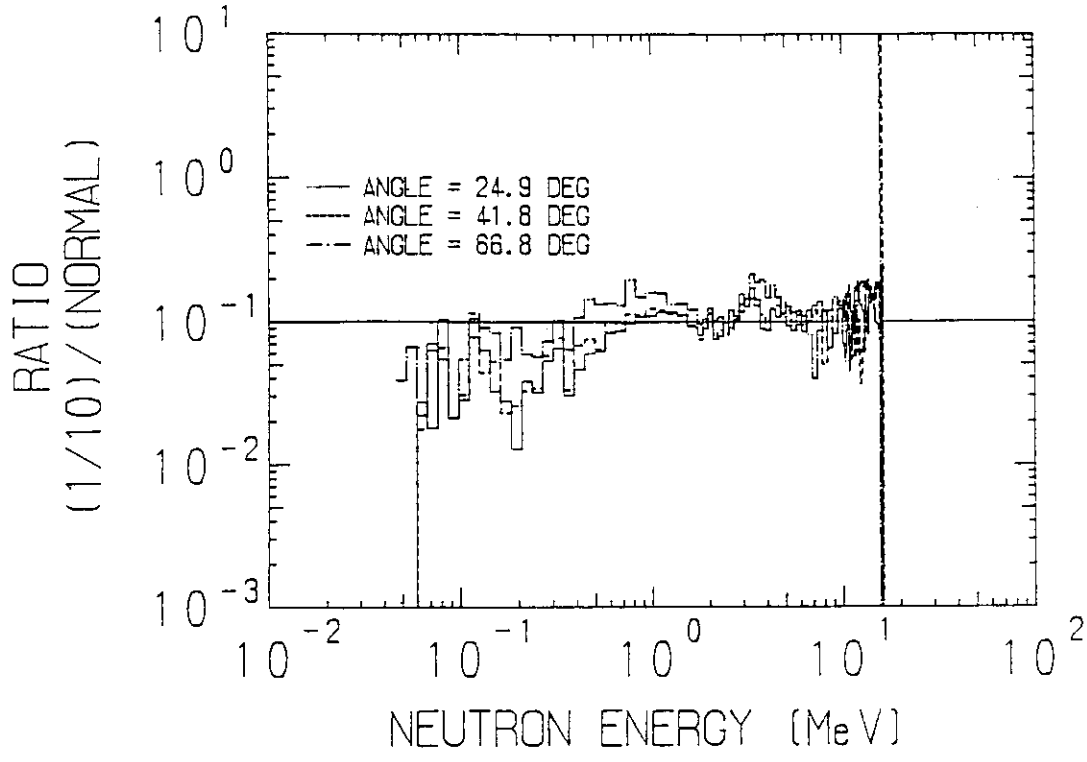

Fig. 2.2.2 Ratios of the spectra from the dilute slab to the normal density for the 5 cm-thick graphite slab.

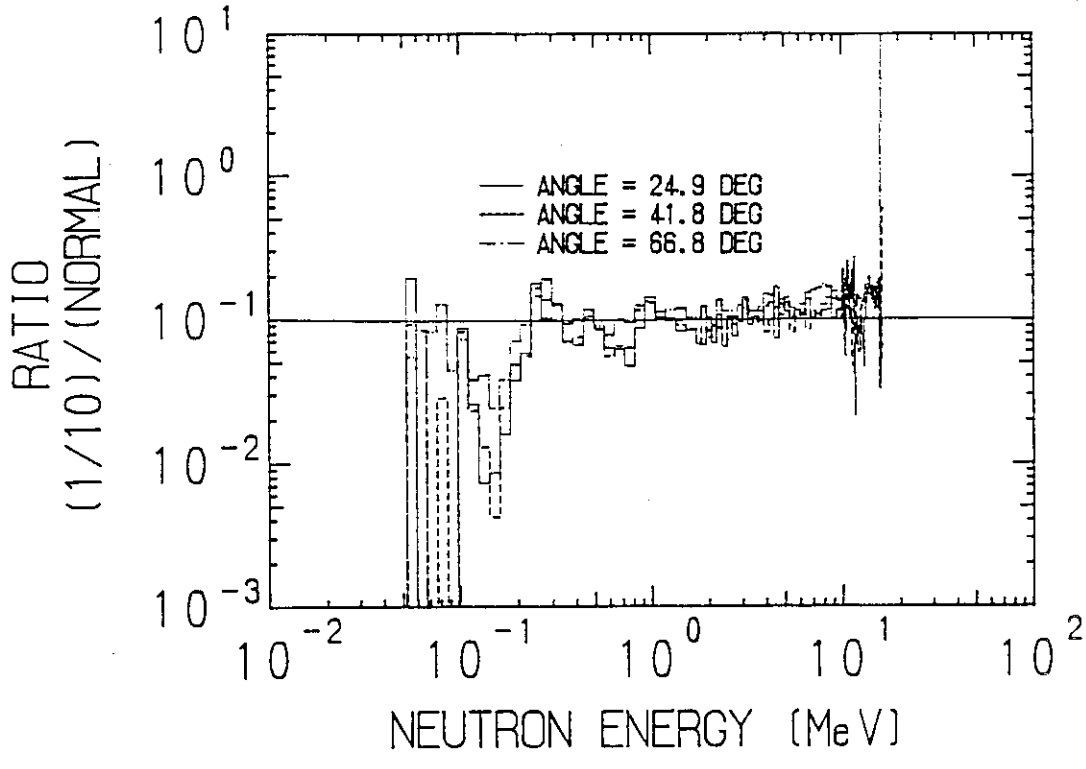

Fig. 2.2.3 Ratios of the spectra from the dilute slab to the normal density for the 4.8 cm-thick lithium-oxide slab.

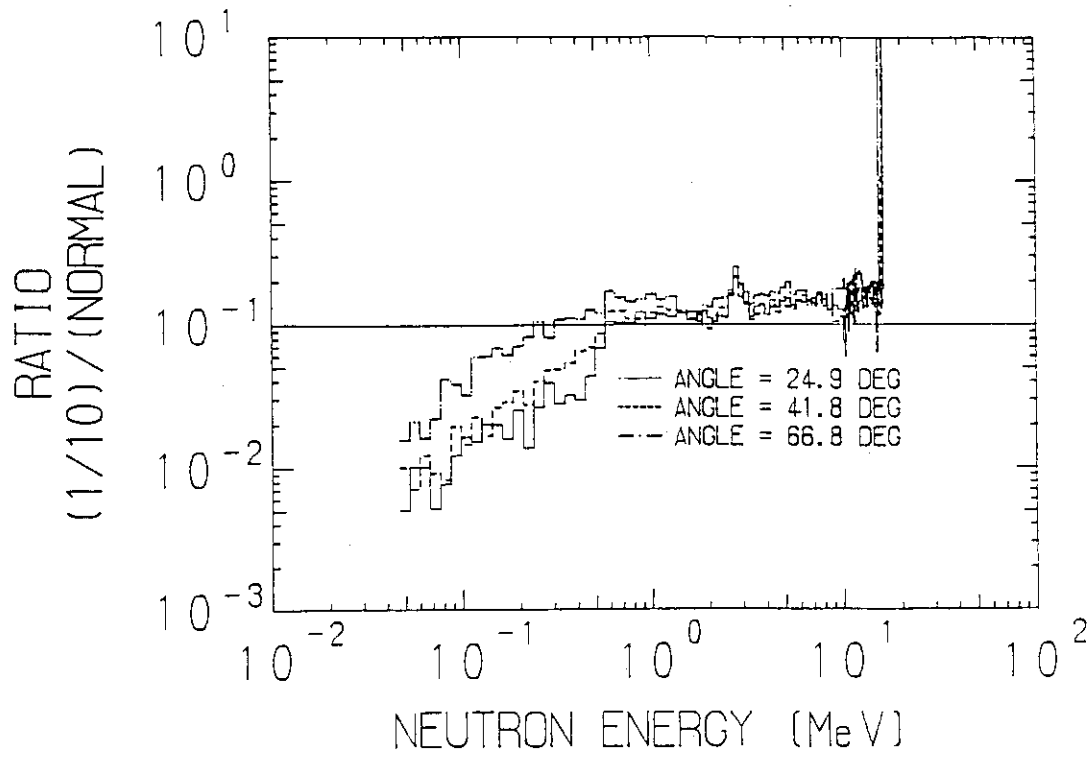

Fig. 2.2.4 Ratios of the spectra from the dilute slab to the normal density for the 5 cm-thick beryllium slab.

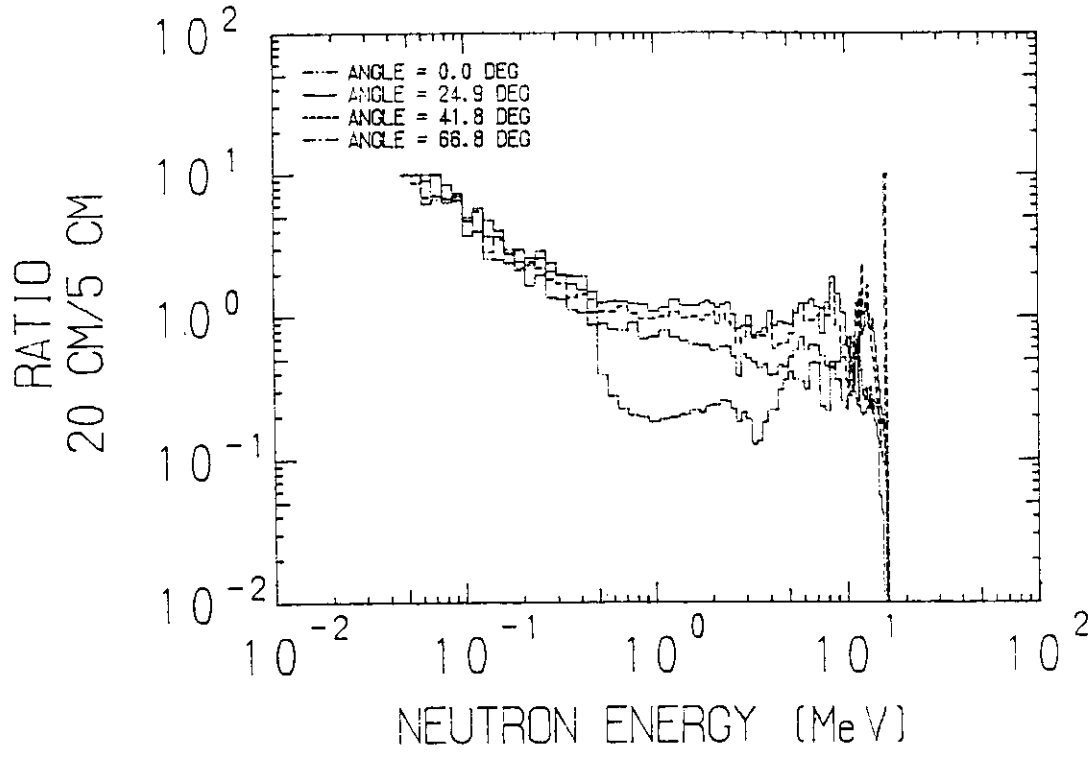

Fig. 2.2.5 Spectral change of the angular flux between the 5 cm- and 20 cm-thick slabs.

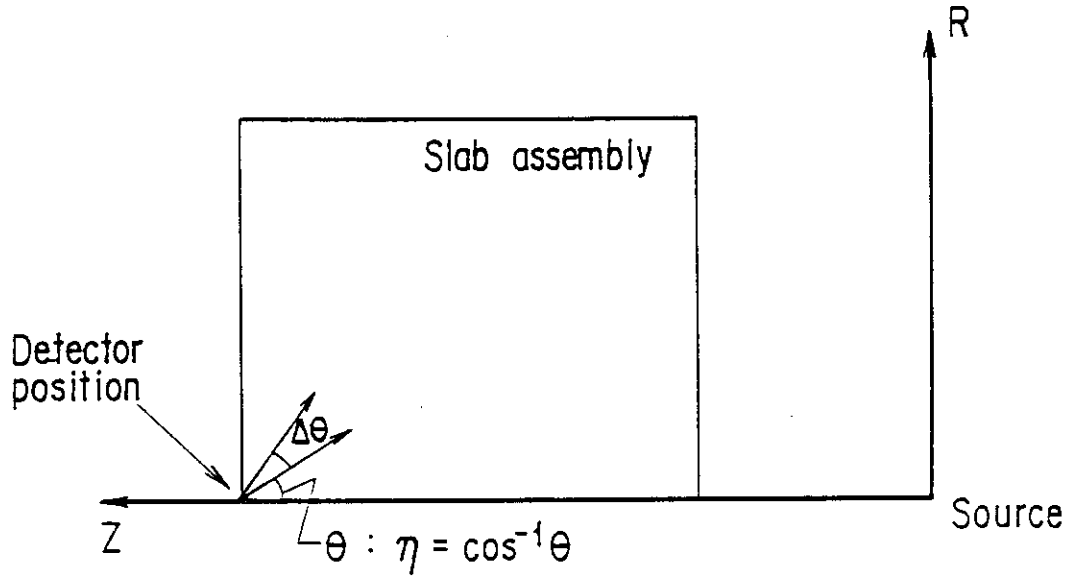

Fig. 2.3.1 Two-dimensional model for contribution flux calculation.

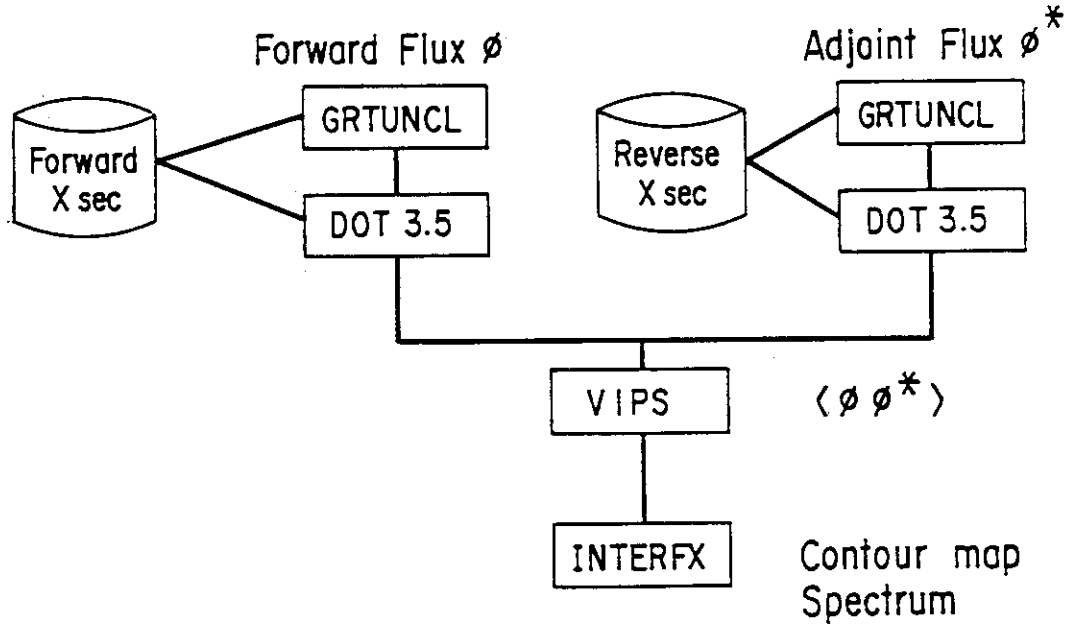

Fig. 2.3.2 Calculational procedures.

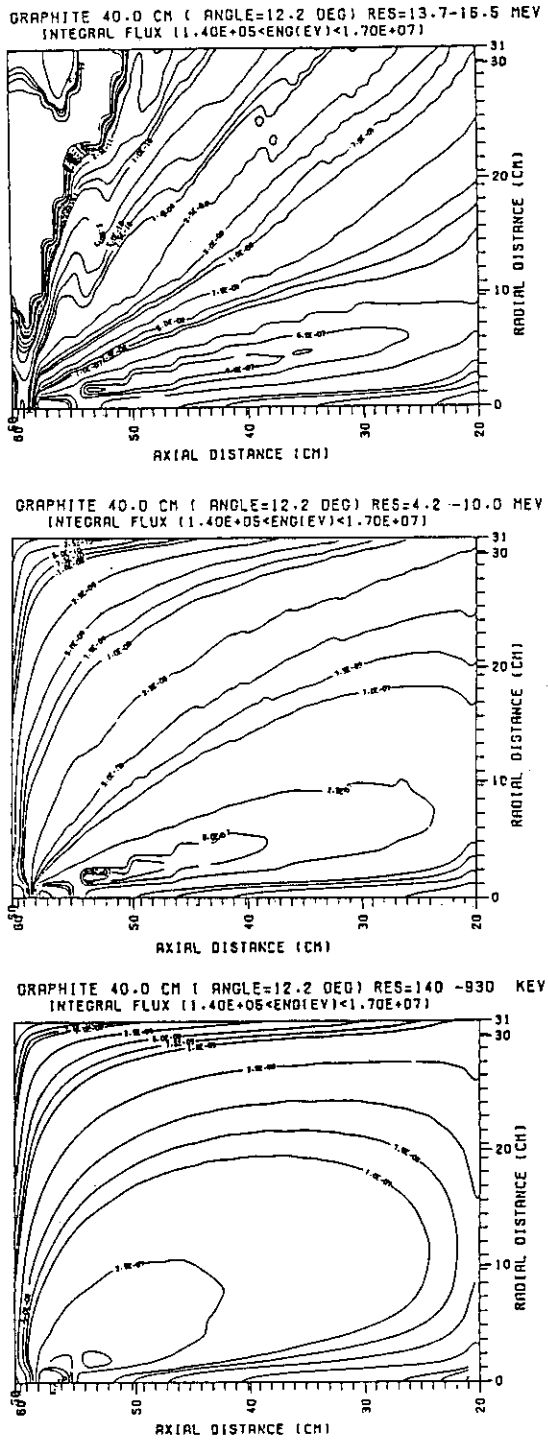

Fig. 2.3.3 Contour maps of the total contribution flux distributions in a graphite slab for the response with the angle window of 7.1-16.8 degrees.
(a) Contribution distributions for the detector with the energy response of 13.7-16.5 MeV, (b) 4.2-10 MeV, (c) 140-930 keV.

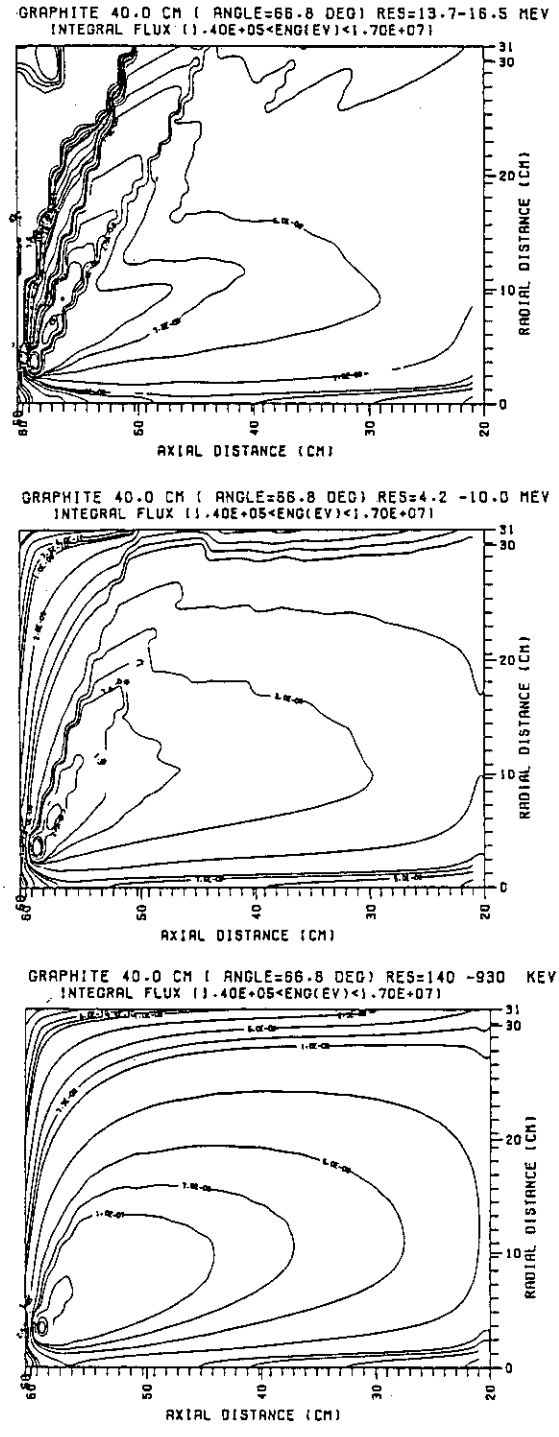

Fig. 2.3.4 Contour maps of contribution flux distributions on graphite slab for the response with the angle window of 61.8-71.8 degrees.
(a) Contribution distributions for the detector with the energy response of 13.7-16.5 MeV, (b) 4.2-10 MeV, (c) 140-930 keV.

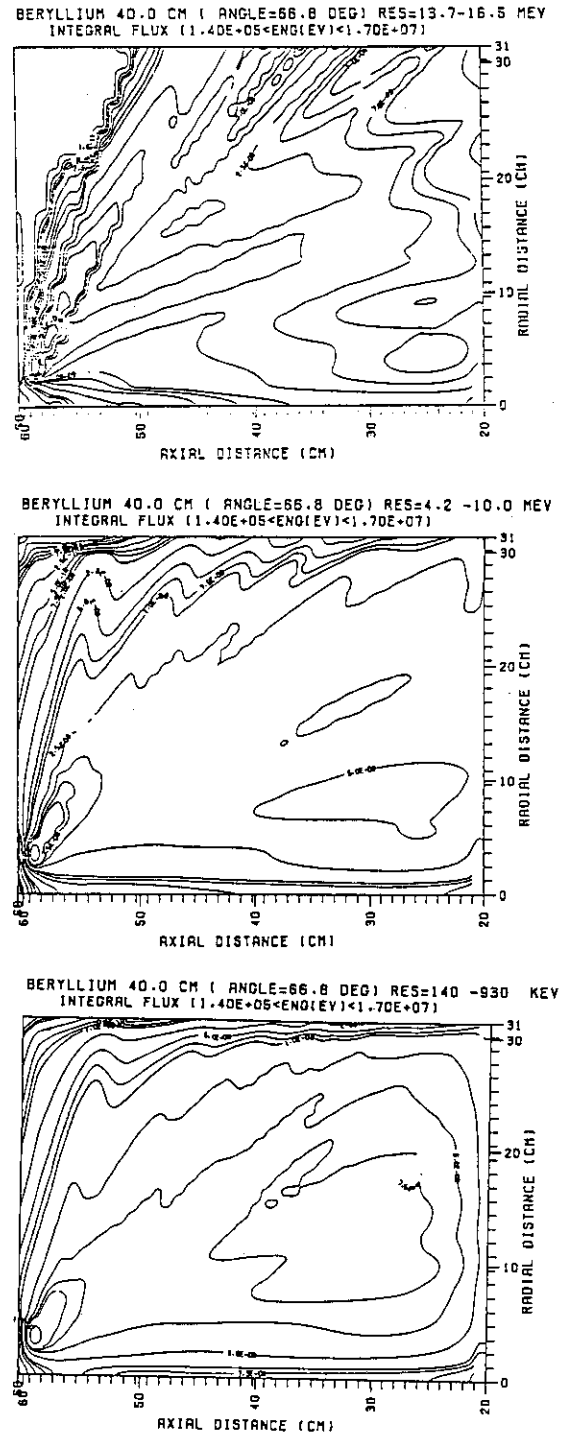

Fig. 2.3.5 Contour maps of contribution flux distributions on beryllium slab for the response with the angle window of 61.8-71.8 degrees.
(a) Contribution distributions for the detector with the energy response of 13.7-16.5 MeV, (b) 4.2-10 MeV, (c) 140-930 keV.

3. Development of a Method for Measuring Angular Neutron Flux Spectra from Restricted Surface of a Slab

3.1 Introduction

To obtain an angular flux spectrum from the restricted area on the rear surface of slab, there are two main problems:(1) measurement of energy spectra from the thick slab assembly and (2) determination of the restricted area. the measurement of neutron energy spectrum is performed by the ordinary time-of-flight technique using an NE213 scintillation detector. However, the method to obtain accurately neutron spectra in a wide energy range from 15 MeV to below 100 keV should be developed for a fusion neutron experiment. The restricted area is defined by the collimator-detector system and it is replaced by the effective measured area for data reduction.

The experimental setup involves the design of assembly, collimator, neutron source, detector and shield. The detecting system includes signal processing scheme and efficiency calibration. The measured data are reduced to angular flux by various corrections, e.g., air attenuation, solid angle, background, neutron yield, etc.

In the present study, a new TOF detector system, using an NE213 scintillator, has been developed to yield measurements over a wide energy range,[1)] covering 50 keV to 15 MeV in a single run. The effective measured area is used to obtain 'angular neutron flux' from 'angular neutron current'. That area is estimated by introducing the detector-collimator response function. The background was examined in detail to obtain improved shielding, hence, a better signal-to-background ratio.[1)]

3.2 Experimental Arrangement

For a direct comparison of measurement with the calculation by deterministic method, it is essential to adopt a slab assembly, because it is the only simple arrangement to measure an angular neutron flux from the restricted area on the rear surface of slab. In contrast, a sphere assembly features a shadow contribution in a directional leakage measurement on a finite surface area. The slab

arrangement allows one to isolate the assembly from the neutron generating target (whose structure affects the measurement by neutron scattering in the arrangement that the neutron target is surrounded by the experimental assembly).

To simplify a calculational model, the slab assembly was made in pseudo-cylindrical configuration; this system can be accurately represented by a two-dimensional code. The pseudo-cylinder was made from blocks of a standard size of 50.6 mm side length as shown in Fig. 3.2.1, supported by square aluminum tubes of 50.8 mm unit size. The assembly was placed at a distance of 0.2 m from the neutron source. Figure 3.2.2 shows the experimental layout in the target room. The radius of the assembly was 0.314 m, corresponding to 5 - 6 mean free paths for 14 MeV neutrons, such that the neutron flux attenuates to 1 % in passing through the material. The boundary of the pseudo-cylinder can, thus, be approximated by a true circle in the calculational analysis.

The neutron angular flux was defined by the area and the solid angle which was determined by the detector-collimator system. Since the measured area for the emitted neutrons is of finite size, the measured angular flux is an average over the area, which was designed to be 0.05 m in diameter by selecting the detector size and the collimator opening, so that the averaged flux, i.e., the measured flux, was less than the flux at the center by only a few % from a calculational estimation.[2)]

The dual rotating deck, consisting of an upper and a lower deck, was designed to perform the experiments on different thick samples. The detector-collimator system was placed on this deck. The lower deck moves around the neutron source and points to the target, and then the upper deck rotates slightly on the lower deck to adjust the axis to the measured direction. The detector-collimator axis can be adjusted to any point near the neutron source by these two motions. This mechanism allows measurement for assembly thickness of more than 1 m. A shadow-shield made of 0.4 m-thick iron blocks was provided to prevent direct neutrons entering the collimator entrance and the detector.

The 14 MeV DT neutrons were generated at a 10 Ci (3.7×10^2 GBq) tritium-metal target. The tritium was adsorbed in a 40 g/m^2-thick

titanium layer evaporated on a 1 mm-thick copper backing. Neutrons were produced by the reaction

$$d + {}^{3}H \rightarrow {}^{4}He + n + 17.6\ MeV. \qquad (3.2.1)$$

Deuteron beams were accelerated to 350 keV by the electrostatic accelerator of the FNS (Fusion Neutronics Source) facility at JAERI.[3] Figure 3.2.3 shows the accelerator and the beam line systems. A pulsed deuteron beam of 2 ns width (FWHM) was employed in the time-of-flight measurement, using the 80 degree beam line. The beam pulsing was accomplished by four pulsing devices, i.e., sweeper, diverter, post-acceleration deflector and buncher, as shown in the block diagram of Fig. 3.2.4. A singly-charged deuteron beam was selected by a 90° bending magnet. Then, the deuteron beam was chopped by the sweeper and the deflector within the high voltage cage by a 2 MH_z master oscillator, reshaped by the post-deflector after acceleration and shortened to 2 ns in a 10 m-drift tube by the two-gap buncher. Thus, the DC beam of 2 mA was bunched to a peak current of more than 35 mA at the target. The tritium target was attached to the bottom of the Farady cup and cooled by compressed air flow as shown in Fig. 3.2.5. The neutron spectrum obtained from the target is shown in Fig. 3.2.6. The angular distribution of neutron emitted from that target is also shown in Fig. 3.2.7. Forward neutron emission is fairly isotropic, even though emission at 90 degrees is strongly distorted by scattering on the structure materials.

The neutron yield at the target was monitored by detecting the associated alpha particles.[4] This monitoring method was chosen to make the yield measurement independent of the used assembly size, which gives different neutron yields for any external arrangements of a neutron detector. Figure 3.2.8 shows the alpha detector arrangement. A silicon surface-barrier detector (SSD) was used for alpha particle detection. A thin aluminum foil of 4.1 g/m^2 was inserted to separate the alphas in the detector response from other particles, such as, protons from the $^{3}He(d,p)^{4}He$ reaction and from the $D(d,p)^{3}T$ reaction (Here, ^{3}He is formed by β-decay of ^{3}T in the target, and deuterium is absorbed) as shown in Fig. 3.2.9.

The conversion factor of alpha counts to total neutron yield was calculated from kinematics considering slowing-down of deuterons in the titanium-tritium layer.[5] The error in absolute yield was estimated to be ±2 %.

3.3 Development of a Time-of-Flight Detector using an NE213 Scintillator with a Two-Bias Scheme

A neutron time-of-flight (TOF) method was adopted in the present experimental method. This method is generally used for neutron spectrum measurements with a pulsed neutron source. It had previously been applied to integral experiment for reactor physics in the measurement of fast neutron spectra leaking from fission materials, utilizing a linear accelerator-based neutron source.[6] For fusion reactor engineering, Wong et. al.[7] at LLNL applied this method in the measurement of the total leakage neutron current from a sphere assembly, with a pulsed DT neutron source.

The detectors used for the above measurement over the energy ranges of 2 - 15 MeV and 10 keV - 1 MeV were NE213 and ^{6}Li-glass scintillators. Kappler et al.[8] at KFK made use of this technique for in-core angular flux measurements using a re-entrant hole. They also used two detectors (NE213 and ^{6}Li-glass), and extended the measuring energy range of the NE213 detector down to 250 keV so as to overlap the ranges of both detectors. In practice, two-detector system is somewhat awkward, requiring preparation of two detector channels. Moreover, the efficiency of the Li-glass detector is unreliable around the resonance at 250 keV because of large error in the measured cross section used in the efficiency calculation.

The spectrum of neutrons obtained from fusion sources mainly contains 14 MeV neutrons, together with very few neutrons below 1 MeV compared with high energy neutrons. However, the neutron detection efficiency of a ^{6}Li-glass detector, whose thickness is chosen to obtain lower gamma-ray efficiency, is too small to measure the low energy neutrons below 1 MeV. The usage of a single NE213 detector with extended measuring energy range, could materially shorten the time needed to perform the experiment. Measurement in the low energy region with NE213 scintillator, however, has been unreliable due to the uncertainty in efficiency which is caused by unknown contributions from non-elastic carbon reactions, $^{12}C(n,\alpha)^{9}Be$ and $^{12}C(n,n'3\alpha)$, in the scintillator.[9] Another problem in low-energy measurement is neutron-gamma separation. Firstly, the pulse shape discrimination (PSD) circuit usually used for that purpose has a limited dynamic

range for pulse height; in high gain operation, the PSD property becomes worse by pulse saturation. Secondly, the intrinsic neutron-gamma separation is limited to about 300 keV for protons due to the linear energy transfer property of charged particles in the NE213 scintillator.[10] Since high energy neutrons produce strong gamma-ray flux around the detector, a low-bias measurement has a disadvantage for high-energy neutron detection.

These unreliabilities in low-energy measurement have been resolved at the same time by the combination of two different biases. This method, developed here and designated the "two-bias scheme", is described below.

3.3.1 Electronic circuit with two bias channels

The electronic circuit, arranged as shown in Fig.3.3.1, involves two separate pulse shape discriminators.[11] The 50.8 mm-diameter and 50.8-mm thick scintillator was mounted on an R329 photomultiplier tube with E934 base (Hamamatsu Photonics). The anode signal was branched into two channels. One of these was attenuated to 1/10 through a 50 Ω signal splitter The neutron and gamma separation was performed by these two signals using individual pulse shape discrimination (PSD) circuits. The low bias operation used coincidence signals combined by two PSD circuits to extend the dynamic range. A single-parameter measurement was adopted to reduce the complexity of data processing. Thus, two time-of-flight spectra were measured with different biases and PSD gates.

Figure 3.3.2 illustrates how the combination of two PSD signals was attained. The PSD output for large pulses were deformed by saturation in the amplifier. Pulses smaller than a certain level and larger than this were obtained as output from the direct channel and the 1/10 attenuated channel, respectively and were used as the PSD gate for low bias. Saturation of the direct signal limited the high voltage to -2300 V for the photomultiplier. Under those conditions, the low bias level could be set at 1/16 of the ^{241}Am gamma -ray peak of 59 keV. Since the carbon contribution to the efficiency at 1/16 Am bias increases above the neutron energy of 1 MeV, the Compton edge of ^{133}Ba gamma rays was chosen for the high bias. The result of this combination is shown in Fig. 3.3.3 for 14 MeV neutrons.

The high bias is set to dynode pulses by a single-channel analyzer. All coincidence timing is synchronized by strobe pulses from constant fraction discriminators to cover the wide time range of the time-to-pulse height converter (TAC). Two time spectra, for low and high bias, are collected at a different range for each bias, i.e., a shorter time range is adopted for high bias to obtain precise time resolution.

3.3.2 Neutron detection efficiency of NE213 scintillator

Neutron detection efficiency of NE213 scintillator is usually determined by the following methods:

(1) Direct method; determined by absolute mono-energetic neutron sources of different energy, i.e, (p,n) or (d,n) reaction neutron source using an accelerator,

(2) Comparison method: normalized by comparison with other known standards, e.g., the standard cross sections of hydrogen and carbon, the standard neutron field of the ^{252}Cf fission spectrum, and, sometimes, a reference field of leakage neutrons from a graphite pile with assistance of transport calculations.

(3) Calculation method: calculated using cross sections of hydrogen and carbon contained in the NE213 liquid scintillator, by an analytical or Monte Carlo method.

The direct method requires a mono-energetic neutron source covering a wide energy range. The use of standard cross sections also needs such a neutron source. The fission spectrum of ^{252}Cf is determined precisely in the range of about 500 keV to 10 MeV but still has much uncertainty in the energy range below 500 keV because of multiple scattering due to the capsule containing californium, for example. Since the cross sections of hydrogen and carbon, i.e., the components of NE213, are known accurately (except non-elastic reactions of $^{12}C(n,\alpha)^{9}Be$ and $^{12}C(n,n'3\alpha)$), the calculational method is the best means to obtain the efficiency in the absence of a mono-energetic neutron source. The effect of non-elastic reaction appears at low pulse height, hence, their uncertainties affect the calculated efficiency for high-energy neutrons chiefly at very low discrimination bias.

In the present work, the calculated efficiency has been used predicting it from the ambiguity of non-elastic reaction in carbon by combination of two biases. combination of two biases. The biases are chosen so as to share the measuring energy range: the high bias excludes the response produced by the non-elastic reactions of carbon, while the low bias channel is used only to register low-energy neutrons whose response has no non-elastic reaction.

The neutron response in the NE213 liquid scintillator was calculated by a Monte Carlo code using pointwise scattering cross sections. The nuclear data for hydrogen and carbon and light output efficiency for charged particles were taken from ENDF/B-IV[12] and Verbinski's data[13], respectively. The calculated response was broadened by a Gauss function corresponding to the detector energy resolution and integrated above the discrimination bias level. Figure 3.3.4 shows the efficiencies calculated for typical biases with and without carbon contribution. It is clearly seen in the figure that non-elastic reaction contributions of carbon are large for the case of low bias levels.

The bias value is usually defined in terms of the half-height of the Compton edge of standard gamma-rays. Those reference points in the pulse height distribution must be converted to the light output unit used in the efficiency calculation in order to apply them to the measurement. Therefore, the gamma-ray response for the NE213 scintillator was also calculated in electron energy units by the Monte Carlo code[14] and then the half-height edges of the gamma-rays were calibrated to Verbinski's light output unit. These results of the gamma-ray calibration are shown in Fig.3.3.5 and summarized in Table 3.3.1. This response is not in proportion to electron energy below the edge of ^{133}Ba gamma-ray. Thus a gamma source having low energy single line is needed for calibration of the low discrimination bias. At present, the 59 keV photopeak of ^{241}Am and the Compton edge of the 122 keV ^{57}Co gamma rays were used for lower bias calibration.

The discriminator dial to set a bias was determined with precision of the index by five times larger than the minimum interval. For this choice, reproducibility of the discrimination level is expected to be within 4 %, if one reads one fifth of the interval. This value corresponds to 1/16 of the ^{241}Am photopeak in our system.

This procedure is performed with a multi-channel analyzer (MCA) using a coincidence gate on the discriminator output as shown in Fig. 3.3.6.

Sharp discrimination at the desired bias was effected by a constant fraction discriminator. The discrimination resolution for lower biases, however, is relatively worse than for higher biases. One reason for this is a loss of neutrons from the coincidence gate; another is a deformation of PSD signals for pulses near the discrimination level. These discrimination property was examined by taking the ratio of pulse height spectra with and without PSD gate. Figure 3.3.7 shows this ratio and an illustration of discrimination for the low bias. The ratio spectrum seems to be composed of two parts, the gamma-ray rejection region having a gentle slope and the real bias a steep slope. The discrimination factors were determined by these ratios. Then the efficiency for low bias was found by combining the differential efficiency of NE213 with those factors as follows:

$$\varepsilon(E_n, h_o.) = \varepsilon(E_n, h_n) + \sum_{i=1}^{n} (1-f_i) \cdot R(E_n, h_i) \cdot \Delta h_i, \qquad (3.3.1)$$

where ε = efficiency of neutron energy E_n for bias h_o,

h = light output boundary,

f_i = discrimination factor (= counts with discrimination / counts without discrimination),

R = differential efficiency between h_i and h_{i+1},

Δh_i = light output interval.

3.3.3 Experimental confirmation of the detector system

The detector system and efficiency were confirmed experimentally by comparison of measured spectra with a reference spectrum. The reference spectrum was produced by neutrons leaking from a graphite pile with a DT neutron source placed at the center. The experimental setup is shown in Fig. 3.3.8. The graphite pile is a cube of 556.6 mm side length; the source void is a cube of 101.2 mm side length lined with 4 mm-thick aluminum, as shown in Fig. 3.3.9. The NE213 detector, located at the distance of 9.57 m from the source, can see the face of the pile through a 50 mm diameter collimator. The neutron scattering cross section of carbon is relatively reliable and does not have any

structure in the energy range of 1 keV to 1 MeV. That feature is very desirable for the reference neutron field.

The neutron spectrum at the detector position in this reference field was calculated by the Monte Carlo code MORSE-DD[15] with nuclear data of ENDF/B-V[12]. Figures 3.3.10 shows the raw measured spectrum uncorrected by the efficiency, and the spectrum calculated by that code. The ratio of both spectra provides the efficiency,

$$\varepsilon(E_n) = \frac{\phi(E_n)}{C(E_n)} \quad , \qquad (3.3.2)$$

where ε, ϕ and C are the efficiency, the calculated neutron flux and the raw data, respectively.

The energy uncertainty in this arrangement, dominated by flight path ambiguity due to thickness of the assembly, is about 6 %. This difference of energy scale causes a large deviation of the ratio around the peak structure, hence, the comparison should be limited to the energy region below 2 MeV.

The results of the ratios for various biases are shown in Fig. 3.3.11, together with the calculated efficiencies. The figure also includes the efficiency produced by the discrimination factor described above. The efficiency calculated without consideration of the discrimination factor deviates from the measured efficiency for low bias, while the efficiency composed by the discrimination factor agrees very well with the directly measured one. This shows that the composed efficiency is very successful for low bias. Figure 3.3.12 shows the deviation of the measured efficiency from the composed one for 1/16 Am-bias. The deviations are less than 10 % from about 60 keV to 2 MeV but the data are scattered beyond this range.

3.4 Collimator and Detector shield

A collimator is required for angular neutron flux measurement on a restricted area of the sample assembly. The number of neutrons emitted from this area is expected to be small. Hence, the neutron detector must be shielded to improve the signal-to-background ratio. This detector-collimator system defines the effective measured area over which the flux is averaged. To obtain the latter, the collimator response function was measured. A simple area calculation method was

proposed and verified by experiments.

3.4.1 Collimator design

The collimator and detector shield used in the present study are shown in Figs. 3.4.1 and 3.4.2. The aperture has a diameter of 50 mm through the inner sleeves of iron and paraffin containing B_2O_3(30 weight %). The main materials of the collimator are 0.4 m-thick iron and 0.45 m-thick paraffin containing Li_2CO_3(20 weight %); total thickness of the collimator is 1 m. The main detector shield is made of paraffin containing Li_2CO_3 powder (20 weight %) and of 0.1 m-thick lead near the detector. The additional detector shield of 0.5 m-thick paraffin containing Li_2CO_3(20 weight %) covers the main shield as shown in Fig. 3.4.2. This outer shield contains iron blocks of 50 mm thickness in the vicinity of the detector.

The effect of the additional shield is shown in Fig. 3.4.3. The structure due to the room-returned neutrons is seen in the time spectra in the figure. The contribution of those neutrons is significantly reduced by adding the outer shield.

The shield performance of the collimator is estimated by the removal cross sections[15] of iron and hydrogen. These cross sections and shielding performance are summarized in Table 3.4.1.

Throat scattering of the collimator, i.e., surface-skin scattering, can be estimated using the formula by Glasgow[16] as in the following: if scattering can be assumed to be isotropic in the arrangement of Fig. 3.4.4, the integrated scattering flux is roughly calculated as:

$$I_s \simeq \frac{1}{2}\phi \int_{\beta_1}^{\beta_2} \frac{\sin\beta \, d\beta}{r_0^2+(L-X)^2} , \qquad (3.4.1)$$

where ϕ = source neutron intensity per unit solid angle,

r_0 = radius of collimator opening,

$\sin\beta = r_0/\sqrt{r_0^2 + x^2}$,

x = distance between source and scattering point,

L = distance between source and detector.

Thus, the fraction of the scattered component is given by

$$R_s \approx \frac{\text{scattered neutrons}}{\text{direct neutrons}}$$

$$\approx \frac{1}{2} \cdot L^2 \int_{\beta_1}^{\beta_2} \frac{\sin\beta \, d\beta}{r_0^2+(L-x)^2} \quad . \qquad (3.4.2)$$

If distances from the collimator to the source and from the collimator to the detector are large, i.e., $r_0 \ll x$,

$$R_S \sim -\frac{1}{2} L^2 r_0^2 \int_{\ell_1}^{\ell_2} \frac{dx}{x^3(L-x^2)^2} \quad , \qquad (3.4.3)$$

where ℓ_1, ℓ_2 are the points of entrance and exit of the collimator along the axis. In our case, with r_0 = 25 mm, L = 7.63 m, ℓ_1 = 4.20 m and ℓ_2 = 5.70 m, we obtain $R_s \approx 3.3 \times 10^{-5}$. This value is small enough to neglect throat scattering.

3.4.2 Effective measured area

To obtain the neutron angular flux on absolute basis, the area on the assembly surface, from which neutrons are emitted into the detector, should be well defined. The effect of the detector-collimator on the measurement must be known. To determine the 'effective' measured area, the detector-collimator response function was measured.

The effective measured area is defined by the equation ,

$$A_s = \int_0^\infty 2\pi r \cdot f(r) dr \ [m^2], \qquad (3.4.4)$$

where A_s is the effective measured area and r is the radial distance from the detector-collimator axis on the surface of the assembly. The detector-collimator response function f(r) is given by

$$f(r) = C_w(r)/C_o(r), \qquad (3.4.5)$$

where $C_w(r)$and $C_o(r)$ are the detected counts of neutrons coming from a source located at the position r on the surface with and without collimator system, respectively.

The detector-collimator response function f(r) was measured by scanning DT and ^{252}Cf neutron sources relatively on the measured plane utilizing the dual rotating deck. The result measured for the DT

neutron source by the TOF method is shown in Fig. 3.4.5. The measured response shows that the scattering component (doted line) is less than 0.1 % for DT neutrons. The difference of the response shape is caused by the source volume: The DT primary source size is equal to the accelerated deuteron beam size of ∿10 mm with a components of neutrons below 10 MeV that are scattered by the assembly, and thus form a source of target assembly size, ∿ 30 mm. Figure 3.4.6. shows the measured spectra for each position of the source by the TOF method. The flux below 10 MeV for the radial position of 0.11 m is almost background. The high energy peak shows a small-angle scattered component.

The dependence of the response function on the distance between the source and the detector was also examined by an integrated counts measurement using a ^{252}Cf source. These neutron sources, however, have finite volumes so that the measured response functions are actually smeared over their volumes, while the collimator-detector response function is defined for a point source. Therefore, the response functions were estimated by a calculation and then, in order to confirm the calculated results, they were compared with the measured results taking into account the finite volume of source .

Since the throat scattering component can be neglected as described in the previous section, the response calculation was performed by considering only a simple optical projection as illustrated in Fig. 3.4.7. The overlapping area of the neutron projection defined by the entrance of the collimator and the detector surface from the position of r on the source plane is proportional to the response function. The response function for point source was smeared with a Gauss function ($G(r) = (1/\sqrt{2\pi}\sigma)\exp(-r^2/2\sigma^2)$). The source scanning includes the effect due to a possible offset between the detector collimator axis and the source-detector axis. This offset was measured to be about 5 mm for the present system. Comparisons of the smeared response functions are shown in Fig. 3.4.8 for the neutron sources. The source diameters for smearing are estimated to be ∿ 10 mm (σ = 0.6) for the ^{252}Cf source and the DT source, and ∿30 mm (σ = 1.8) for the component of source neutrons scattered by the target assembly ranging below 10 MeV, respectively.

The effective measured areas obtained from the response functions are compared between calculation and the experiment in Fig. 3.4.9. In

the cases with offset = 5 mm and σ = 10 mm, for the most realistic conditions, good agreement is found within an experimental error of 2 %. The scattered component of the TOF result below 10 MeV is also seen around σ=1.8. These results suggest that the above simple calculation method is valid for the present detector-collimator system.

3.5 Data Reduction

The angular flux measurement is performed in foreground-background mode. The background is measured by blocking the collimator hole with a plug of type 304 stainless steel of 0.6 m length and polyethylene of 0.4 m length. Background data are subtracted from the foreground data. Measured time spectra are transformed to energy spectra by the relativistic relation,

$$E_n = 939.553 \cdot \left[\left(1.0 - 11.126496 \cdot \left(\frac{L_{eff}}{t_0 - t}\right)^{-\frac{1}{2}}\right)^{-1.0} \right] \quad [\mathrm{MeV}] \quad , \qquad (3.5.1)$$

where E_n is the neutron energy in MeV, L_{eff} the effective flight path in m (discussed further), t the neutron arrival time and t_0 the time-zero in ns of neutron emission. The time zero is determined by the peak in time spectra associated with the gamma-rays originating from the assembly.

Two parameters in the energy transformation, i.e., the time zero and the flight path, are determined. We can observe two gamma-ray peaks in the time spectra from the assembly. The first peak is due to Compton-scattering of gamma rays emitted from the target assembly, since no time variation is observed with detector angle. The second peak results from gamma rays produced by inelastic scattering of incident neutrons and varies in the time spectrum. The time difference between peaks is related to the effective scattering point as shown in Fig. 3.5.1. If we assume that there is no large difference in the effective scattering points compared with the flight path, the effective emission depth $\Delta\ell_n$ can be obtained from the relations

$$\ell' = \Delta T_{\gamma\gamma}, \left(\frac{72.3}{\sqrt{E_0}} - \frac{1}{0.3} \right) , \qquad (3.5.2)$$

and

$$\Delta \ell_n = \ell \cos\theta - \sqrt{\ell'^2 - \ell^2 \sin^2\theta} \quad ,$$

where E_0 is the incident neutron energy in MeV, $\Delta T_{\gamma\gamma}$, is the time difference between two gamma-ray peaks in ns, ℓ the distance of the rear face of the assembly from the target and θ is the leakage angle. Thus the effective flight path L_{eff} is

$$L_{eff} = L + \Delta \ell_n .$$

This correction estimated for the graphite assembly was less than about 5 %.

The measured data are reduced to the angular flux by the following equation as illustrated by Fig. 3.5.2.

$$\phi(\Omega, E_n) = \frac{C(E_n)}{\varepsilon(E_n) \cdot \Delta\Omega \cdot A_s \cdot S_n \cdot T(E_n)} \qquad (3.5.3)$$

[n/sr/m^2/unit lethargy/source neutron],

where $\phi(\Omega, E_n)$: neutrons with energy E_n per unit lethargy and emitting angle Ω per unit area and per total source neutrons at the rear surface center of the assembly,

$C(E_n)$: counts per unit lethargy for neutrons of energy E_n,

$\varepsilon(E_n)$: neutron detector efficiency at energy E_n,

$\Delta\Omega$: solid angle subtended by the detector to the point on the surface center of the assembly, i.e., $\Delta\Omega = A_d/L^2$, where

A_d : counting area of the detector,

L : distance from the rear surface to the detector,

A_s : effective measured area defined by the detector collimator system on the plane perpendicular to the axis at the assembly surface,

S_n : total source neutrons obtained by the associated

alpha particle monitor,

$T(E_n)$: attenuation due to air through neutron flight (= $\exp(-\Sigma_{air}(E_n)\cdot L)$, Σ_{air}:macroscopic total cross section of air).

A plot of the macroscopic cross section of air against neutron energy is shown in Fig. 3.5.3. The air attenuation correction has some structure due to cross section.

The neutron source spectrum from the target, ψ, is presented in the same manner.

$$\psi(\Omega,E_n) = \frac{C(E_n)}{\varepsilon(E_n)\cdot\Delta\Omega\cdot S_n\cdot T(E_n)} \qquad (3.5.4)$$

[n/sr/unit lethargy/source neutron].

Since there two spectra are normalized to total source neutron yield, systematic error of source neutron yield can be excluded by adopting this source spectrum for the analysis to be compared.

3.6 Uncertainty Analysis

The uncertainties included in the experimental results are associated with the energy scale and flux, they are composed of random errors, mainly related to counting statistics, and systematic errors, related to calibration or normalization.

3.6.1 Energy scale uncertainty

The energy scale uncertainty in the transformation of time spectra to energy spectra is attributed to uncertainties in the flight path and flight time. The random error, i.e., energy resolution and the systematic error are separately considered.

Energy resolution depends on the time resolution of the measuring system, which is a function of the electronics and deuteron beam pulse width, estimated to be $\sim$2 ns; this yields 2 % resolution for 15 MeV neutrons. Other causes are the flight path spread and emission time spread of neutrons scattered in the assembly. This is limited to within $2(\Delta L/L)$, i.e., $\sim$5 % for the 0.4 m-thick assembly.

The systematic errors are caused by the uncertainty of the time zero and effective flight path. The time zero t_0 and the effective flight path L_{eff} are determined by the gamma-ray peaks in the time spectrum as described in sect. 3.5. However, the effective flight path as defined is valid only for single-scattered neutrons, since the neutron emission point does not correspond to the gamma emission point if the neutron is scattered after emitting gamma rays by inelastic reaction.

The overall energy scale uncertainty of the observed neutrons is obtained by the equation:

$$\frac{\Delta E}{E} = 2\frac{\Delta t}{t} + \frac{\Delta \ell}{L} = 2\frac{t_1 - t_0}{t_2 - t_1} + 2\frac{\Delta \ell'_n}{L_{eff}}$$

$$= 2\frac{\Delta \ell'_n}{L_{eff}}\left(\frac{E}{\sqrt{E_0}} + 1\right) , \qquad (3.5.5)$$

where t_0, t_1 and t_2 are the time zero obtained by the gamma-ray peak, the true time zero and the time of neutron detection, respectively, $\Delta \ell'_n$ the difference of the positions at which the gamma rays and neutrons are emitted, E_0 and E the energies of incident and scattered neutrons (see Fig. 3.6.1).

This equation shows that the energy scale uncertainty depends on the neutron energy through t; the position difference $\Delta \ell'_n$ also changes with neutron energy. The difference $\Delta \ell'_n$ is very small for the high energy region, and $\Delta E/E$ nearly equals $2\,\Delta \ell'_n/L_{eff}$ for the lower energy region; $\Delta \ell'_n$ is smaller than $\Delta \ell_n$. Therefore, the uncertainty cannot exceed $2\,\Delta \ell_n/L_{eff}$, which is less than 8 % in the experiment.

3.6.2 Flux uncertainty

The flux uncertainty is composed of errors in the parameters appearing in the definition in sect. 3.5.

Source neutron intensity

The systematic error in source neutron intensity is estimated to be ±2 %.(See sect. 3.2) However, the systematic error is canceled when the measured source spectrum is used in the calculational analysis. Thus, the random error alone is significant and that is less than 1 %.

Detector efficiency

The detector efficiency error is caused by the errors involved in the efficiency calculation, neutron loss near the bias level, and mismatch due to instability of the discrimination circuit. The calculational errors come from the cross section and scintillation efficiency. The cross section error of hydrogen is ∿1 %. The scintillation efficiency error has the same effect as the discriminator instability, and thus it depends on neutron energy. Hence, the error due to the scintillation efficiency is negligible except in the energy range near bias, since the error of Verbinski's efficiency is reported to be less than 2 %.[13] Judging from the comparison of the measured reference field (graphite pile) with the calculation as shown in Fig. 3.3.17, the neutron loss near bias level is less than 10 % below 100 keV and is negligible above 100 keV. The discriminator instability or bias calibration error affects the range below 100 keV as shown in Fig. 3.6.2. Our bias setting procedure yields 4 % accuracy, so that the uncertainty below 100 keV is less than 10 %.

The overall uncertainty discussed above is summarized as follows:

1) For the energy range above 200 keV, the systematic error is less than 2 %,
2) For the range of 80 to 200 keV, the error is 5∿10 %,
3) For the range below 80 keV, the error is 10∿20 %.

Solid angle

The solid angle is determined by the distance from the assembly surface to the detector and by the detecting area. The distance of the assembly to the detector is large enough to neglect its error. The detecting area of the scintillator is determined within accuracy less than 1 %. Therefore, the total error is less than 1%.

Effective measured area

The uncertainty of this value depends on the accuracy of the detector-collimator response function. The value calculated by the optical simulation was used as the effective measured area in this experiment. The reliability of this calculational model was examined experimentally and the calculated value agreed with the experimental one within ±2 % . Thus this discrepancy is adopted as the uncertainty of the effective measured area.

Air attenuation correction

This factor is obtained from a macroscopic cross section of air and is estimated to be about 7 % of the angular flux. Even if it is assumed that the uncertainty of the cross section is 10 %, the error of this factor contributes less than 1 % to the error of the angular flux. Thus, it is considered to be negligible.

Neutron counts

The neutron count error originates in count statistics and in count loss due to electronic circuit dead time. The count rate was low enough to neglect the count loss. The statistical error was ± 1-20 % for each energy interval in lethargy unit.

Background subtraction

The time-dependent and time-independent background were measured in the background run by blocking the collimator-hole. All the background, excluding the contribution related to the collimator aperture, was subtracted from the foreground data. That background contribution, such as neutrons scattered by the inner wall of the collimator aperture and the neutron room return passing through the collimator aperture and the room return, is judged to be negligible from a rough calculational estimate as described in sect. 3.4.

The overall uncertainties for the present experimental system are summarized in Table 3.6.1.

3.7 Conclusion

In conclusion, an adequate neutron angular flux measuring system was developed successfully. The main difficulties in the experiment, to obtain the lower energy spectrum and to define the measured source area, were resolved by adopting the two-bias scheme and deriving a detector-collimator response function, respectively. By measuring the time difference between the secondary and scattered gamma-rays, we obtained the effective flight path length for the bulk sample. The errors in the measured spectrum were comparable with the uncertainties

in cross section data for fusion materials. Thus the present system can provide a method to obtain an angular flux on the restricted area on the rear surface of the slab bombarded with fusion neutrons.

References

1) Oyama Y., Maekawa H.: Nucl.Instr. Meth A245 , 173 (1986); Oyama Y., Maekawa H.: "Measurement of Angle-Dependent Neutron Spectra from Lithium-Oxide Slab Assemblies by Time-of-Flight Method," JAERI-M83- 195, Japan Atomic Energy Research Institute (1983); Oyama Y., Yamaguchi S., Maekawa H.: "Modification of the Time-of Flight System for Extending to Lower Energy Range," JAERI-M 86-125, p.124 (1986)
2) Oyama Y., Yamaguchi S., Maekawa H.: "Analysis of time-of-Flight Experiment on Lithium-Oxide Assemblies by a two Dimensional Transport Code DOT3.5," JAERI-M 85-031 (1985)
3) Nakamura T., Maekawa H., Ikeda Y., Oyama Y.: "A DT Neutron Source for Fusion Neutronics Experiments at the JAERI," Proc.Int.Ion Engineering Congress-ISIAT'83 & IAPT '83, Kyoto, Japan, vol.1, 567 (1983)
4) Maekawa H., et al.: "Neutron Yield Monitors for the Fusion Neutronics Source (FNS)-For 80° Beam Line-," JAERI-M 83-219 (1983)
5) Yamaguchi S., Oyama Y., Maekawa H.: "Calculation of Anisotropy Correction Factor for Determination of D-T Neutron Yield by Associated α-Particle Method," JAERI-M 84-109 (1984)
6) Profio A.E., Anturez H.M., Huffman D.L.: Nucl. Sci. Eng., 35 , 91 (1969)
7) Wong C., et.al.: "Livermore Pulsed Sphere Program: Program Summary Through July 1971," UCRL-51144, Lawrence Livermore National Laboratory (1971)
8) Kappler.F.K., et al.: Nucl. Instr. Meth. 111 , 83 (1973)
9) Drosg M., Drake D.M., Lisomski P.: Nucl. Instr. Meth. 176 , 477 (1980)
10) Perkins L.J., Scott M.C.: Nucl. Instr. Meth. 166 , 451 (1979)
11) Sperr P., et al.: Nucl. Instr. Meth. 166 , 55 (1974)
12) ENDF/B Summary Documentation, BNL-NCS-17541 (ENDF-201), 2nd Edition, compiled by D. Garber (1975)

13) Verbinski V.V., et al.: Nucl. Instr. Meth. 65 , 8 (1968)

14) Oyama Y., et al.: Nucl. Instr. Meth. A256 , 133 (1987)

15) Nakagawa M., Mori T.: "MORSE-DD, A Monte Carlo Code Using Multi-Group Double Differential Form Cross Section," JAERI-M 84-126 (1984)

16) Glasgow D.W., et al.: Nucl.Instr Meth. 114 , 521 (1974); Alexander L.Jr.: "Neutron Collimation and Shielding," Fast Neutron Physics, Part I, Interscience Publisher, New York (1963)

Table 3.3.1 Light unit values and Compton half-height edge for typical standard gamma-ray sources: Calculation with the Monte Carlo code, where the detector is set at a distance of 10 mm from gamma-ray source (Eg : gamma-ray energy, Ec : maximum energy of Compton electron)

Gamma-ray source	Eg(MeV)	Ec(MeV)	Half-height of Compton edge(MeV) (calculated)	Light output in ^{22}Na light unit (measured)
^{57}Co	0.1221	0.0395	0.046±0.001	0.026±0.001
^{241}Am	0.0595	———	0.060*1	0.034±0.001*3
^{133}Ba	0.356	0.183	0.220±0.002*2	0.143±0.003
^{137}Cs	0.661	0.477	0.494±0.001	0.360±0.007
^{54}Mn	0.835	0.638	0.660±0.007	0.508±0.010
^{22}Na	0.511	0.341	0.356±0.004	0.250±0.005
	1.274	1.063	1.075±0.003	0.855±0.017
^{88}Y	0.898	0.599	0.720±0.006	0.564±0.011
	1.836	1.512	1.625±0.002	1.314±0.026

*1 full energy peak

*2 fraction of deviation by a 30% change of detector resolution

*3 fraction of deviation by a 2% change of system gain

Table 3.4.1 Shielding Performance of iron and hydrogen

Fe

En (MeV)	Σ (cm^{-1})	1/10 length (cm)
5 ∿ 14	∿ 0.11	∿ 21
2 ∿ 5	0.07 ∿ 0.1	23 ∿ 33
1	0.02	115

H in Paraffin

En (MeV)	Σ (cm^{-1})	1/10 length (cm)
10 ∿ 14	0.06 ∿ 0.08	29 ∿ 38
5	0.14	16
2	0.24	10
1	0.35	7

Table 3.6.1 Systematic errors of measured flux

Error source	Systematic error
1) Source neutron intensity	±2 %
2) Efficiency	
E_n > 200 keV	< 2 %
80 < E_n < 200 keV	5-10 %
50 < E_n < 80 keV	10-20 %
3) Solid angle	<< 1 %
4) Effective measured area	< ±2 %
5) Air attenuation correction	<< 1 %

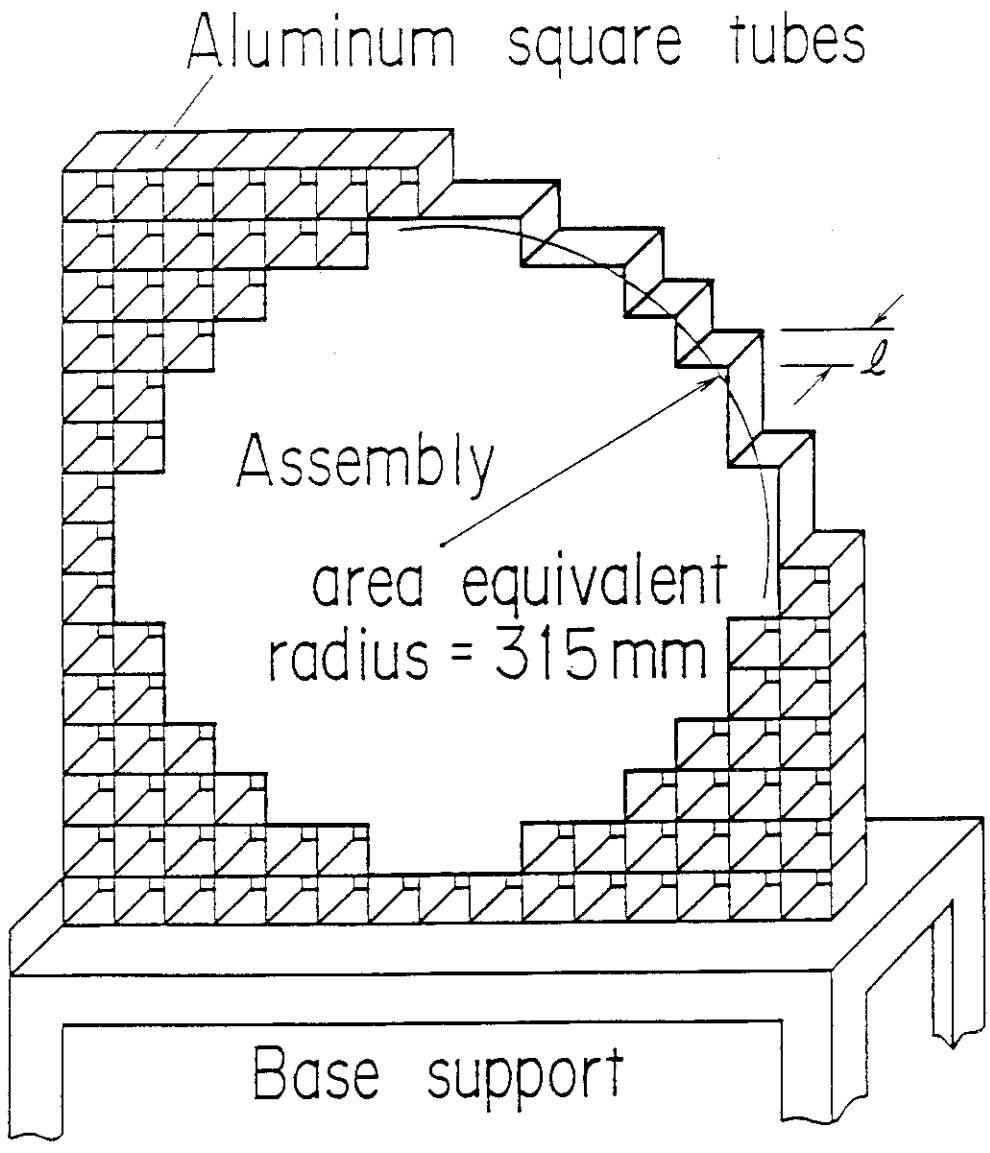

Fig. 3.2.1 Experimental slab assembly in pseudo-cylinder.

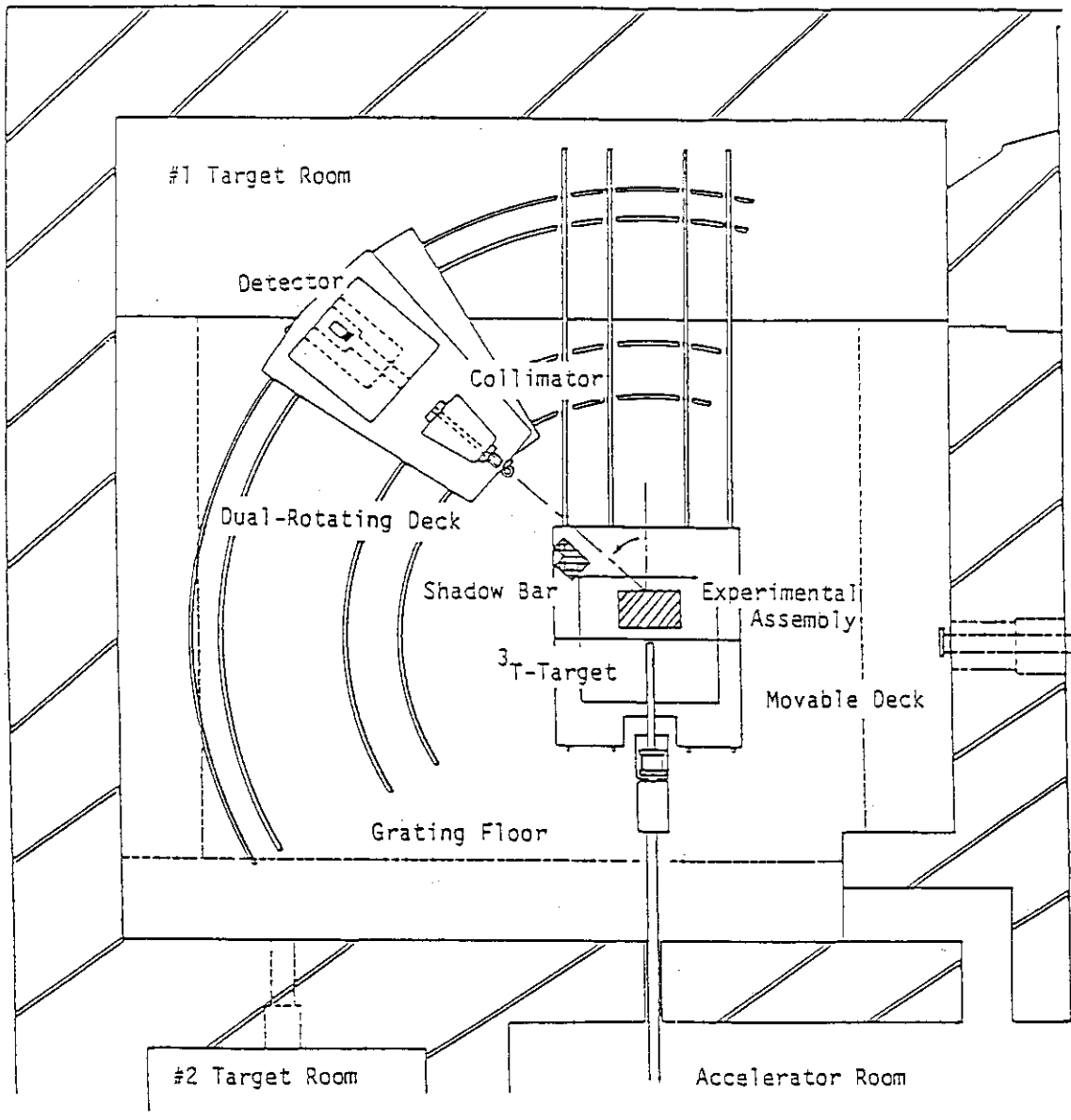

Fig. 3.2.2 Layout of experimental system in the target room.

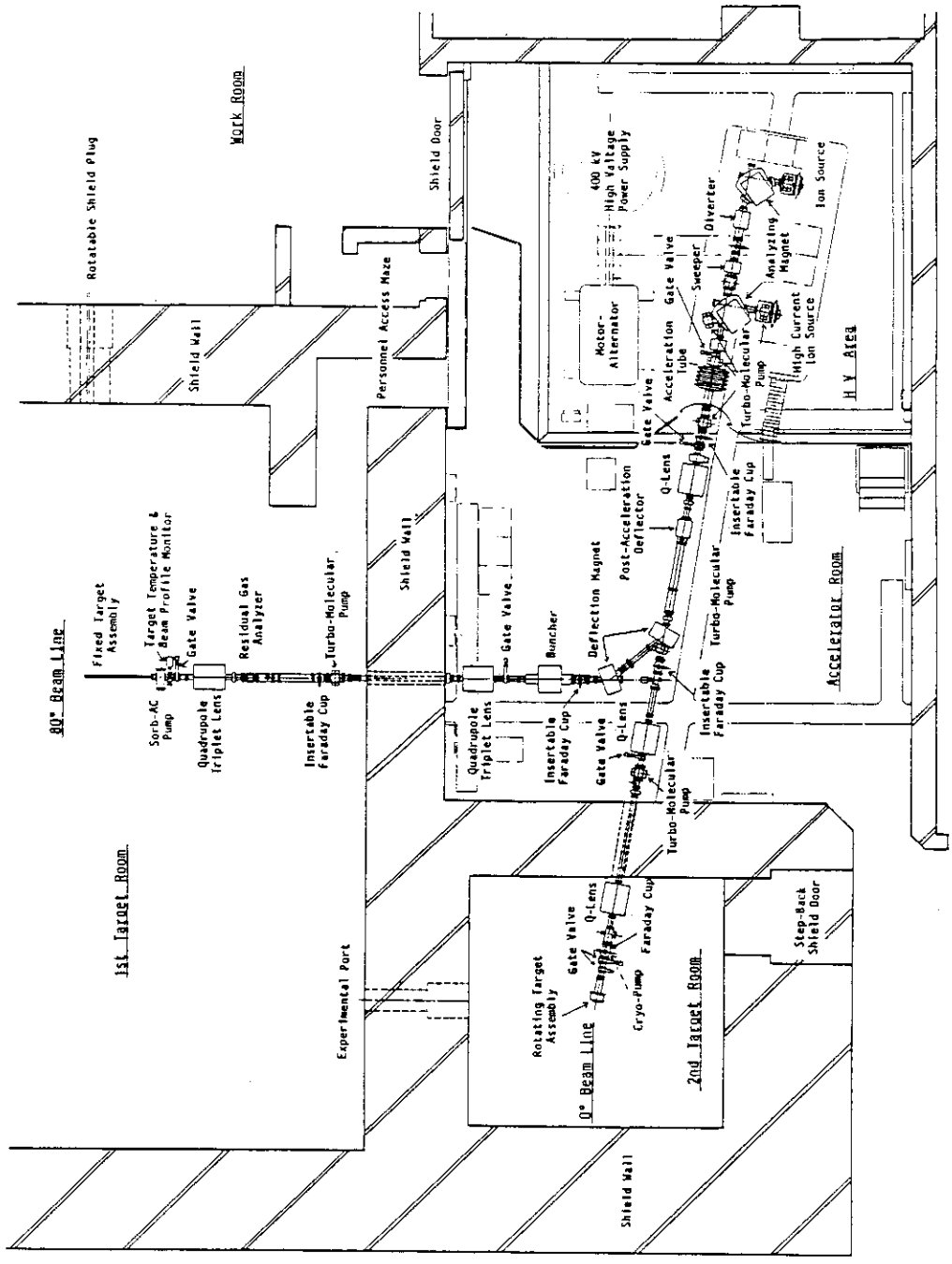

Fig. 3.2.3 FNS accelerator system.

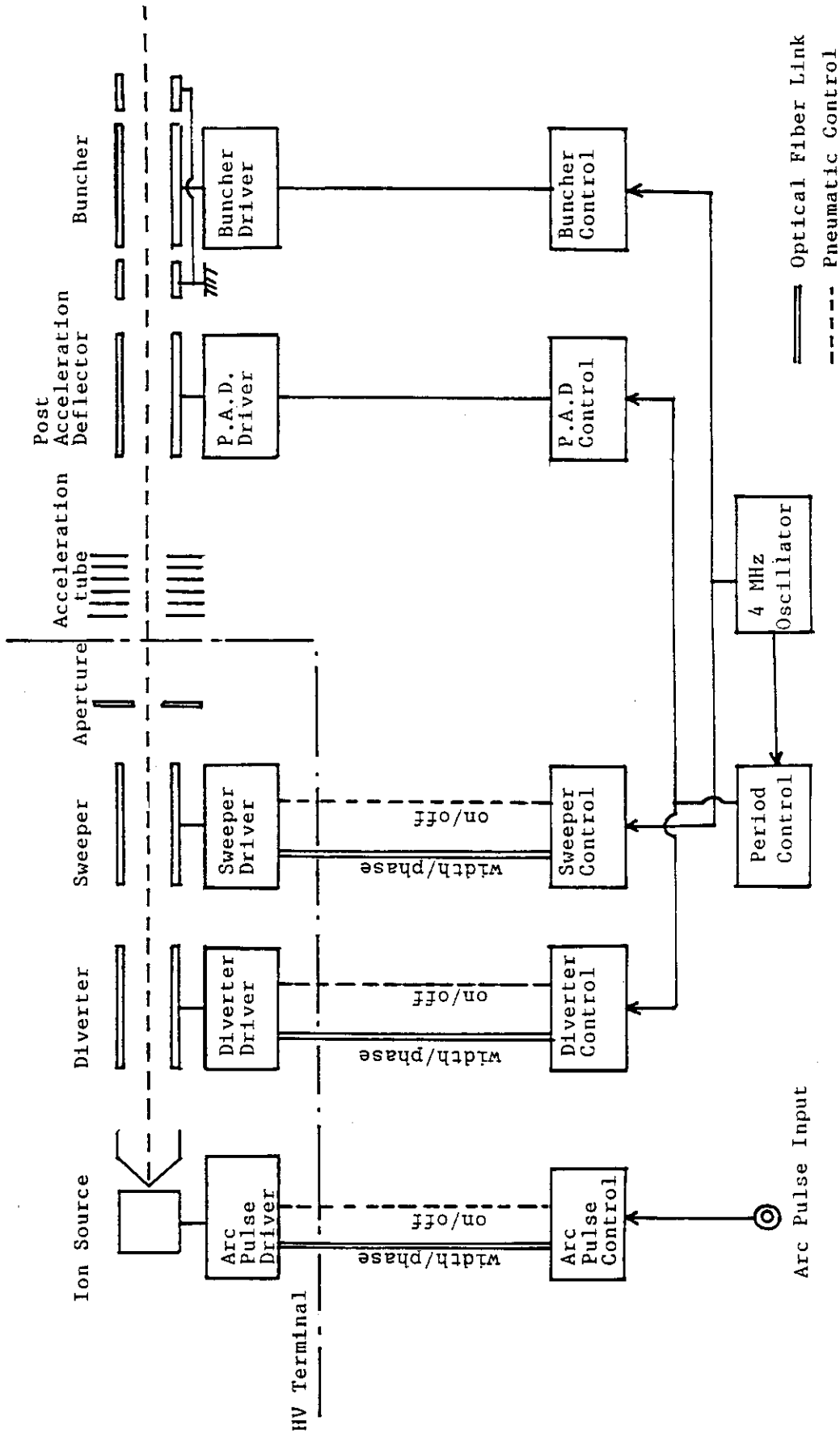

Fig. 3.2.4 Schematic diagram of pulsing system.

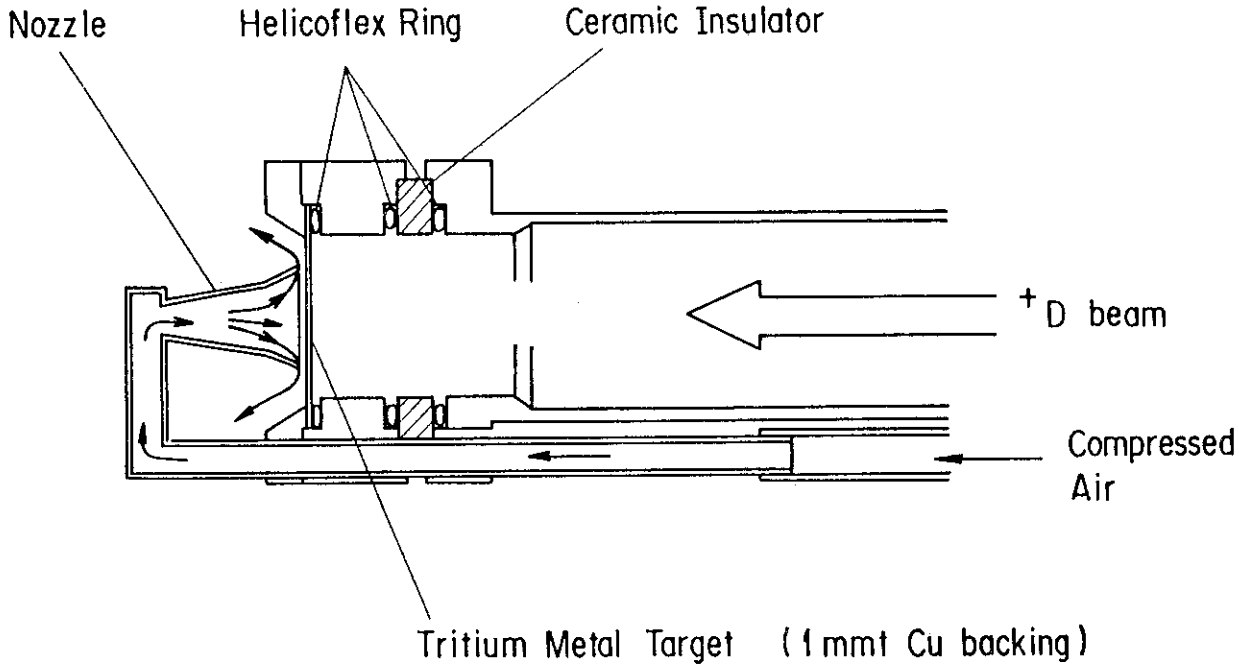

Fig. 3.2.5 Target assembly cooled by compressed air flow.

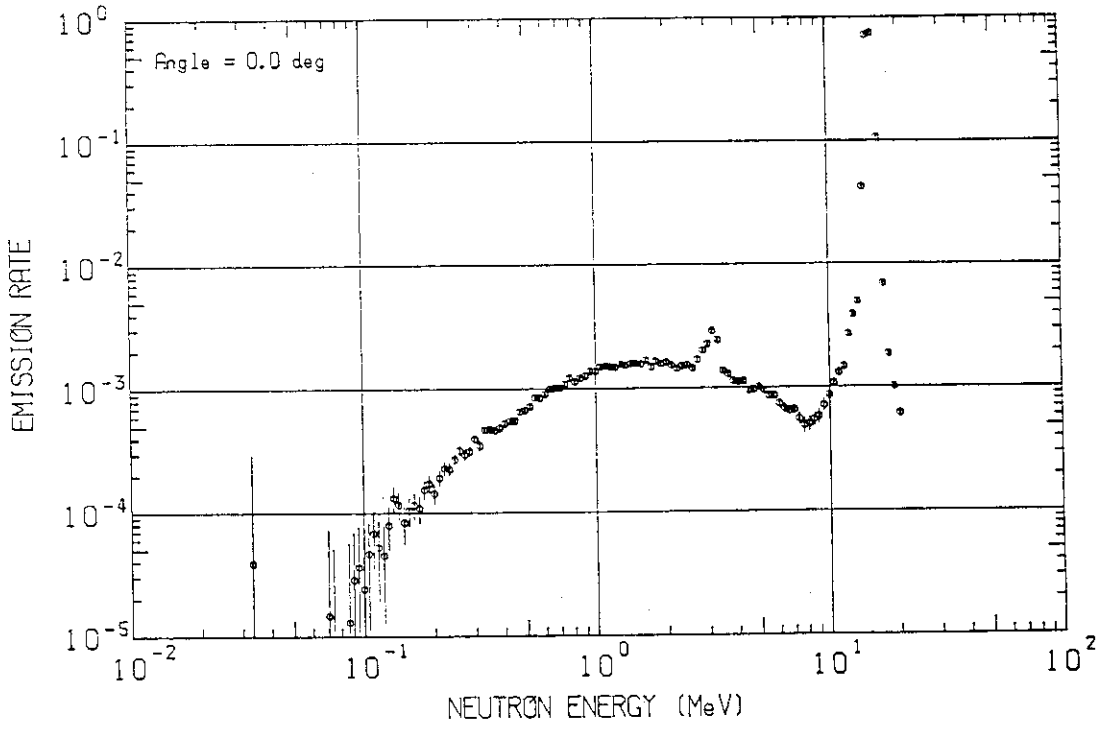

Fig. 3.2.6 Energy spectrum of neutrons emitted from the target.

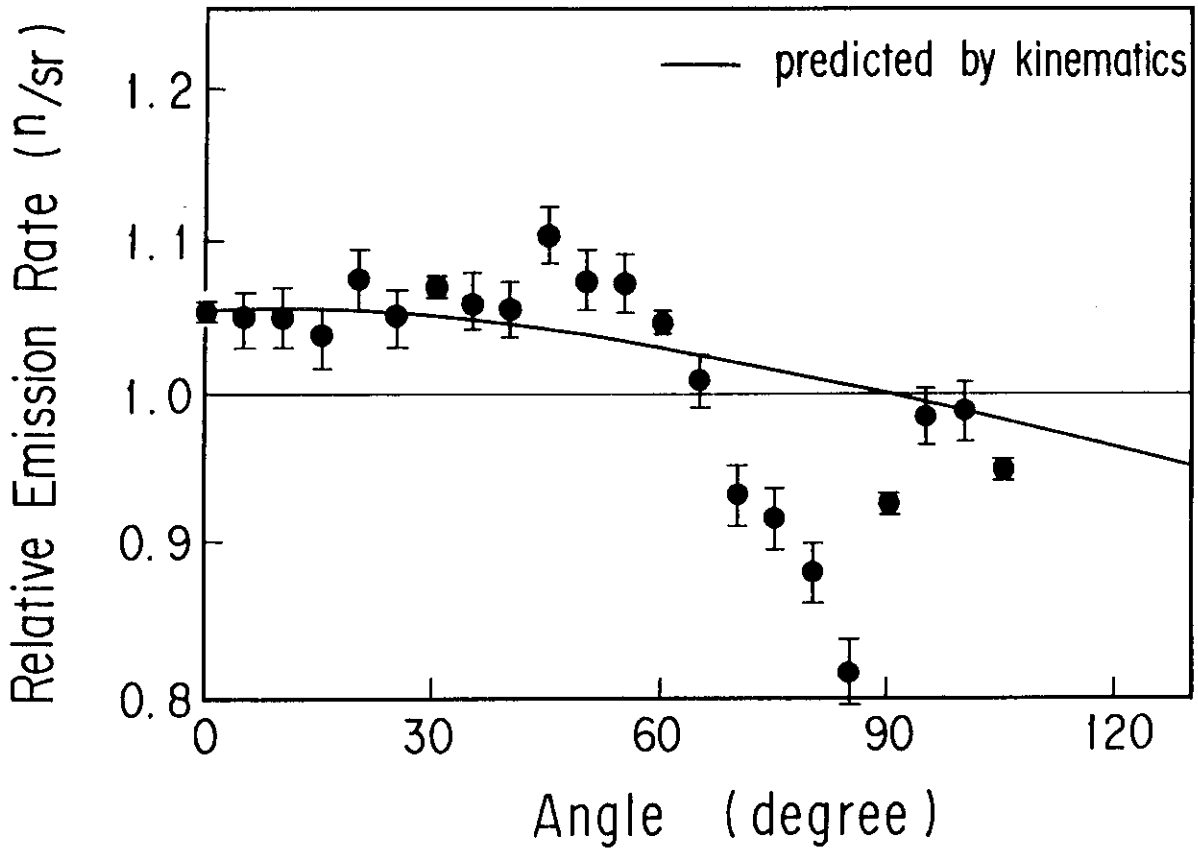

Fig. 3.2.7 Angular distribution of neutron emitted form the D-T target.The neutron emission is normalized to the value at 90 degree. the measured value show neutron emission above 10 MeV and a solid line is the prediction by a kinematic calculation.

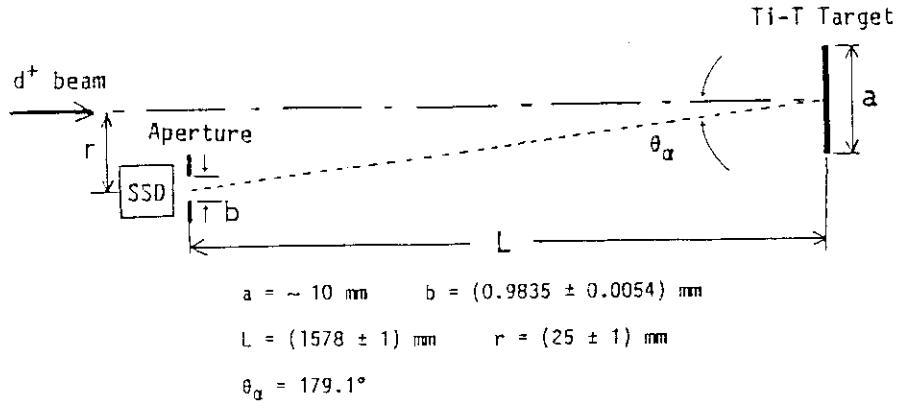

Fig. 3.2.8 Geometrical configuration of α-monitor in the beam line.

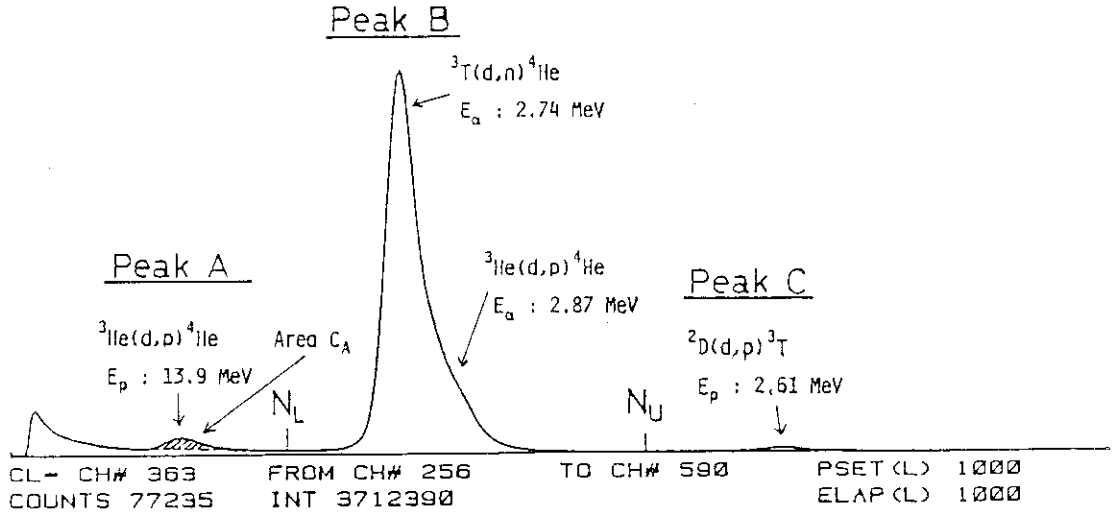

Fig. 3.2.9 Typical pulse height spectrum of the SSD in linear scale.

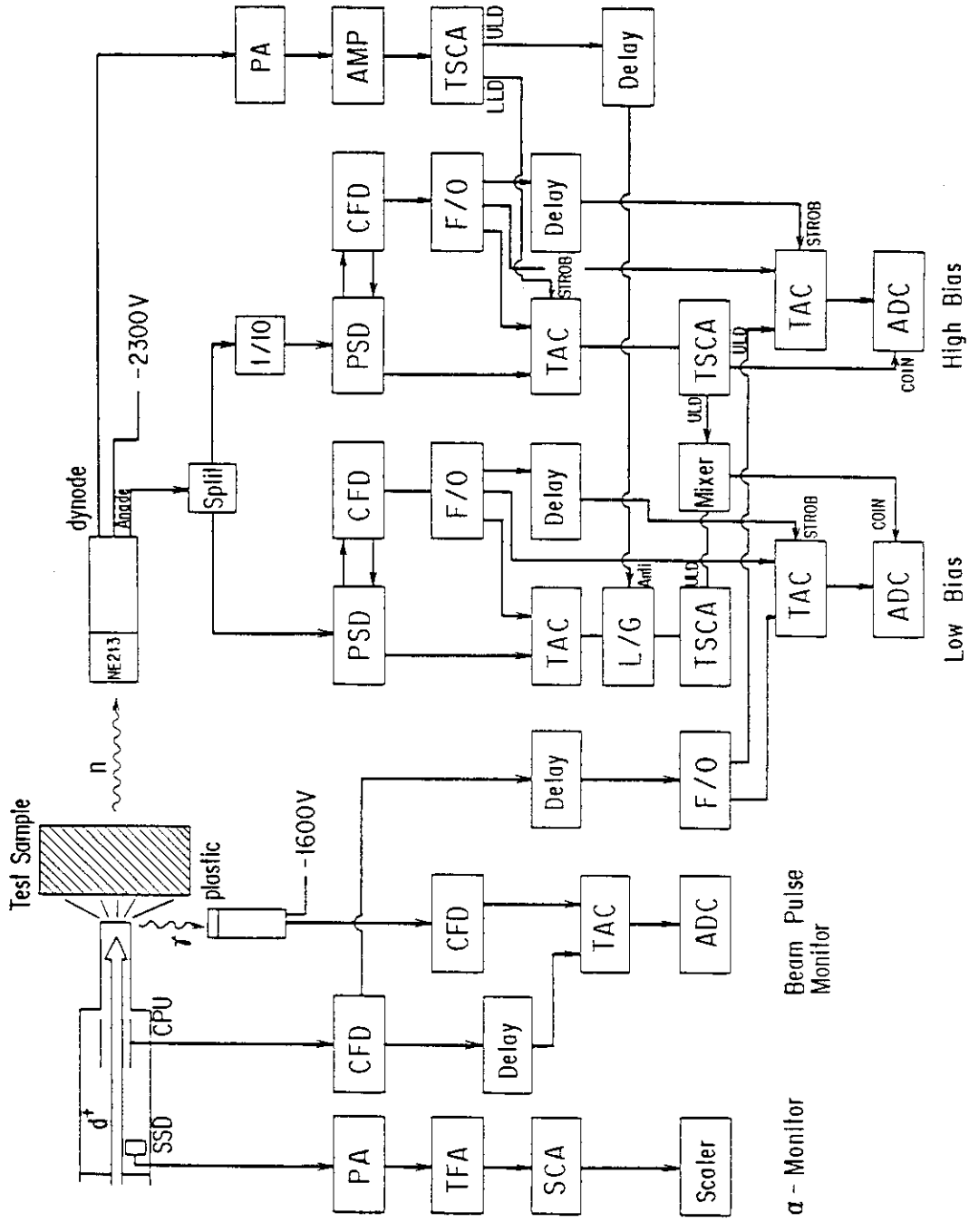

Fig. 3.3.1 Schematic diagram of electronic circuit for two-bias time-of-flight system.

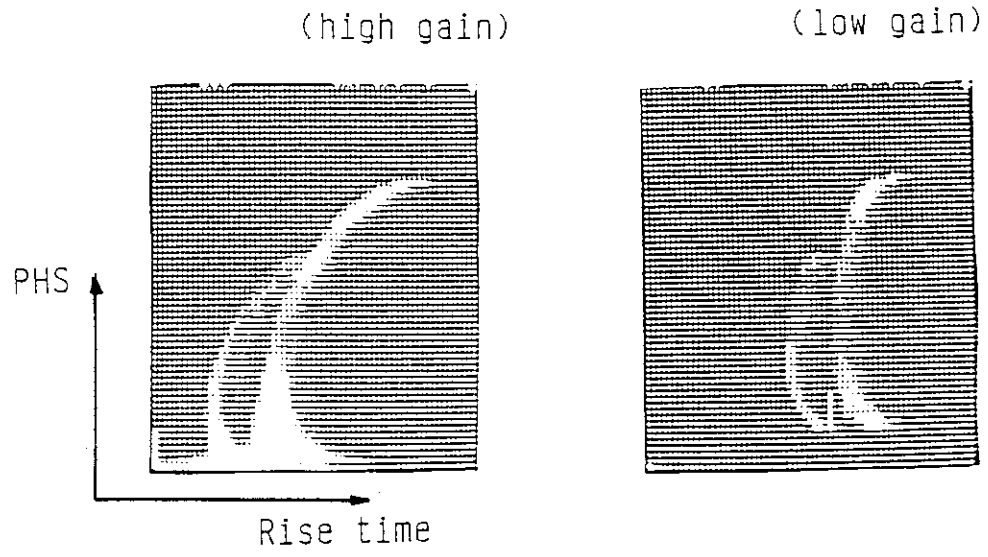

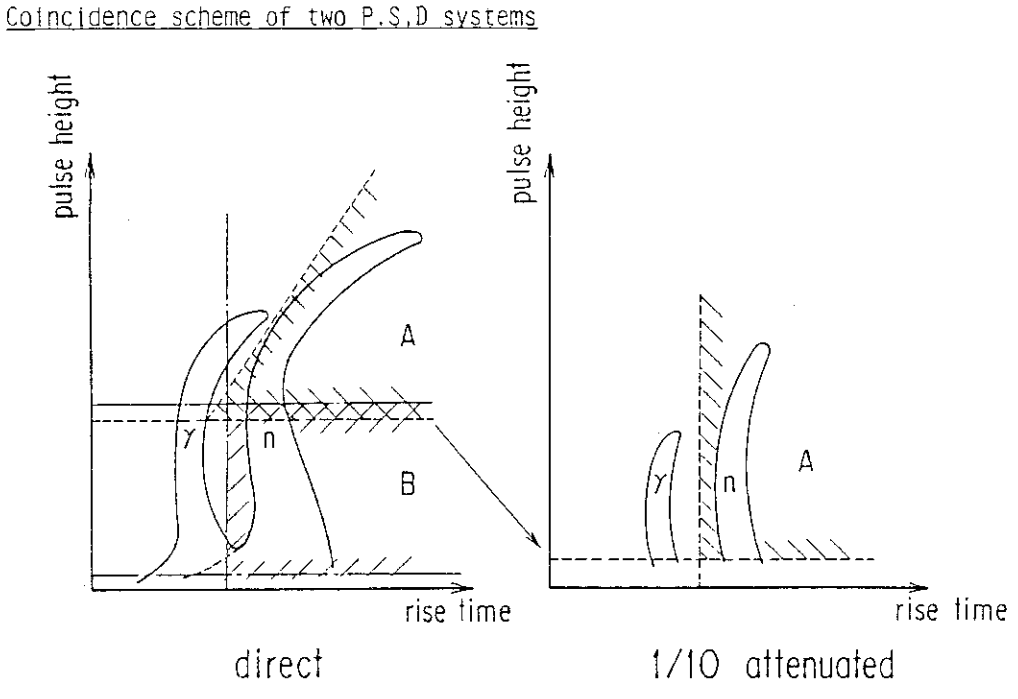

Fig. 3.3.2 (a) Saturation in pulse shape discrimination system. Two parameter representation is deformed for high gain.

(b) Illustration of combination gate with two pulse shape discrimination circuits. The coincidence with A+B gate is used for low-bias measurement.

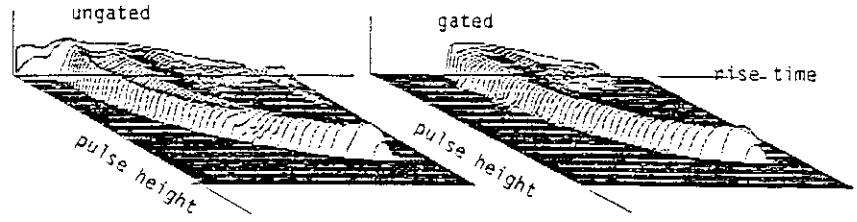

Fig. 3.3.3 Isometric view of the result for 14 MeV neutron field by combination gate.

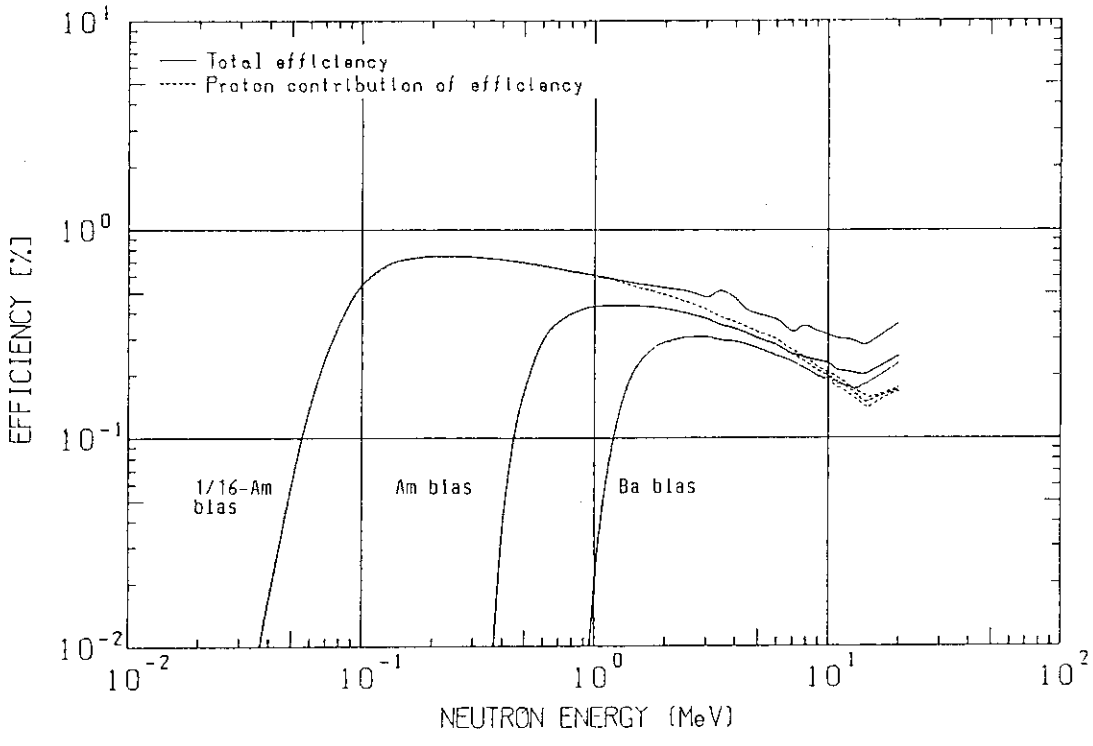

Fig. 3.3.4 The calculated efficiencies with and without the alpha-particle response. Dot line shows the contribution of protons alone.

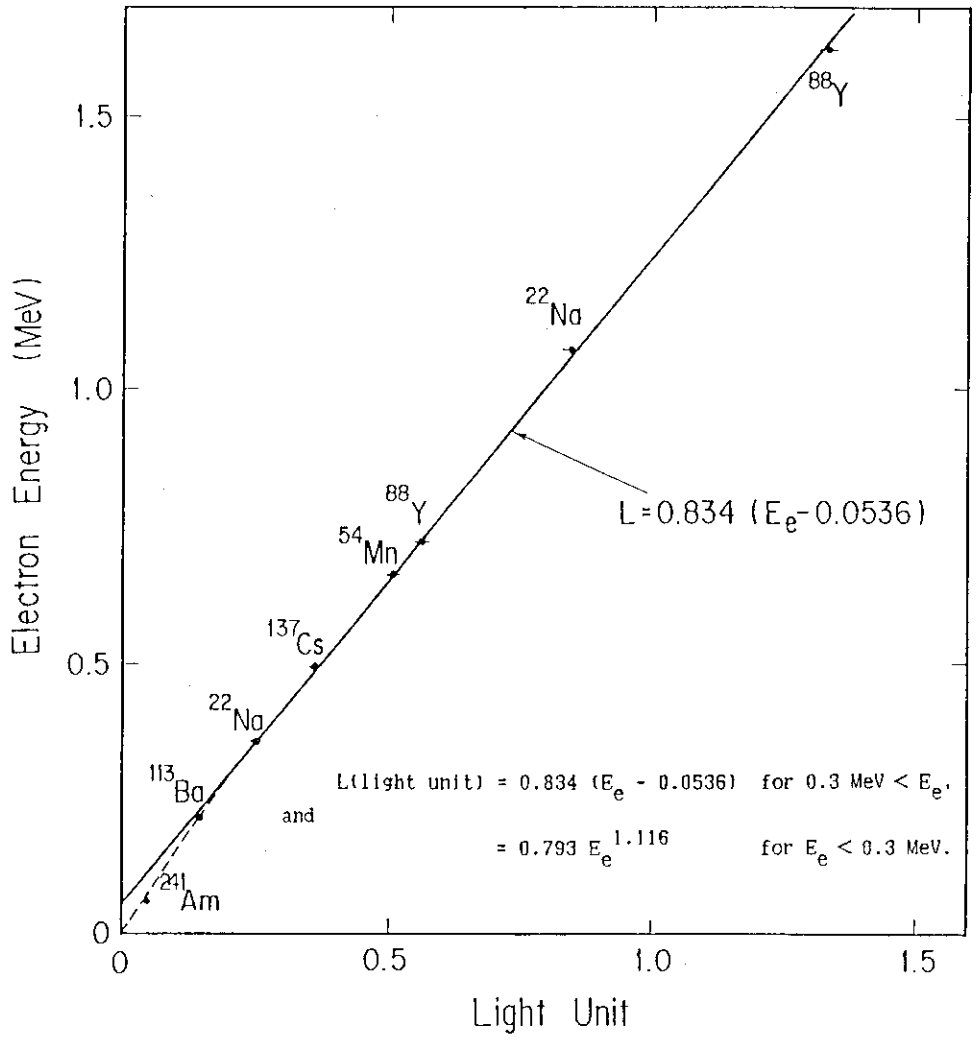

Fig. 3.3.5 The relation of the electron energy vs. the light output for various standard gamma-rays

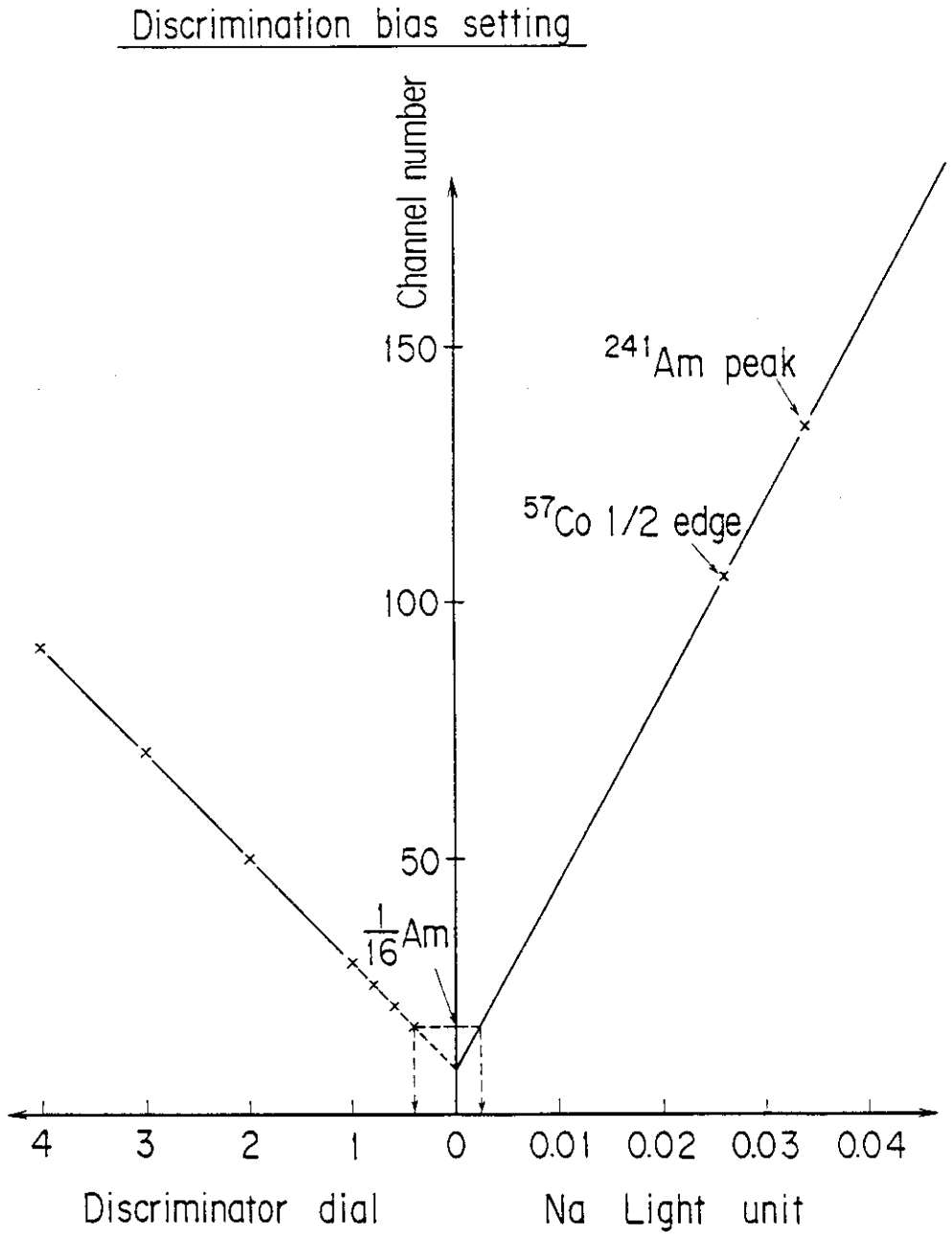

Fig. 3.3.6 The calibration procedure of the bias discriminator for the light output used in the efficiency calculation.

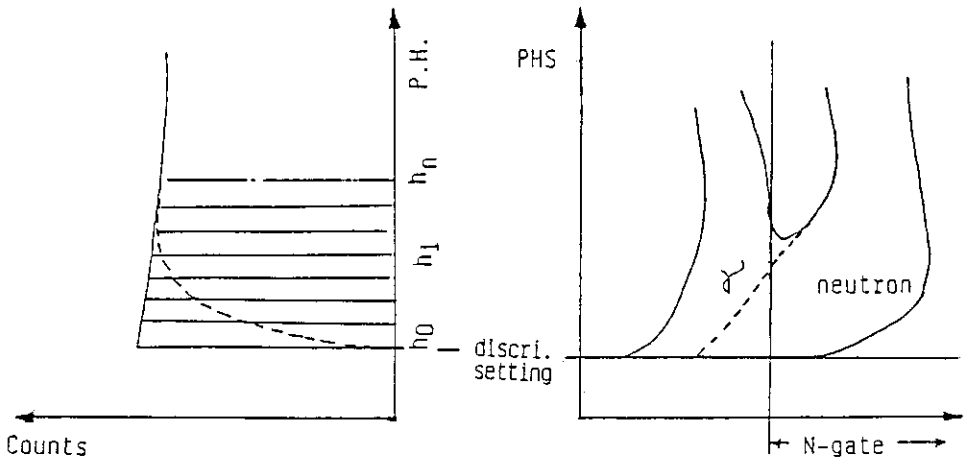

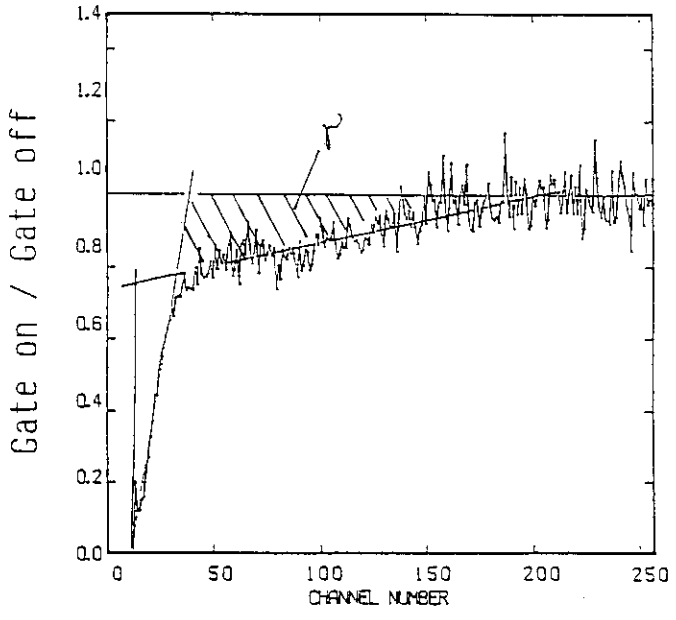

Fig. 3.3.7 (a) Illustration of the discrimination factor. The discriminator does not clearly cut the pulse height distribution as a knife edge.

(b) The energy pulse discrimination property with pulse shape discrimination (PSD) for ^{252}Cf neutron field. The ratio of the spectrum with PSD gate to that without PSD gate shows two parts: One is due to the gamma-ray rejection by PSD and another is the edge by the energy discriminator.

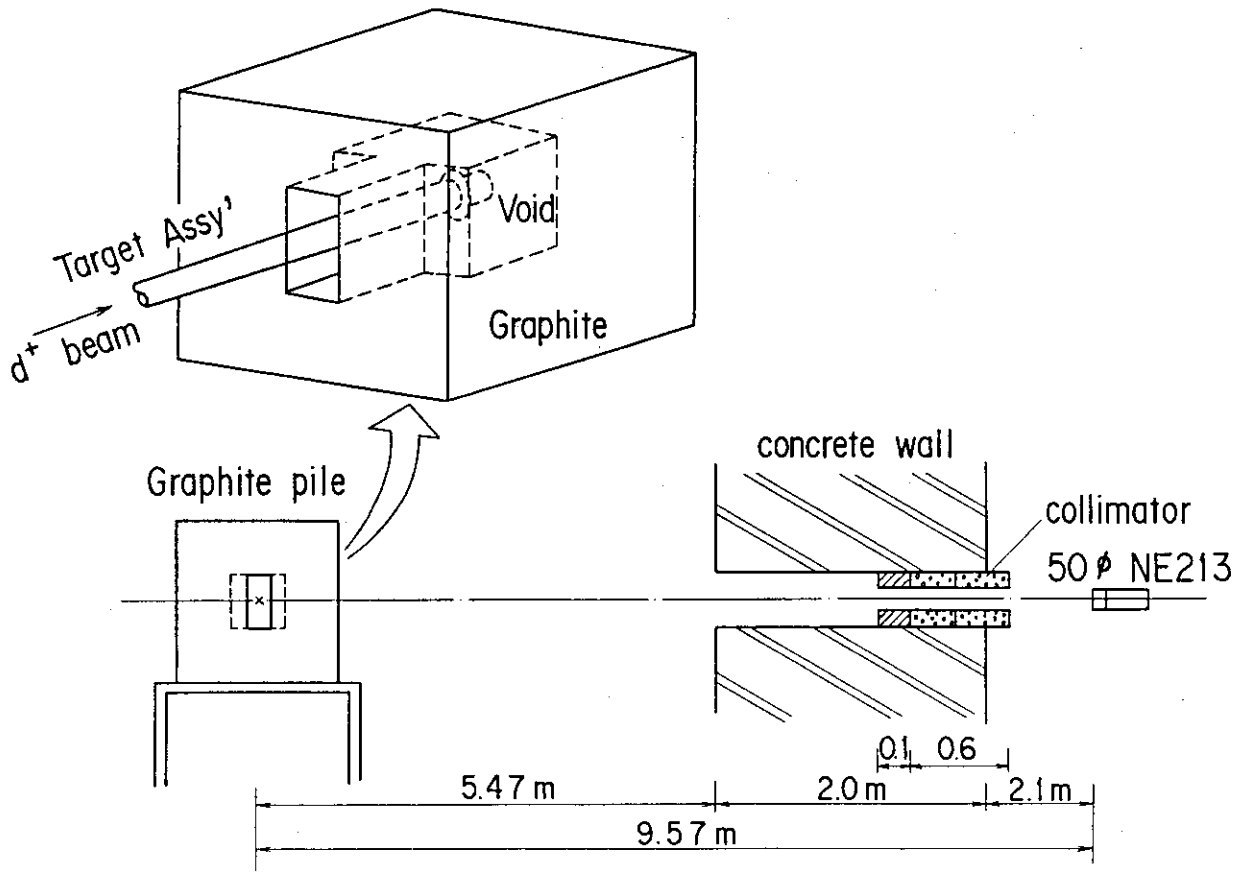

Fig. 3.3.8 Experimental setup for the measurement of the reference field produced by the graphite pile.

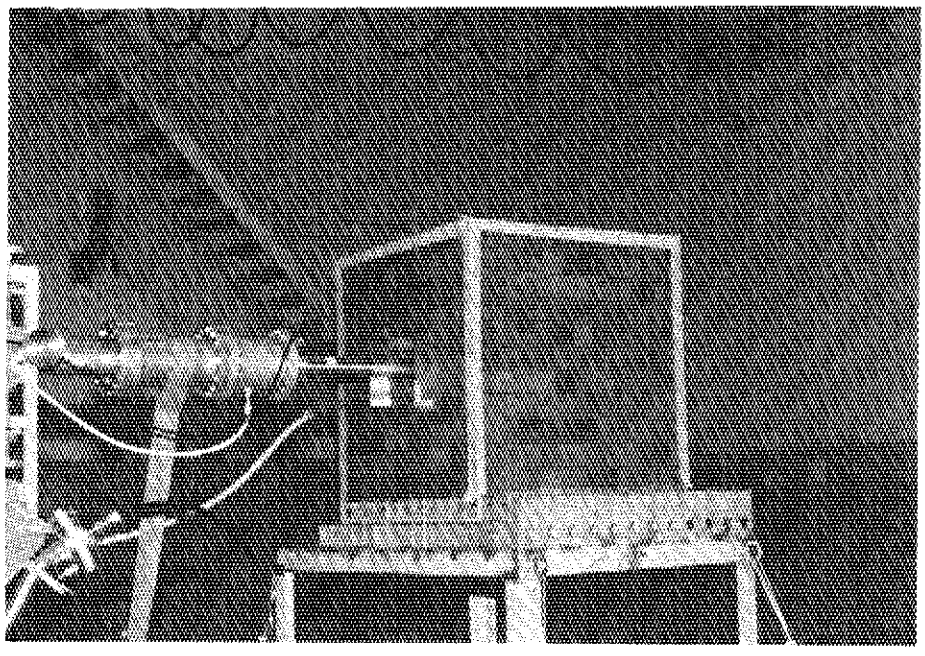

Fig. 3.3.9 Photograph of the graphite pile.

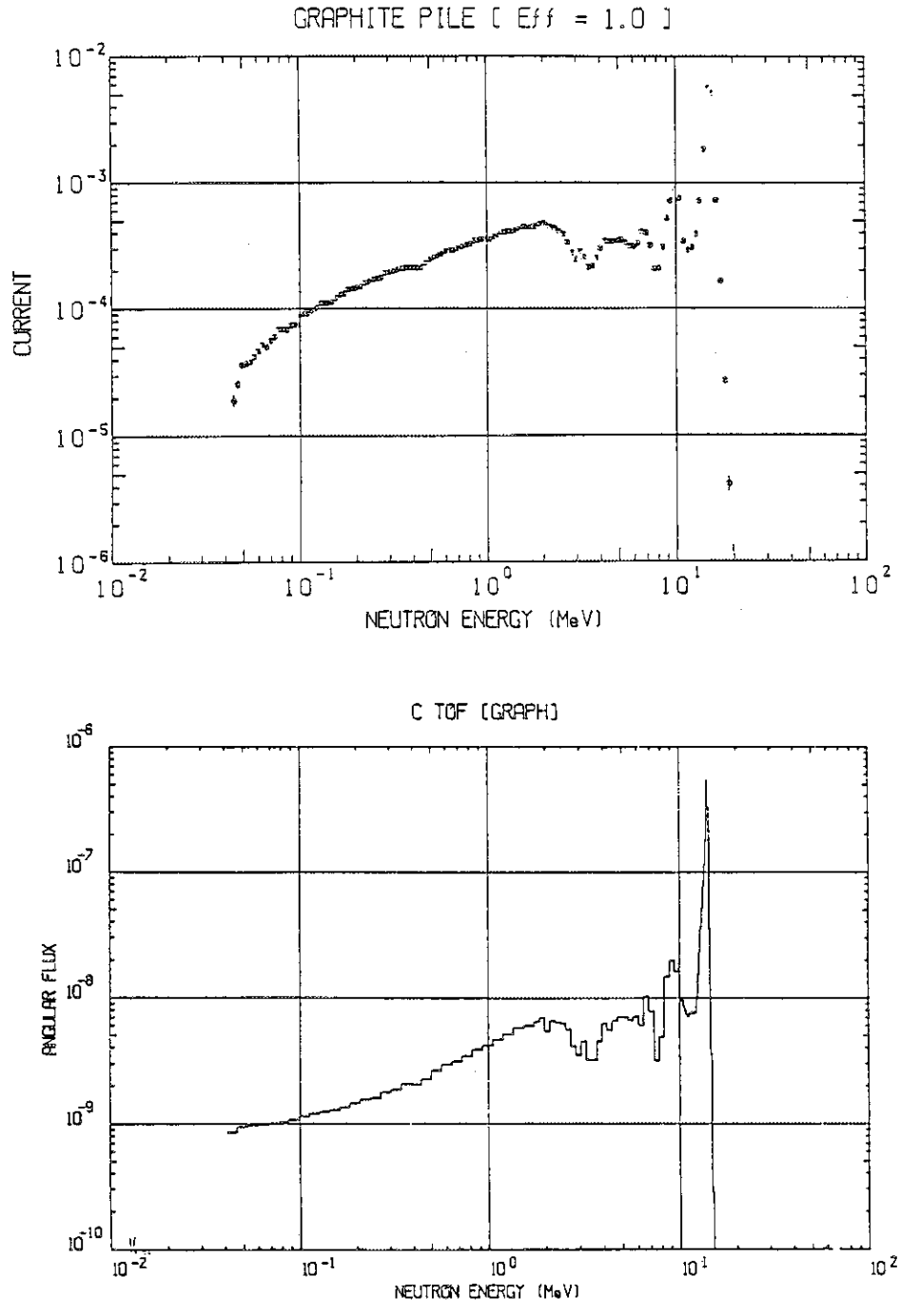

Fig. 3.3.10 (a) The measured raw spectrum for neutrons leaking from the graphite pile.

(b) The calculated spectrum for neutrons leaking from the graphite pile. The calculation was done by MORSE-DD with JENDL-3PR1 and simulated exactly for the experimental setup.

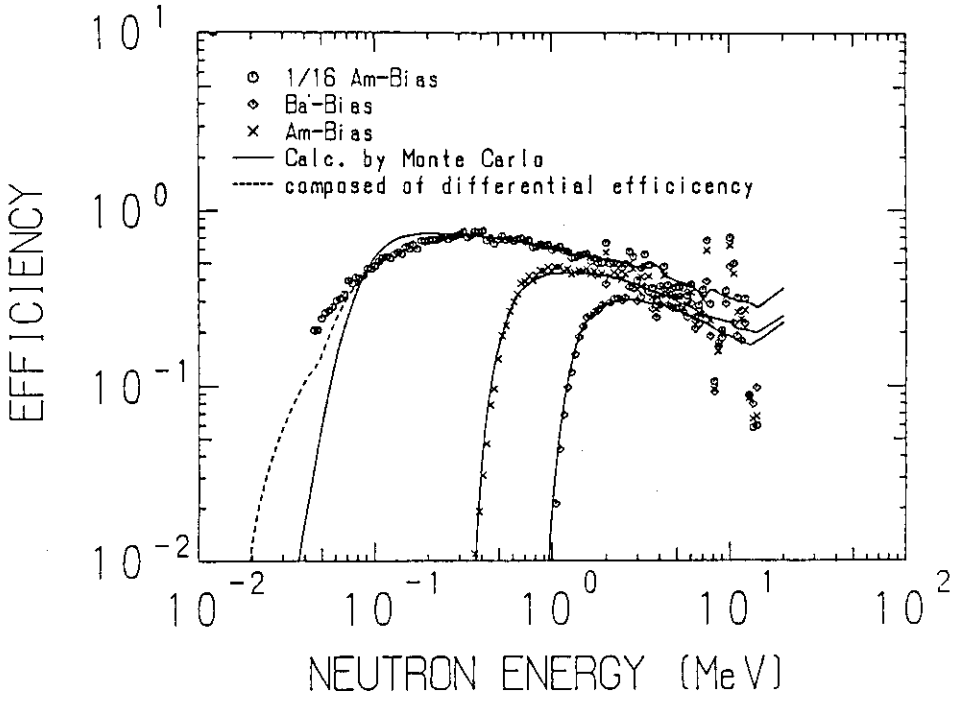

Fig. 3.3.11 Comparisons of the calculated efficiencies with the efficiencies obtained by the comparison method.

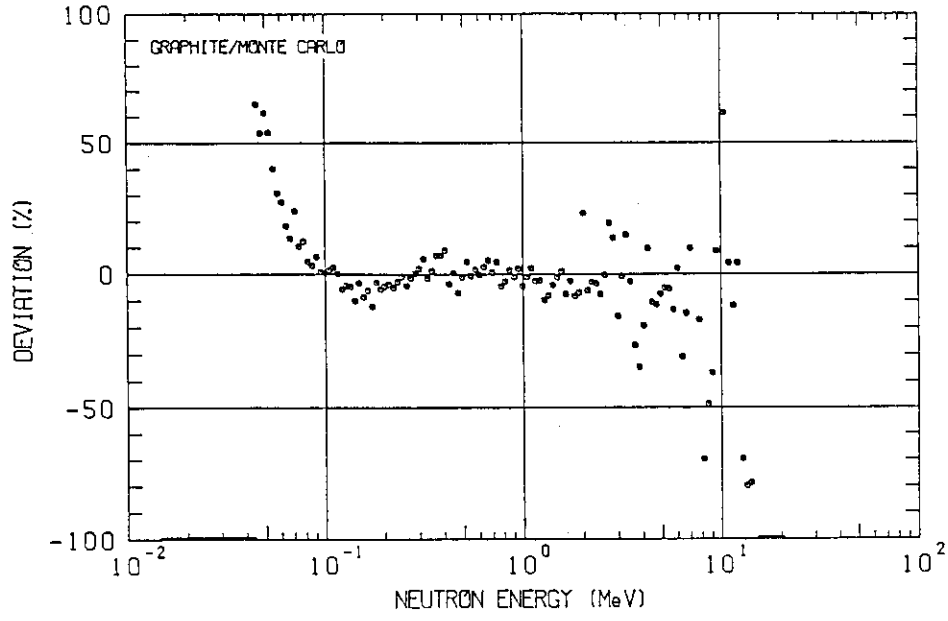

Fig. 3.3.12 Difference between the efficiencies determined by two kinds of methods.

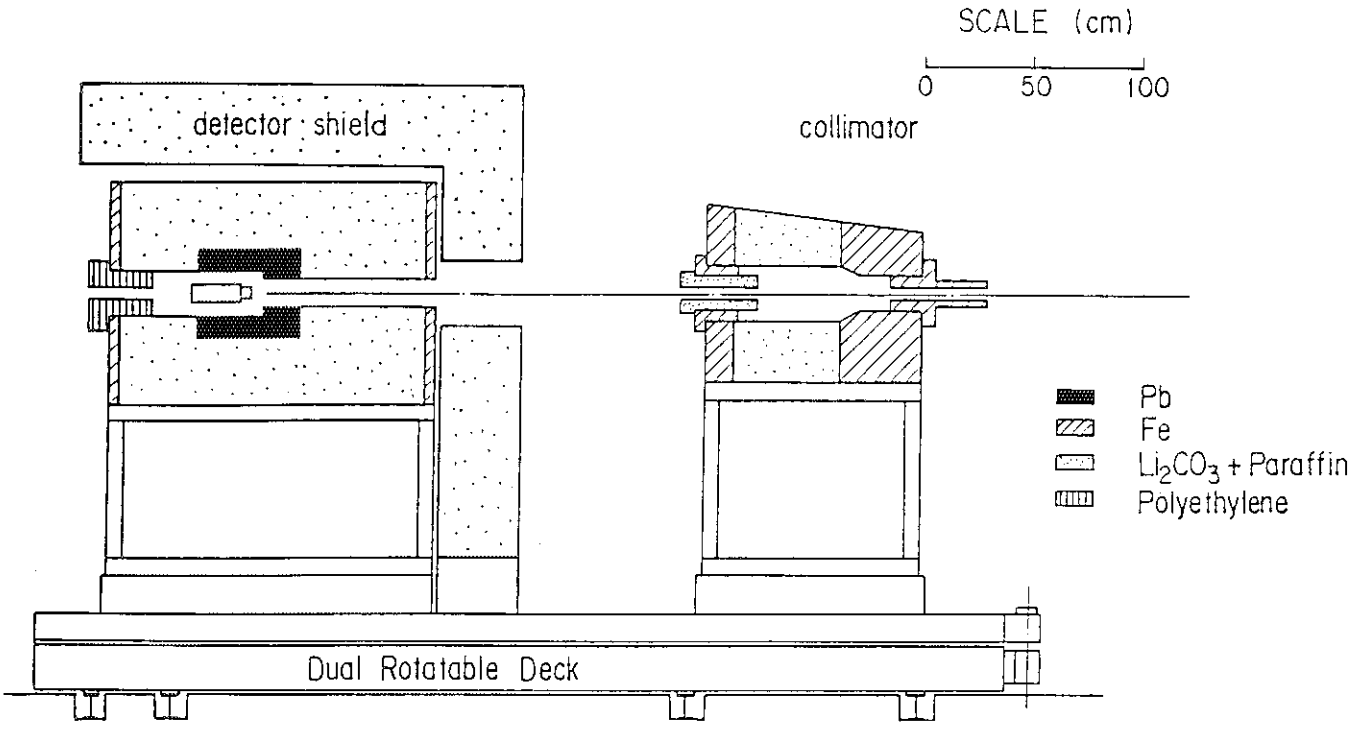

Fig. 3.4.1 Collimator and detector shield.

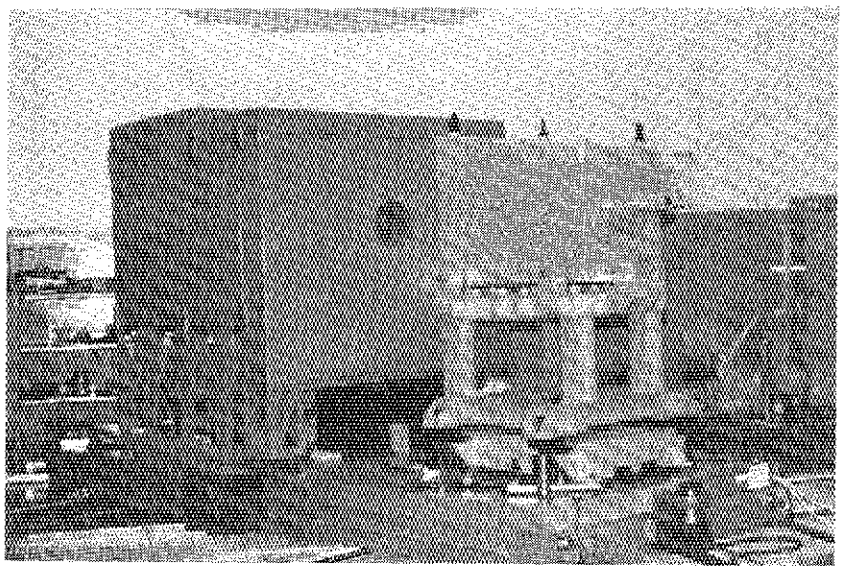

Fig. 3.4.2 Photograph of the collimator and the outer detector shield.

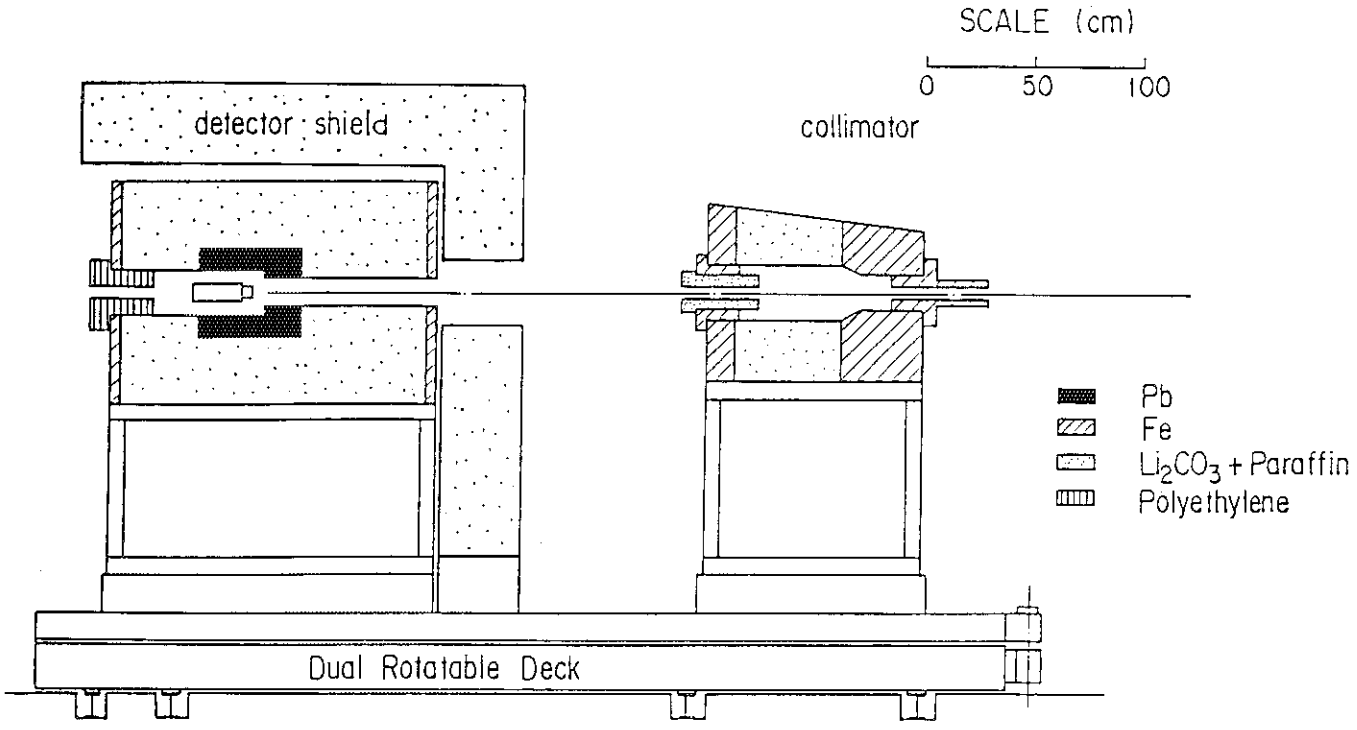

Fig. 3.4.1 Collimator and detector shield.

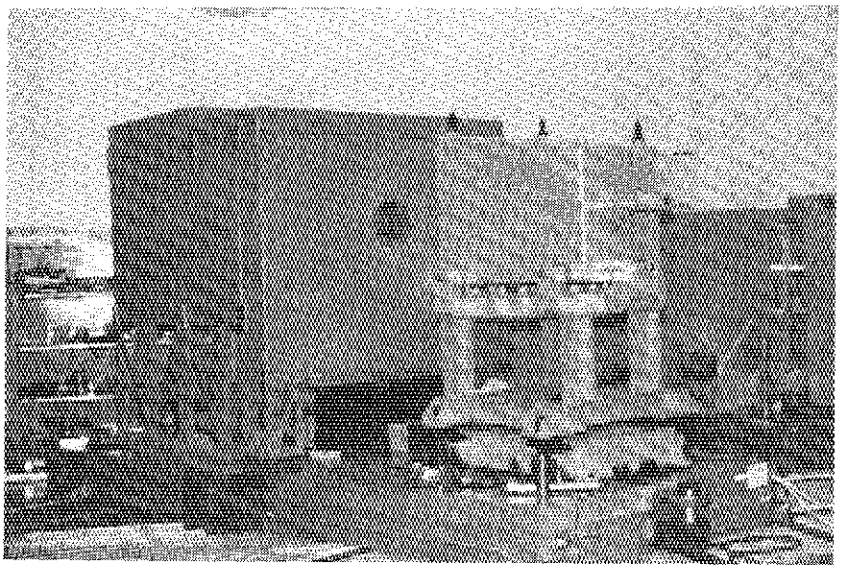

Fig. 3.4.2 Photograph of the collimator and the outer detector shield.

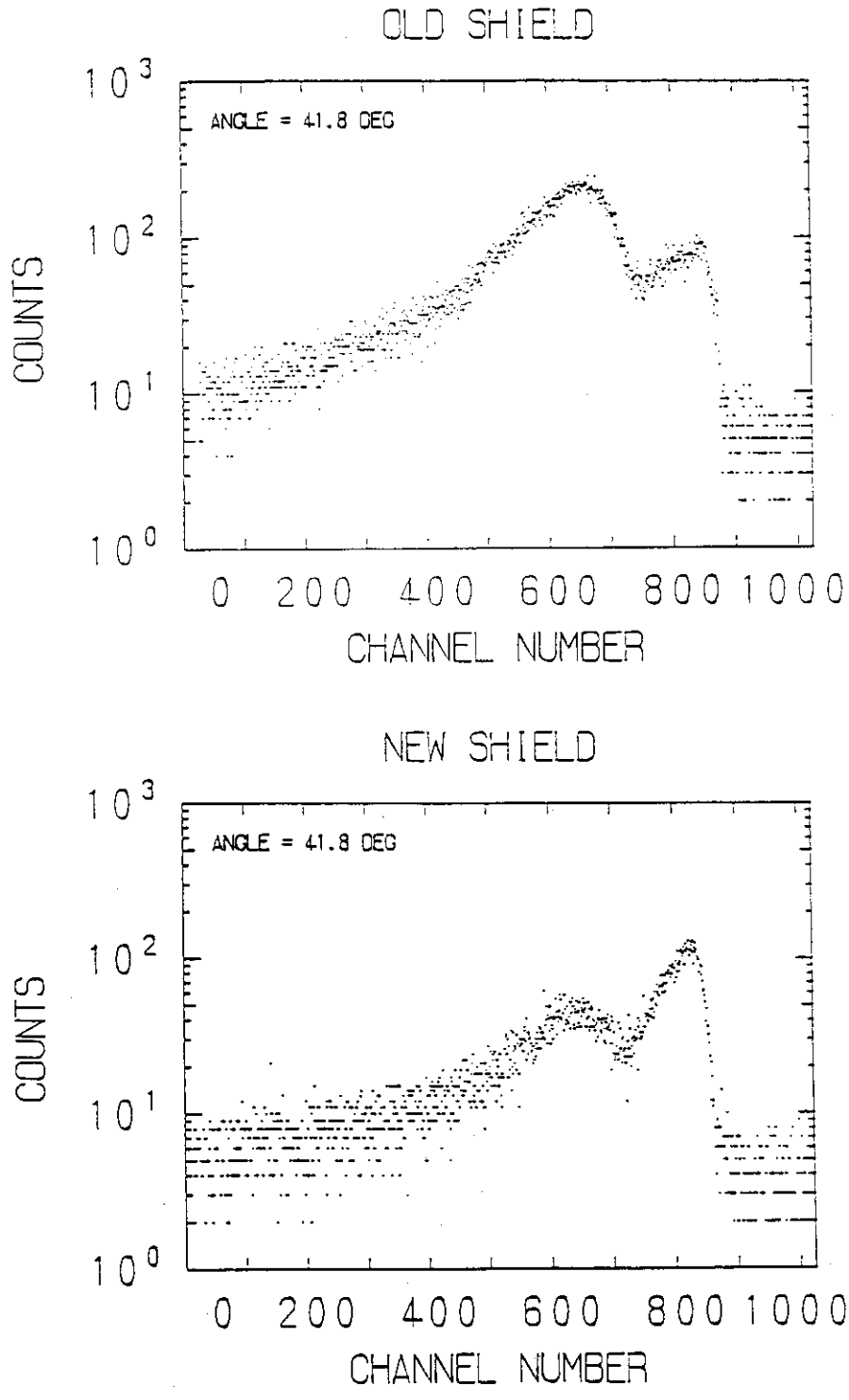

Fig. 3.4.3 Effect of the outer detector shield. The room return background below 700 channel (< 2 MeV) was reduced by the outer shield.

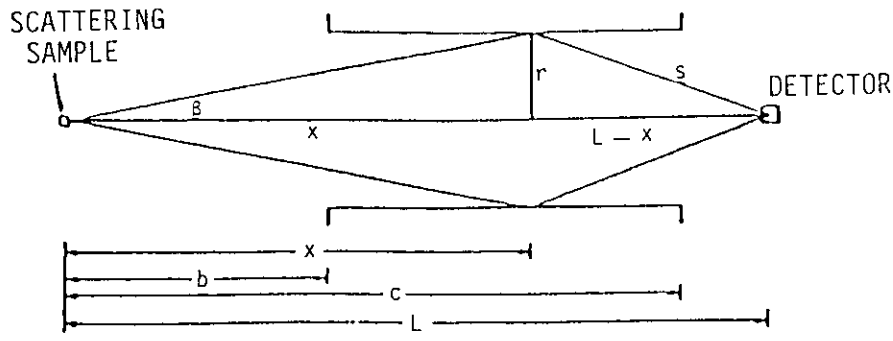

Fig. 3.4.4 Geometry for scattering from the surface of a cylindrical collimator.

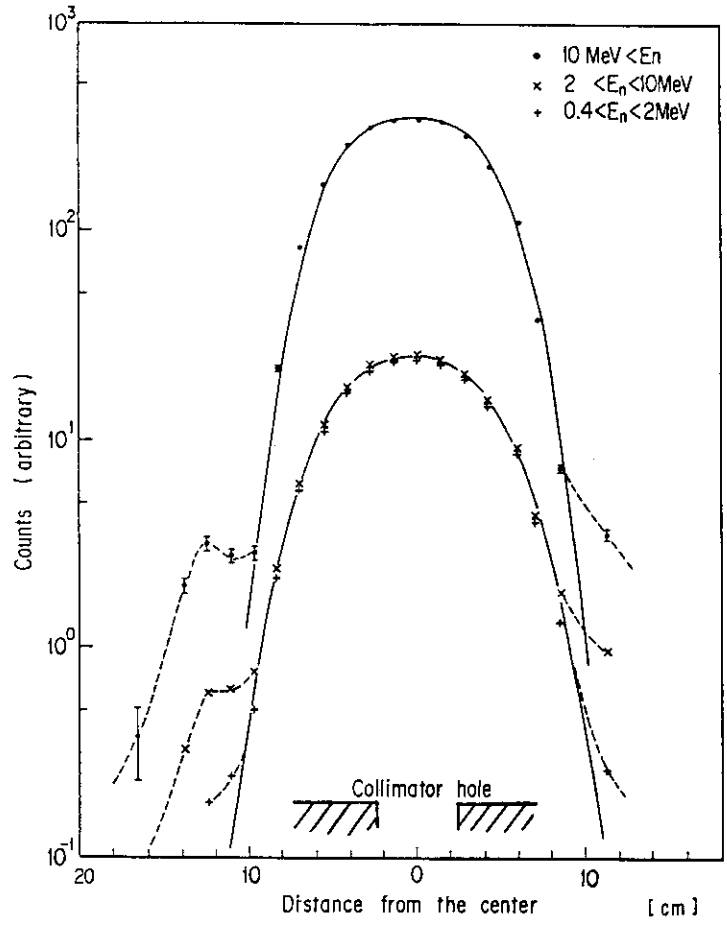

Fig. 3.4.5 The measured detector-collimator response function for the DT neutron source.

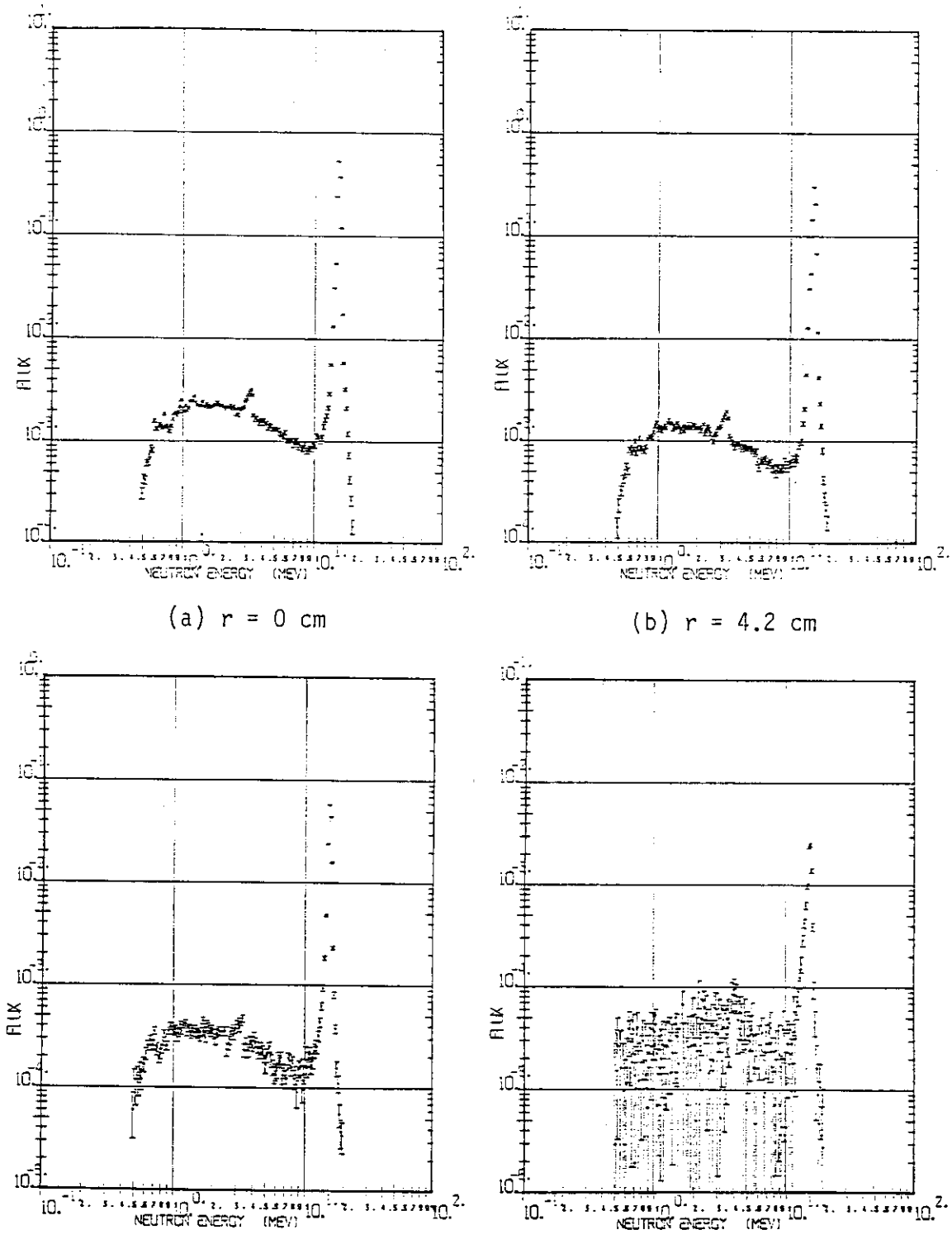

(a) r = 0 cm

(b) r = 4.2 cm

(c) r = 7.0 cm

(d) r = 11.2 cm

Fig. 3.4.6 Neutron energy spectra for various positions on the source surface from the DT source through the collimator.

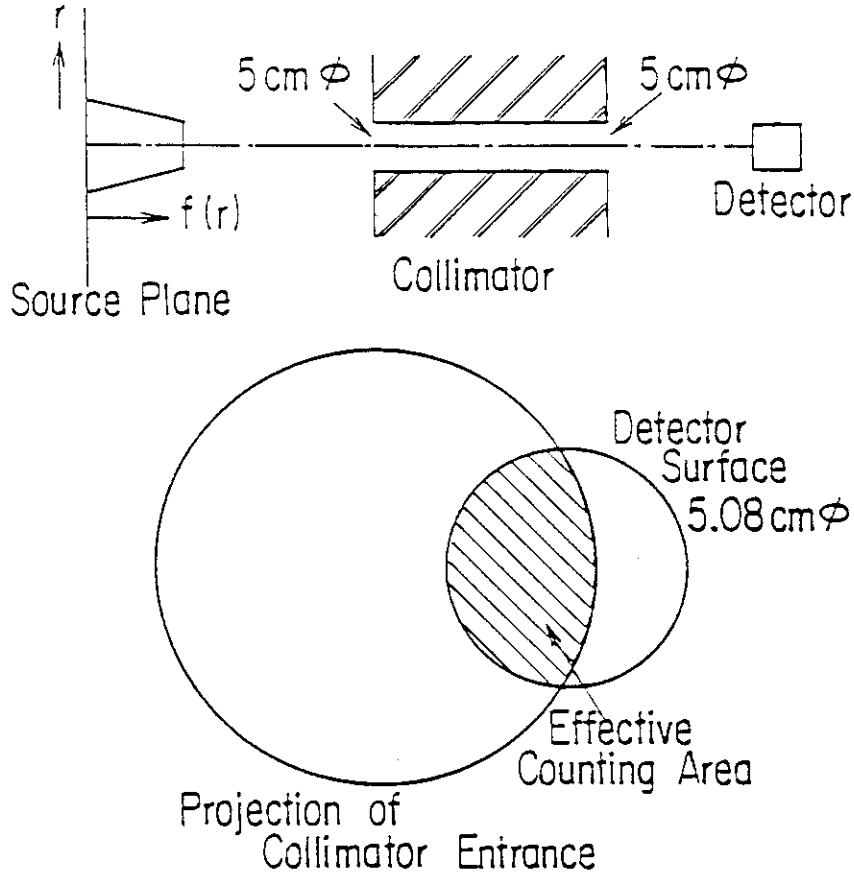

Fig. 3.4.7 Illustration of the detector-collimator response function.

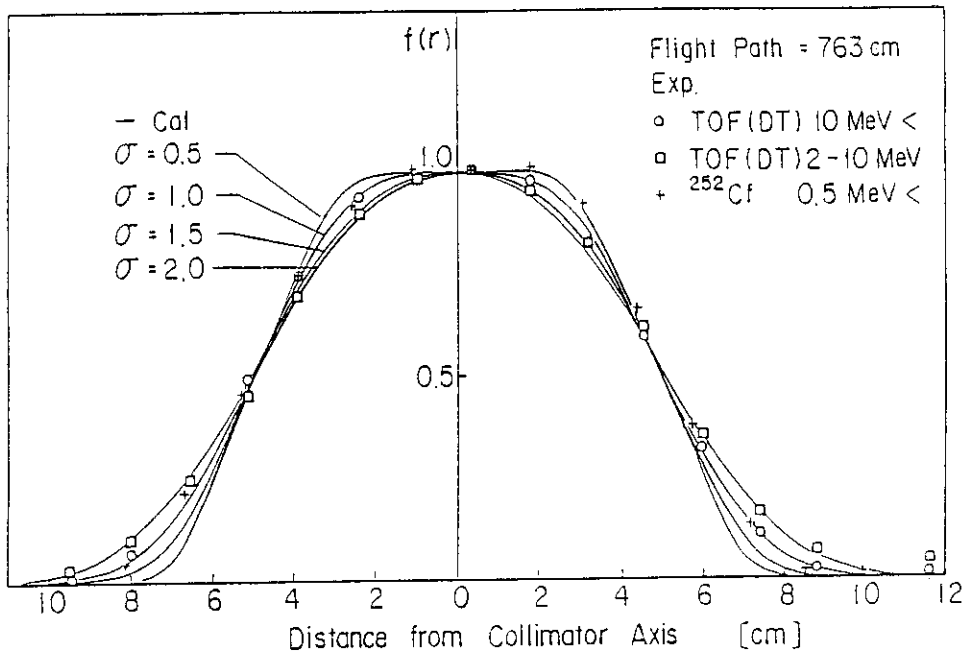

Fig. 3.4.8 Comparison of the measured response functions with the calculated ones.

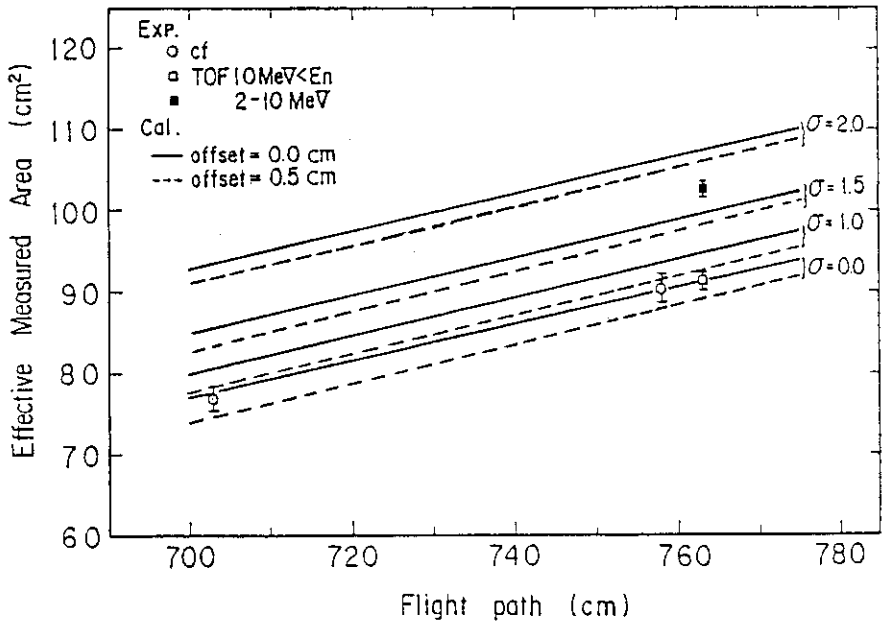

Fig. 3.4.9 Comparison of the effective measeued area with the calculated ones as a function of the destance between the detector and source (flight path).

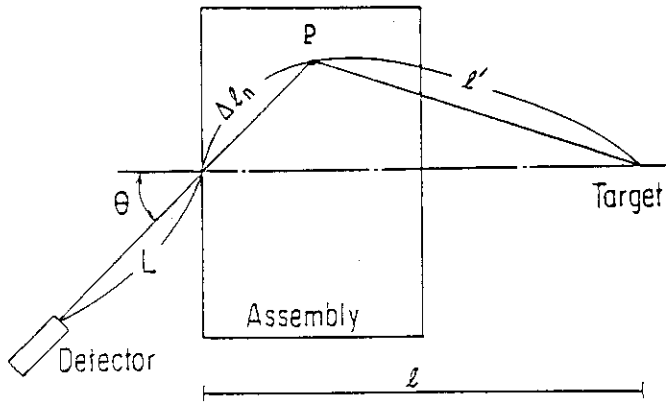

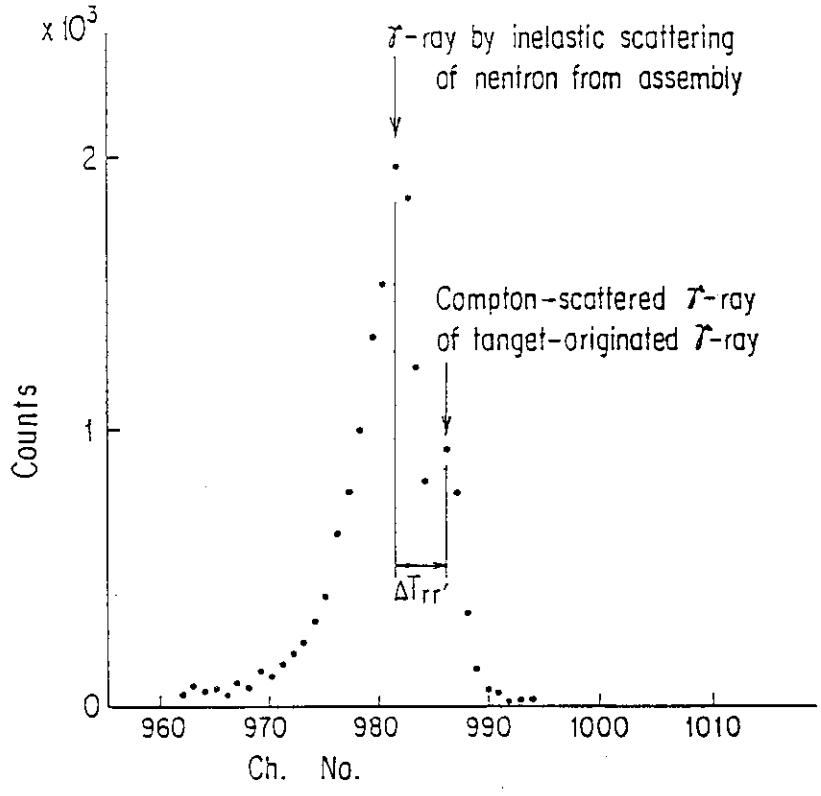

Fig. 3.5.1 Effective neutron emission depth determined by the gamma-rays emitted from the assembly.

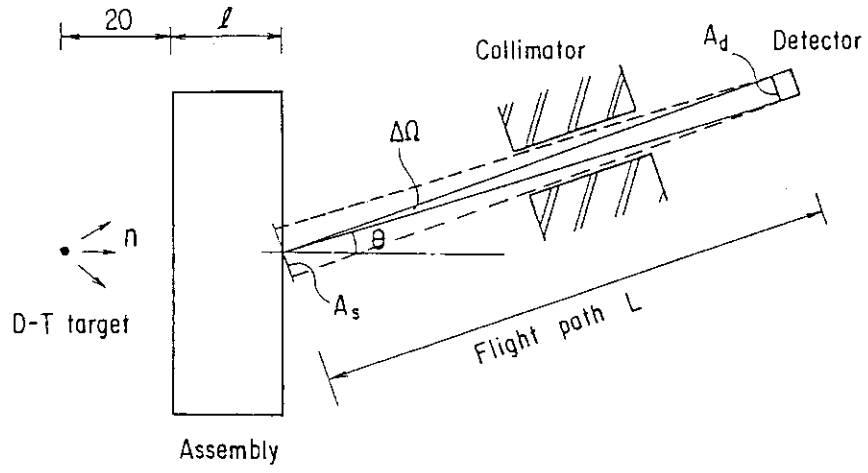

Fig. 3.5.2 Difinitions of the parameters for data reduction.

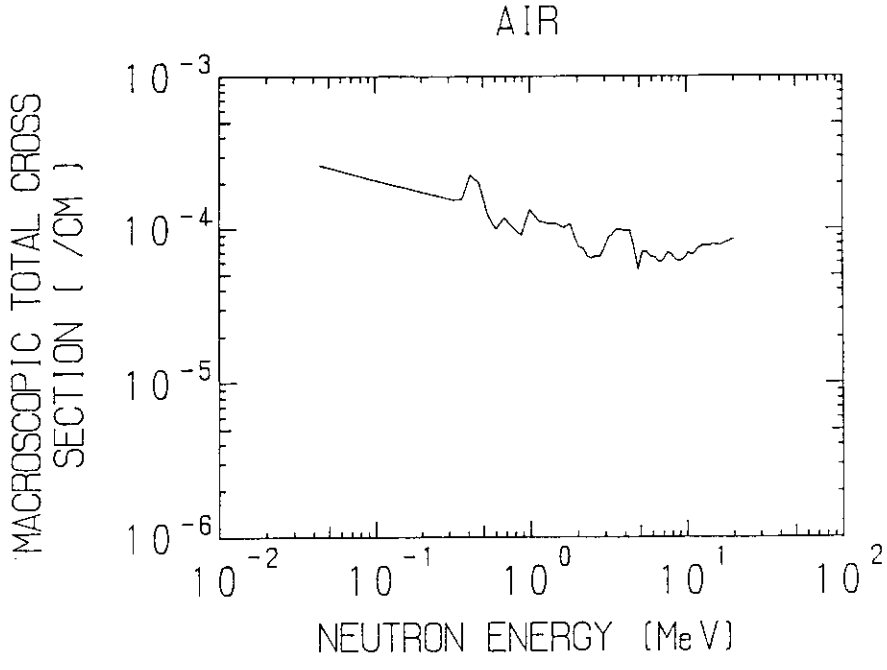

Fig. 3.5.3 Macroscopic total cross section of air used in the air attenuation correction.

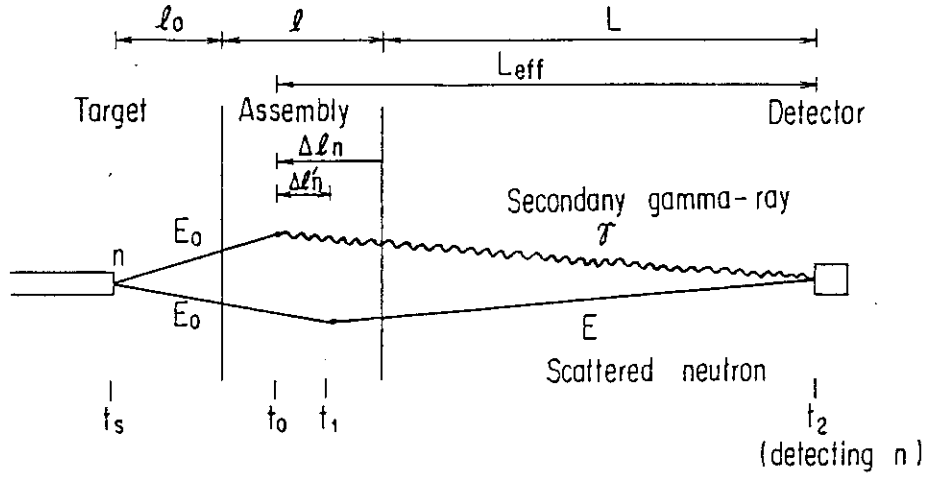

Fig. 3.6.1 Time relation of the observed neutrons and gamma-rays. The time t_s is the time origin obtained from the target by the beam pulse, t_0 and t_1 are the emission times of secondary gamma-rays and neutrons, and t_2 is the arrival time of the observed neutron. E_0 and E are energies of primary and secondary neutrons.

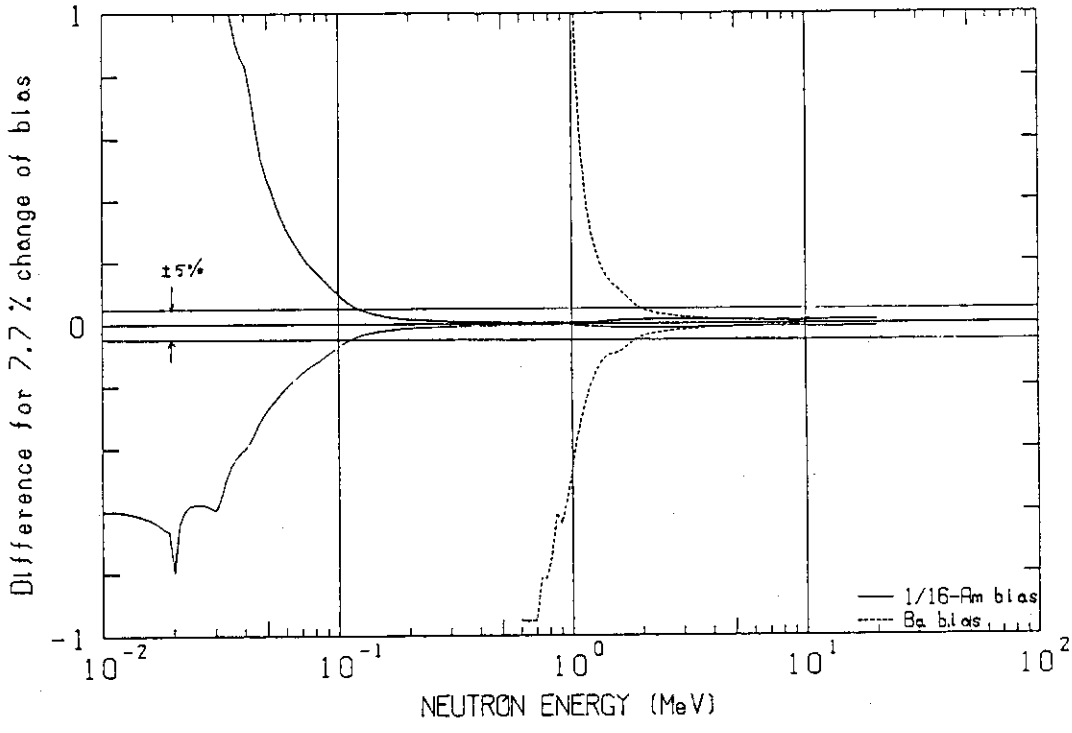

Fig. 3.6.2 Difference of the detection efficiency due to bias mismatch. The figure shows the case for the mismatch of 7.7 %.

4. Measurements of Angular Neutron FLux for Some Fusion Blanket Materials

4.1 Graphite Slab

4.1.1 Introduction

Graphite is one of the candidate materials as a neutron reflector in tritium breeding blankets for DT burning fusion reactors. Many cross section measurements[1],[2] have been performed on carbon for fission reactor development. Carbon cross sections are also, in fact, frequently used as a standard. In 1979, Wasson[3] reviewed the accuracy of carbon cross sections with following conclusions: The error in the total cross section was estimated to be less than 1 % below 2 MeV, about 2 % from 2.8 MeV to 8.5 MeV and about 4 % from 8.5 MeV to 15 MeV, respectively; the uncertainty of the angular distribution of the elastic cross section was also estimated to be less than 5 %, 3-5 % and 7 % for the respective energy ranges.

The accuracy of the total cross section seems to be sufficient even in the high-energy range, from the above review. However, several integral experiments[4]-[11] seem to indicate that the cross section data of carbon for fusion neutrons are still insufficient. In addition, a cross section sensitivity analysis[9] for a Li_2O-C sphere experiment[8] revealed that graphite has a large sensitivity to the experimental result and recommended an integral test, using a simple graphite assembly. On the other hand, new evaluations such as JENDL-3PR1 and -3PR2[12], have been proposed based on the new cross section data.

Graphite slab has been chosen for measurement because it is the best material for examining the performance of the present experimental system. In addition, carbon cross section is expected to have a better accuracy than that for other materials, and an experimental assembly containing a single element can be easily realized. The calculations were performed by the MCNP code[13] using the JENDL-3PR1, -3PR2 and ENDF/B-V[14] nuclear data files.

4.1.2 Measurement

Three carbon slab assemblies were made from rectangular blocks of graphite with 50.6 mm square base and 50.6, 101.2 or 202.4 mm heights, in a cylindrical configuration. The graphite blocks were selected by weight so that the density deviation was within 2 %. The average density of the blocks was 1.632 Mg/m^3. The thicknesses of the slab assemblies were 50.6, 202.4 and 404.8 mm, corresponding to 0.6, 2.4 and 4.8 mean free paths for 15 MeV neutrons, respectively. The area-equivalent radius of the pseudo-cylinder made by the blocks was 314 mm. The measuring angles were 0, 12.2, 24.9, 41.8 and 66.8 degrees, corresponding to the angles of the S_{16} quadrature set used in discrete-ordinate neutron transport codes, e.g., DOT3.5.[15]

The pulse width, peak current and pulse duration of the accelerated deuteron beam were 2 ns, 18 mA and 2 μs, respectively. In this measurement, the detector biases were set to the peak of ^{241}Am gamma-rays for low bias and the Compton half-height edge of ^{137}Cs gamma-rays for high bias, corresponding to the measuring energy range of 0.5 to 15 MeV. This higher setting of the low bias aimed at measuring the TOF spectrum at a high count rate by use of a 500 kHz pulse repetition rate. Figure 4.1.1 shows typical time spectra obtained by the present time-of-flight system. The flight-time ranges for the high and low biases are 500 ns and 1 μs, respectively.

4.1.3 Results

The measured angular flux spectra are shown in Figs. 4.1.2-4.1.4 for the slabs of three thicknesses. Error bars in the results represent only the statistical errors. Measurement degrees was not performed at 12.2 degrees for the 50.6 mm-thick slab, because the tritium target was seen through the collimator at that angle. The energy spread observed in the measured spectra can be interpreted as the sum of the intrinsic spread of ∿4 % due to kinematics in the tritium-titanium target layer, of the detecting resolution less than 1 ns, and of the beam pulse width of 2 ns, corresponding to a 2 % resolution for 15 MeV neutrons.

In the spectra, four obvious peaks are noted. The first three of these correspond to the inelastic scattering peaks from the 4.44 MeV,

7.65 MeV and 9.64 MeV levels in ^{12}C, respectively. The forth peak around 3 MeV is due to neutrons from the parasitic $^{2}D(d,n)^{3}He$ reaction. Below 4 MeV, the spectra are very smooth.

Figure 4.1.5 show angular dependences of the measured flux integrated over the following energy regions (which depend on the reactions that chiefly contribute to those regions): (A) $E_n > 11.4$ MeV, composed of elastically scattered neutrons; (B) $7.8 < E_n < 11.4$ MeV, (C) $5.9 < E_n < 7.8$ MeV and (D) $4.2 < E_n < 5.9$ MeV, composed of neutrons inelastically scattered with excitation of the 4.44 MeV, 7.65 MeV and 9.64 MeV levels in ^{12}C, respectively; (E) $0.48 < E_n < 4.2$ MeV, mainly composed of neutrons inelastically-scattered from the higher levels in ^{12}C and multiply-scattered neutrons. It should be noted that the 0-degree fluxes have different characteristics from other angles because they include the uncollided neutrons, i. e., the 0-degree flux relates strongly to the total cross section. In the figure, the value exclusive of the uncollided flux are shown as black symbols, as obtained from the Monte Carlo calculation described later.

The fluxes of both 0.6 and 2.4 mfp results are almost the same order, while the 4.8 mfp results are smaller by ten times. Angular dependences of the region (A) are almost the same for three thickness. In the low energy regions, the 0.6 mfp case show the same trend as differential cross section of inelastic scatterings, but these patterns disappear with increasing the thickness. For the 4.8 mfp case, the angular dependence of the other energy regions come to be similar to that of the region (A).

From the 0.6 mfp results, it is suggested on the angular dependence of the partial cross sections of ^{12}C that the second level (Q_2 = -7.65 MeV) is different from the JENDLs but close to the ENDF/B-V, and the third level (Q_3 = -9.64 MeV) is not flat as the data in the present files.

4.1.4 Discussions

Comparison with calculation

The experimental results were analyzed by the Monte Carlo code MCNP[13], using pointwise cross sections. These carbon cross section data for the MCNP calculation was retrieved from the cross section

library FSXLIB[16] which was produced by the processing code NJOY[17] for ACE format and the editing code MACROS[16], from the JENDL-3PR1, -3PR2[12] and ENDF/B-V[14] nuclear data files.

The calculational model is described in appendix. Five point estimator detectors were placed at the same time in the actual positions corresponding to the measuring angles. The collimator was simulated using a no-importance region in which neutron history was immediately terminated. Neutron histories were accumulated to obtain statistics within 5 % fsd (fraction of standard deviation).

The measured neutron spectrum emitted from the target was adopted as the source neutron spectrum input, assuming an isotropic angular distribution. The source intensity was normalized to the integration of the forward spectrum over 4π solid angle. Since the calculated results already involved the source neutron energy spread by use of the measured source spectrum, additional smearing of the calculated results with the energy resolution was not necessary. The energy spread due to variation of neutron flight path length, however, was not included, and thus experimental results might be slightly shifted with respect to the calculated spectra.

The spectrum comparisons are shown in Figs. 4.1.6-4.1.8 for three slab thicknesses. There is essentially no difference at 0 degrees among the results calculated by three files. They show excellent agreement with the experiment for three slabs. At other angles, small differences are seen in 4-8 MeV region. The calculations by JENDL-3PR1 and -3PR2 overestimate the second and third inelastic peaks of 7.65 MeV and 9.64 MeV levels. The ENDF/B-V slightly underestimates the third inelastic peak. These discrepancies, however, are obscured with a increase of the slab thickness. In Fig. 4.1.8, we can see that the calculations show fairly good agreement as a whole.

Ratio of the calculation to the experiment

The calculated-to-measured value ratios (C/E), by the three nuclear data files for the three thicknesses of the slab, are shown in Fig. 4.1.9 for the above energy regions. Three files show similar trends for the regions (A),(B) and (E). The JENDLs are similar for (C) and (D), though they show poor agreement in these regions.

The angular dependence of C/E ratios for the 50.6 mm-thick slab reflects the secondary neutron emission spectra due to reaction by the incident 14.8 MeV neutrons. From the figure, it is seen that:

(1) Three nuclear files overestimate the elastic reaction neutrons (region A), by 30 % at 40 degrees.

(2) For inelastic scattering by the 7.65 MeV level in ^{12}C (region C), the JENDL-3PR1 and -3PR2 overestimate the neutron flux at angles between 20 and 40 degrees, and underestimate it at 66.8 degrees, while the ENDF/B-V is rather good except for the underestimation at 66.8 degrees.

(3) For inelastic scattering by the 9.64 MeV level in ^{12}C (region D), the JENDLs overestimate the emission neutrons above 20 degrees, while the ENDF/B-V is good.

As a whole, ENDF/B-V calculations show better trend of the angular dependence of the C/E compared with the JENDLs.

As for the thickness dependence, the three files show the same trends for the 50.6 mm-thick slab in the elastic scattering region (A), but different trends for the thicker slabs. For the 404.8 mm-thick slab, the JENDLs underestimate the flux at large angles, while the ENDF/B-V show good agreement. The cross section data of carbon in the present files are summarized in Table 4.1.1. Since, there is no difference in the angular distribution of elastic cross section, the increase of the elastic cross section might be one of the reasons that the ENDF/B of the region (A) for the 4.8 mfp case came to be better with increasing the thickness.

In the low energy regions with large discrepancies, the three files show the same C/E trends in the region (B) for the 404.8 mm-thick slab, while the deviation in the regions (C) and (D) of the JENDLs decrease with an increase of the thickness. This tendency of a C/E deviation can be attributed to neutrons scattered down from higher energy regions: the initially scattered neutrons of low energy are buried in the neutrons down-scattered by elastic reaction whose number is larger than that of neutrons going out of the region (C) and (D).

From the point of view of the integral experiment, the neutron spectrum in the thicker graphite slab is formed by neutrons slowing down in the slab as seen from the contribution flux distribution in chapter 2. Since a large number of neutrons is staying in the elastic

region (A), the C/E trend in the lower energy region is finally dominated by elastic scattering for the incident DT neutrons. As seen in Fig. 4.1.5, the low energy regions of the 4.8 mfp case followed the angular dependence of the region (A). Hence the importance from the primary reactions other than the elastic reaction come to be relatively smaller at the deep positions.

4.1.5 Conclusion

Angular neutron fluxes from the graphite slab have been obtained in the energy range from 0.5 to 15 MeV at angles from 0 to 66.8 degrees. The flux was calculated and the carbon data of JENDL-3PR1, -3PR2 and ENDF/B-V nuclear data files were examined by MCNP calculations.

The results of the comparison can be summarized as follows: The angular distributions for the elastic scattering in all three files, and some inelastic scattering in the JENDLs, are incorrect for 14.8 MeV neutrons; these discrepancies, however, decrease with a increase of the thickness.

Consequently, the carbon data in the present nuclear data files showed good agreements with the measured results within 5 % at the forward for the 4.8 mfp thickness. Hence, they are sufficient for practical use in a fusion reactor shielding design in which a neutron penetration is more important. However, for use in a blanket reflector design, where the backward scattering is relatively important, the deviation of the C/E for the region (A) at large angle may affect the the estimation of neutrons reflected on carbon.

References

1) Haouat G., et al.: Nucl. Sci. Eng., 65, 331 (1978)
2) Cierjacks S., et al.: Nucl. Instrum. Methods, 169, 185 (1980)
3) Wasson O. A.: "Neutron Cross Section Standards," Proc. Int. Conf. on Nuclear Cross Sections for Technology, knoxiville, Tennessee, 1979, NBS Spec. pub. 594, pp. 720 (1980)
4) Maekawa H., et al.: Nucl.Sci. Eng., 57, 335 (1975)
5) Hansen L. F., et al.: Nucl. Sci. Eng., 60, 27 (1976)
6) Seki Y., et al.: J. Nucl. Sci. Technol., 14, 210 (1977)
7) Seki Y., et al.: ibid.,14, 680 (1977)

8) Maekawa H., et al.: ibid, 16, 377 (1979)

9) Oyama Y., et al.: "Cross Section Sensitivity Analysis of ^{235}U and ^{238}U Fission Rates in a Graphite Reflected Lithium Oxide Assembly," JAERI-M 8870 (in Japanese) (1980)

10) Tsechanski A.: Nucl. Sci. Eng., 84, 226 (1983)

11) Sekimoto H., et al.: J. Nucl. Sci. Technol., 22, 174 (1985)

12) Shibata K.: "Evaluation of Neutron Nuclear Data for ^{12}C," JAERI-M 83-221 (1983)

13) Los Alamos Radiation Transport Group (X-6): "MCNP-A General Monte Carlo Code for Neutron and Photon Transport," LA-7396-M, Revised (April 1981)

14) "ENDF/B-V: Evaluated Nuclear Data File, Version-V," BNL-17541 (ENDF-201) (1979)

15) Rhoades W. A., et al.: " The DOT-III Two Dimensional Discrete Ordinates Transport Code," ORNL/TM-4280 (1973)

16) Kosako K.: "Cross Section Libraries for Analysis of Experiment at FNS," to be published in JAERI-M report.

17) MacFarlane R. E., et al.: "The NJOY Nuclear Data Processing System," LA-9303-M,(1982)

Table 4.1.1 Carbon cross section for 15 MeV neutrons in the nuclear files

Reaction	J-3PR1	J-3PR2	ENDF/B-V	
total	1412.7 mb	1412.7 mb	1410 mb	
elastic	832.6 mb	851.9 mb	866.7	
inelastic				
4.44 MeV	153.5 mb	153.5 mb	165 mb	
7.65	15 mb	15 mb	9.2 mb	
9.64	96.5 mb	77.2 mb	52.4	
10.3	-	-	5.9	232.1 mb
10.8	-	-	18.3	
11.3	not assigned	not assigned	41.2	
11.8	-	-	43.7	
12.3	-	-	39.1	
12.8	-	-	35.1	
13.3	-	-	19.4	
Continuum	241.6 mb	241.6 mb	29.4	

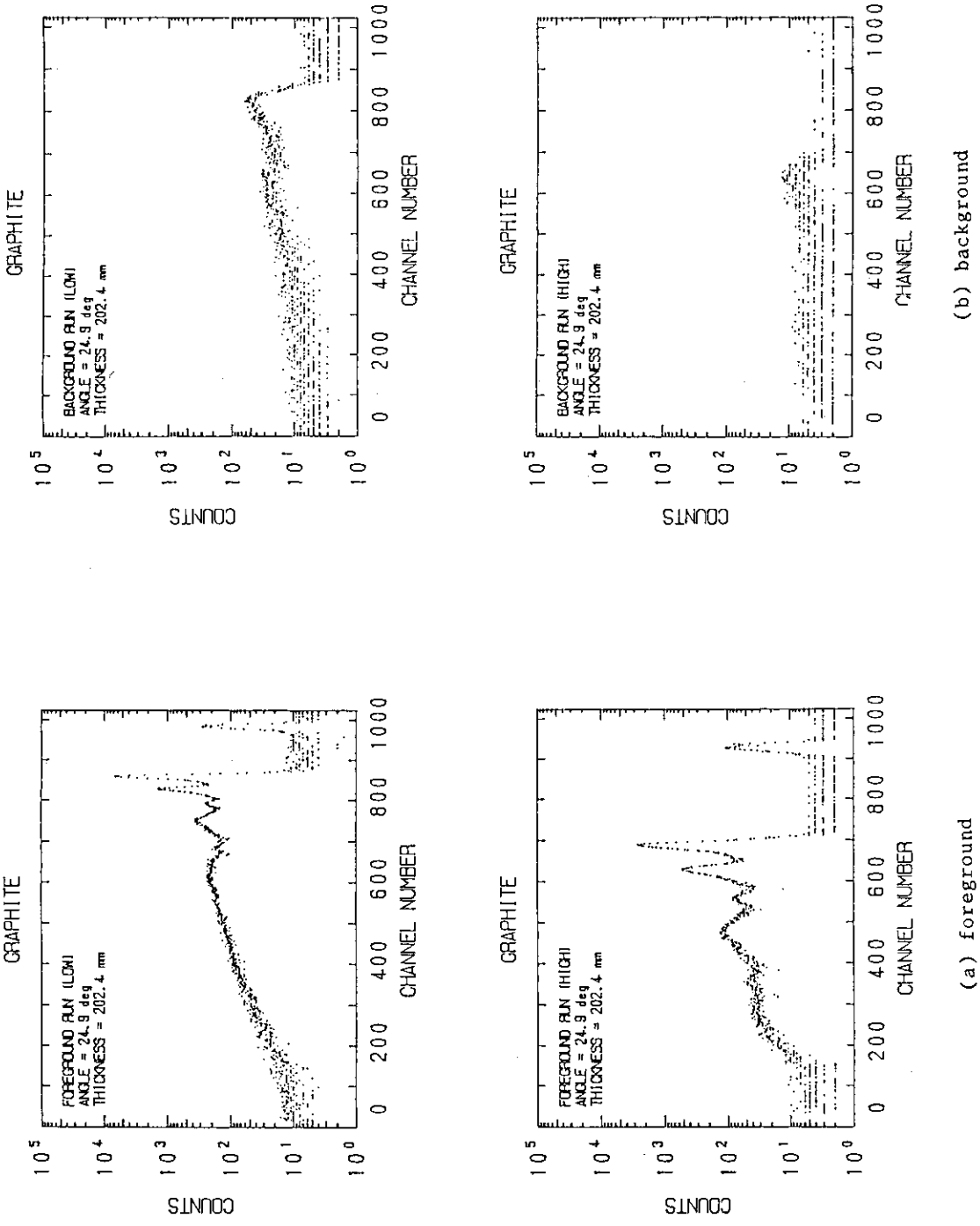

(b) background

(a) foreground

Fig. 4.1.1 Typical time spectra observed on the graphite slab

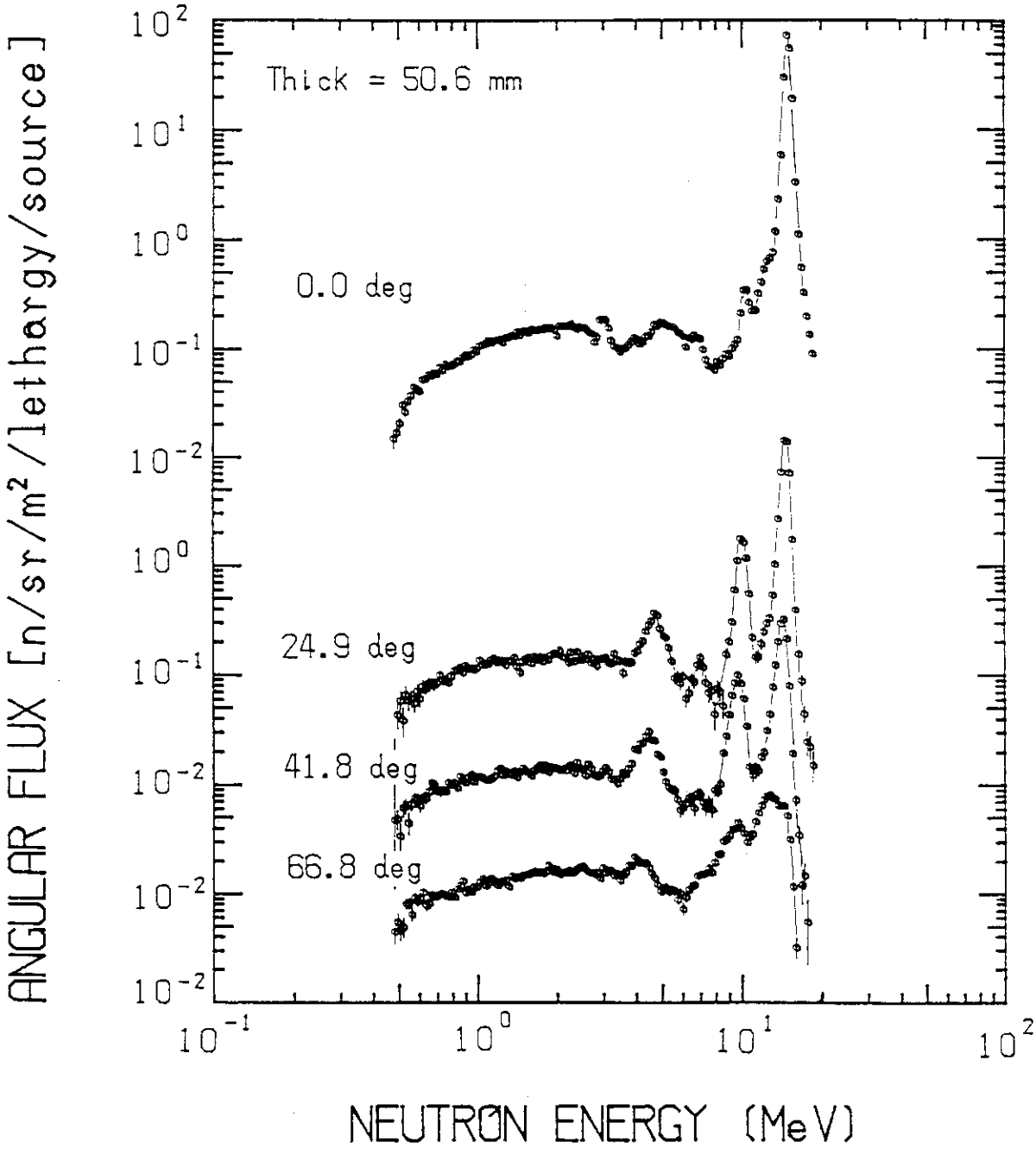

Fig. 4.1.2 Measured spectra of angular flux for the 50.6 mm-thick graphite slab. Error bars include only statistical error due to neutron counts.

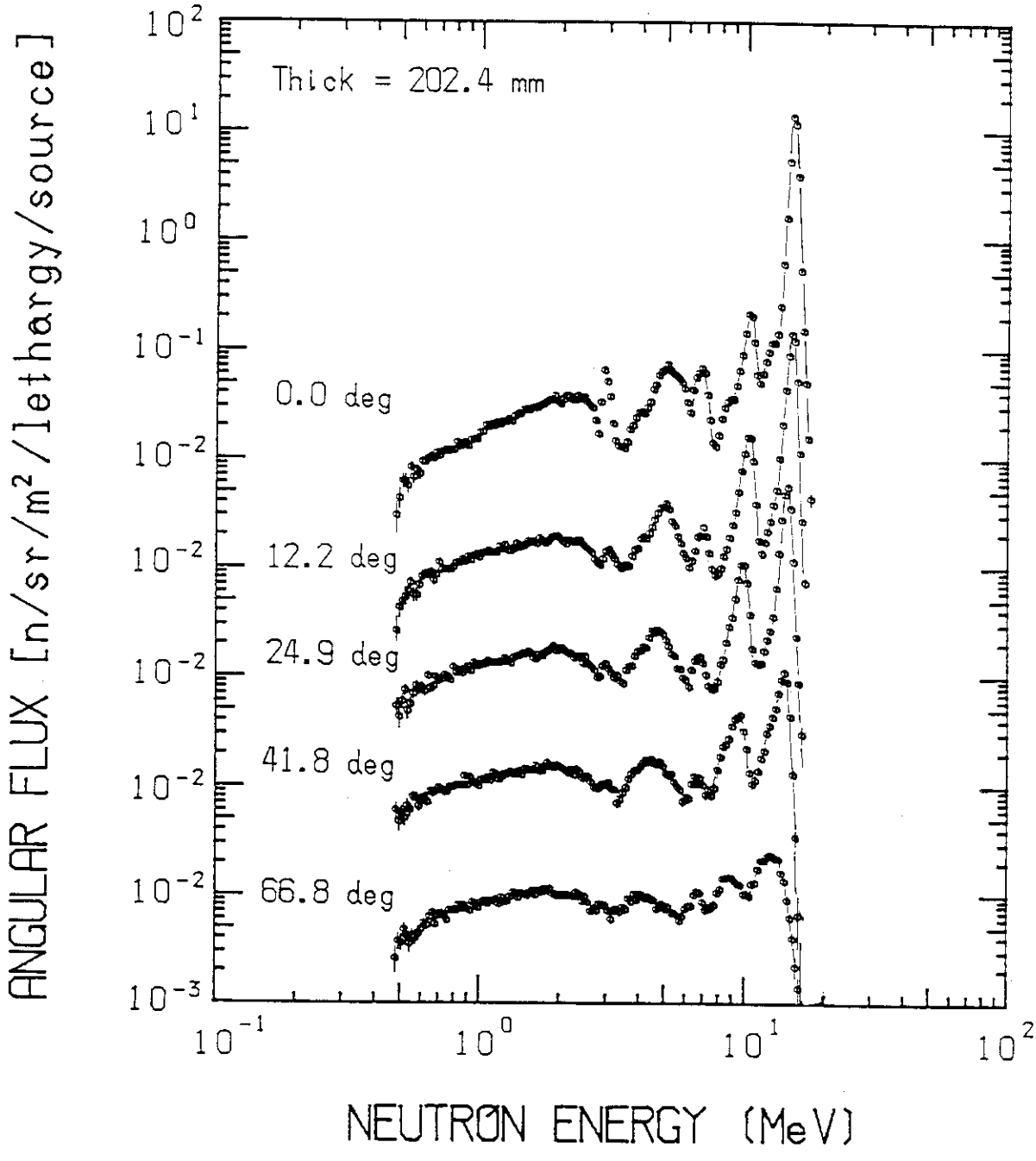

Fig. 4.1.3 Measured spectra of angular flux for the 202.4 mm-thick graphite slab. Error bars include only statistical error due to neutron counts.

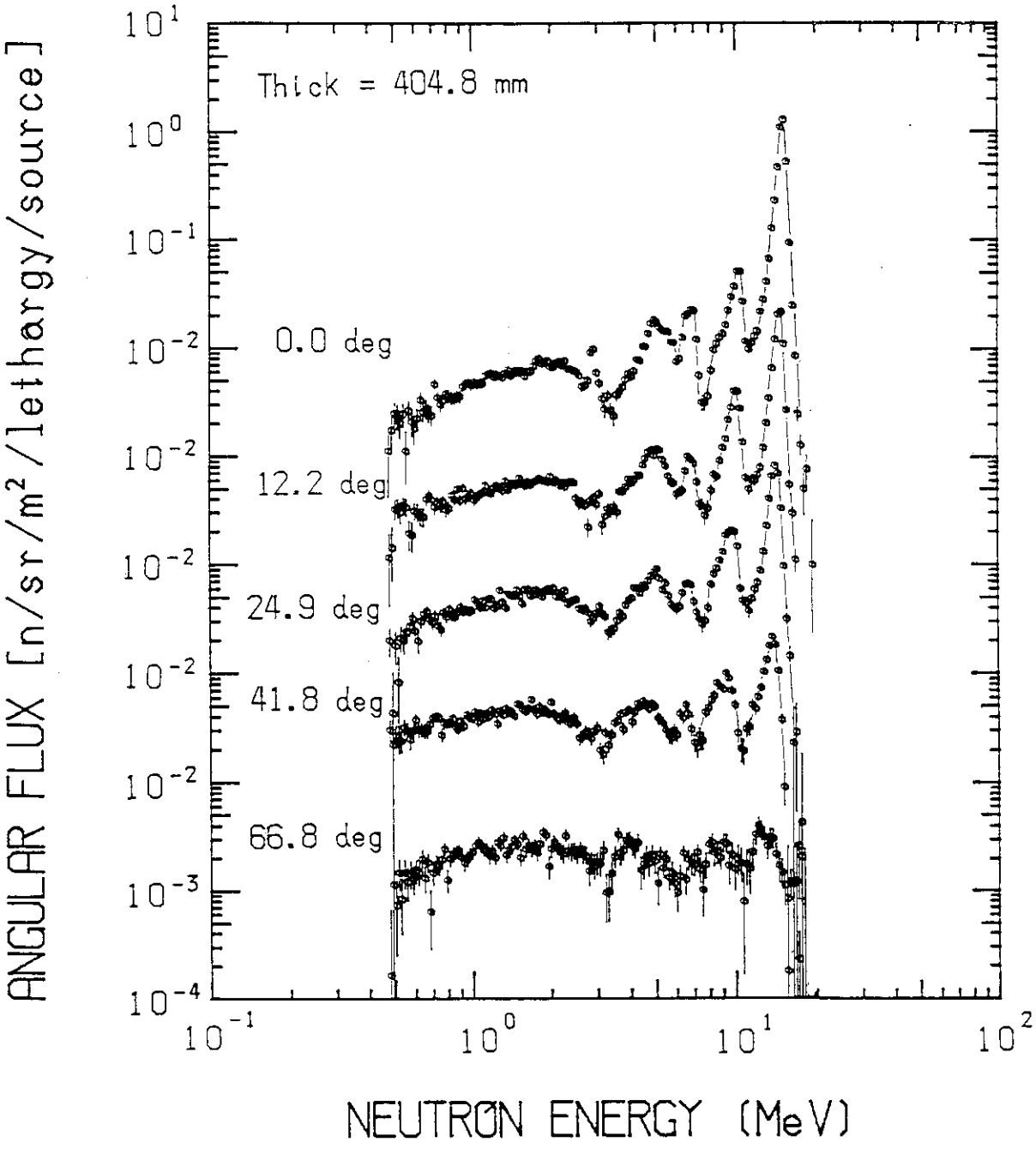

Fig. 4.1.4 Measured spectra of angular flux for the 404.8 mm-thick graphite slab. Error bars include only statistical error due to neutron counts.

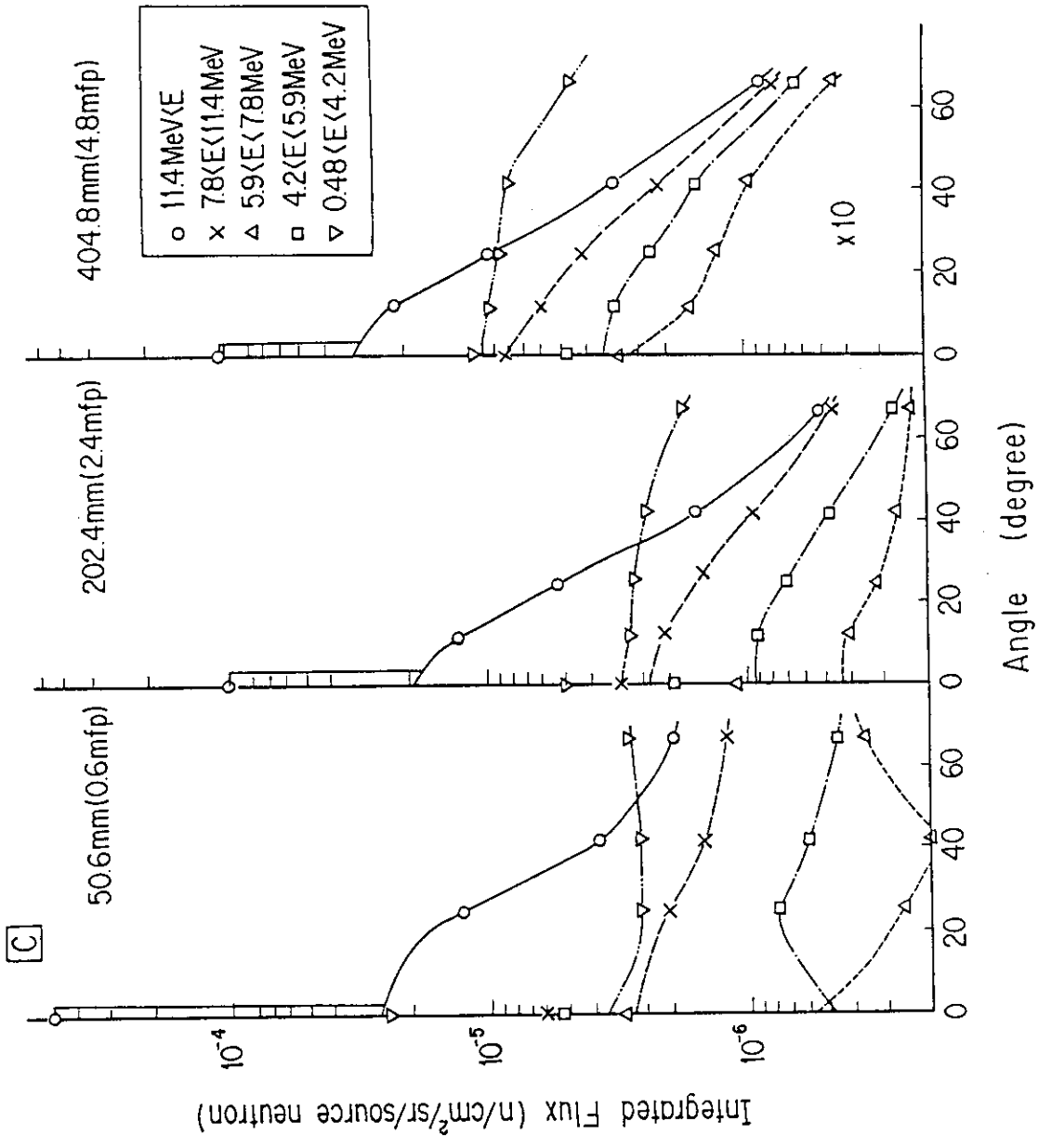

Fig. 4.1.5 Integration of the measured flux in various energy regions.

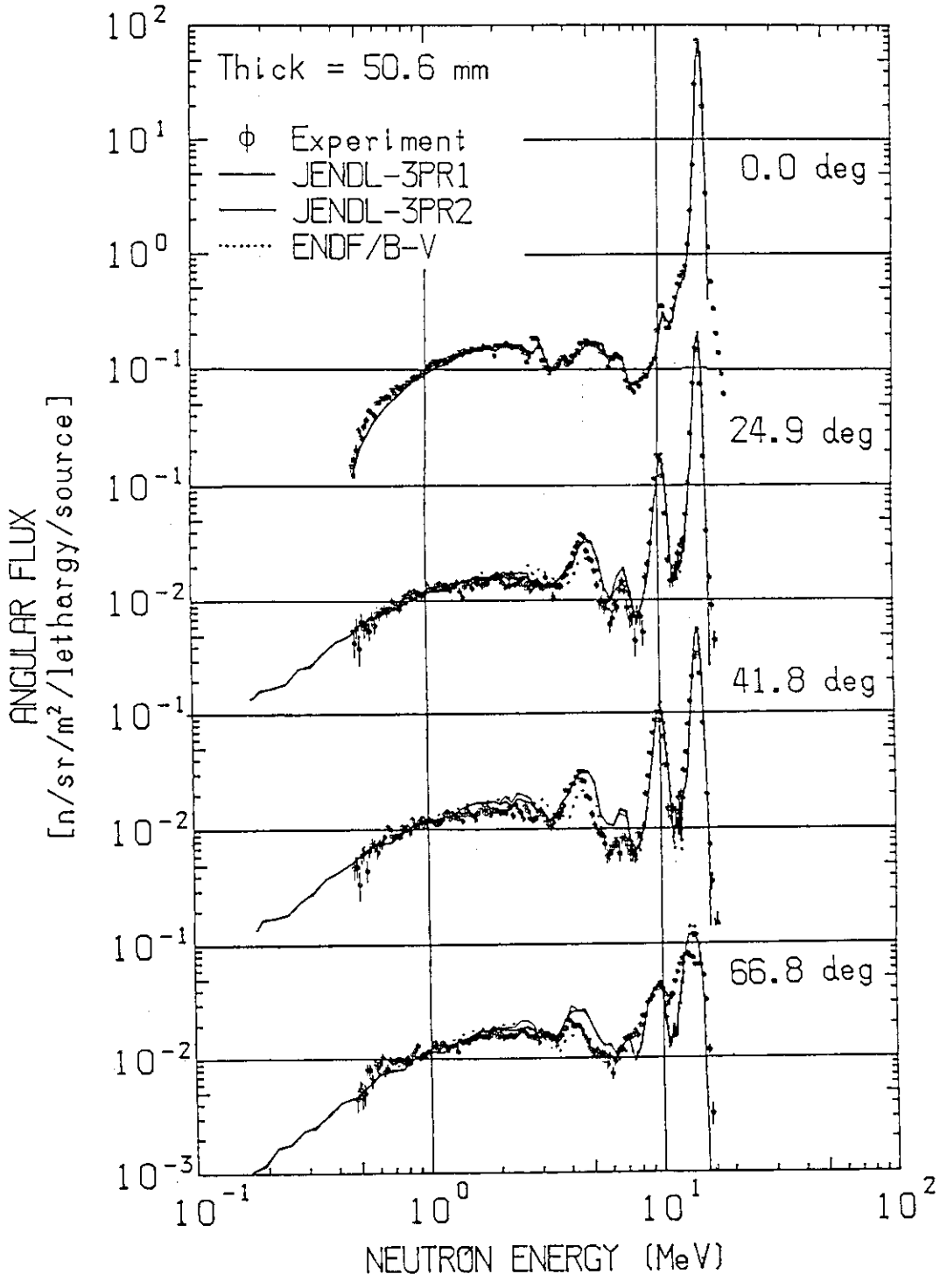

Fig. 4.1.6 Comparison of the experiment with the calculated spectra for the 50.6 mm-thick slab.

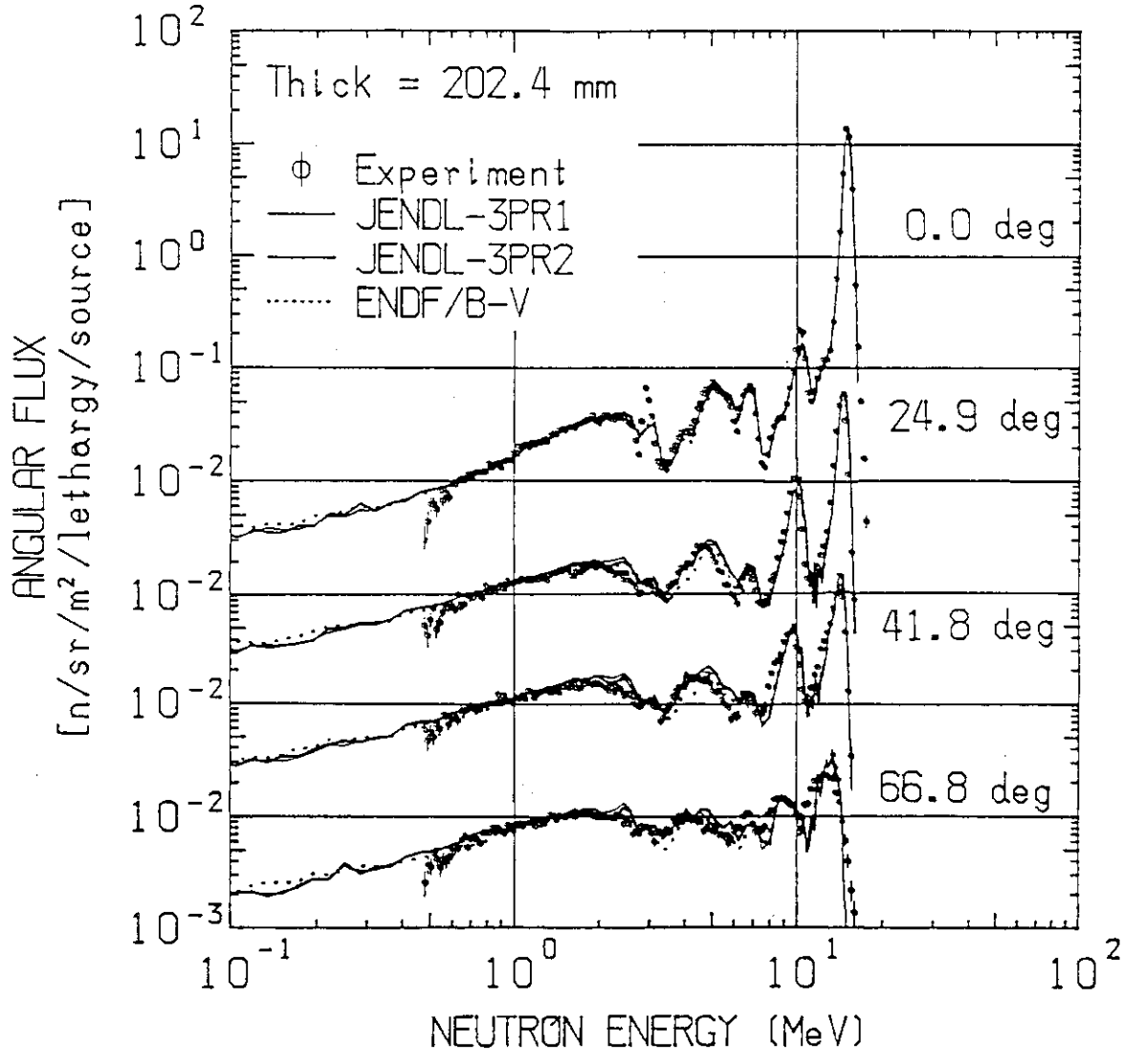

Fig. 4.1.7 Comparison of the experiment with the calculated spectra for the 202.4 mm-thick slab.

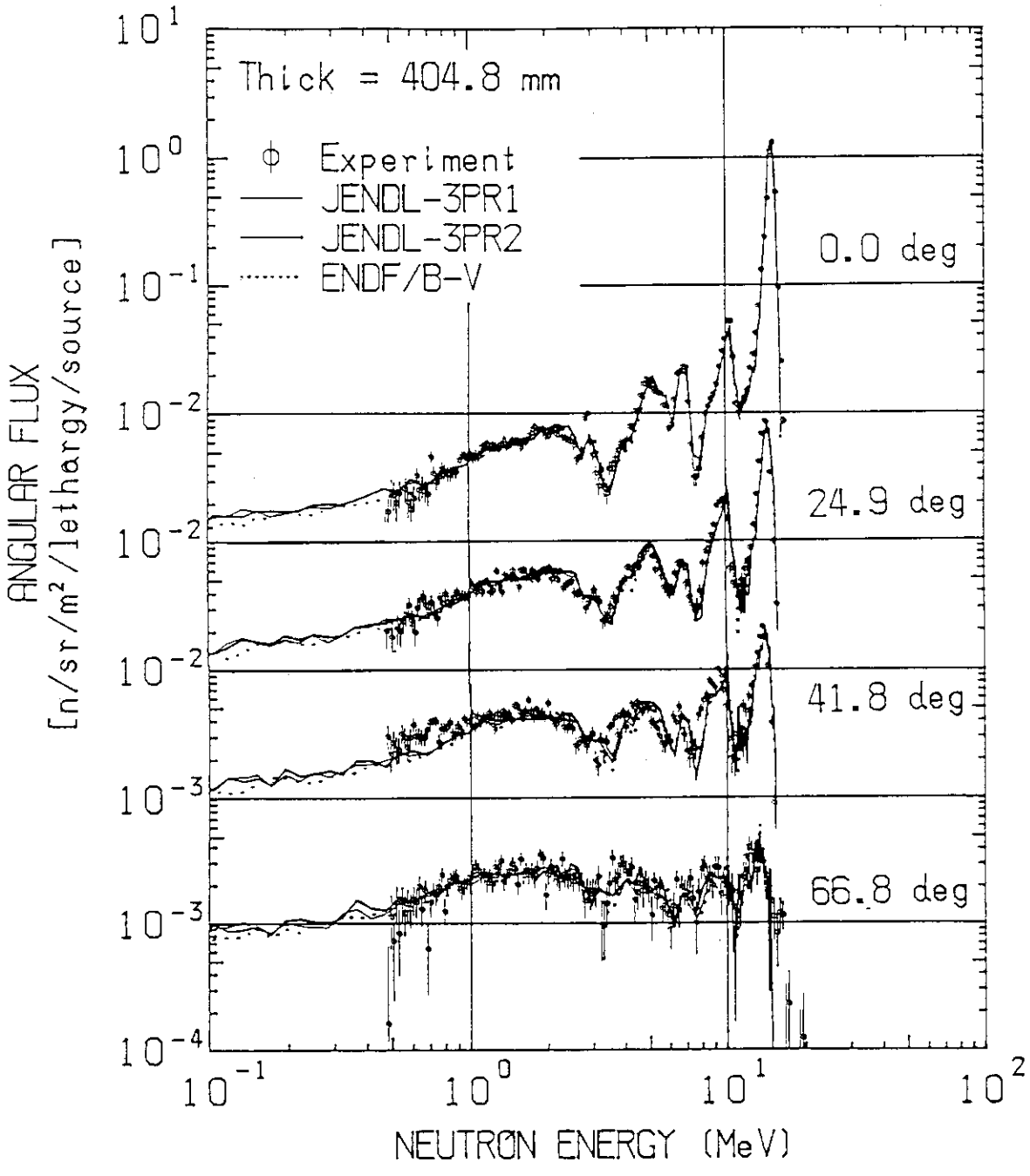

Fig. 4.1.8 Comparison of the experiment with the calculated spectra for the 404.8 mm-thick slab.

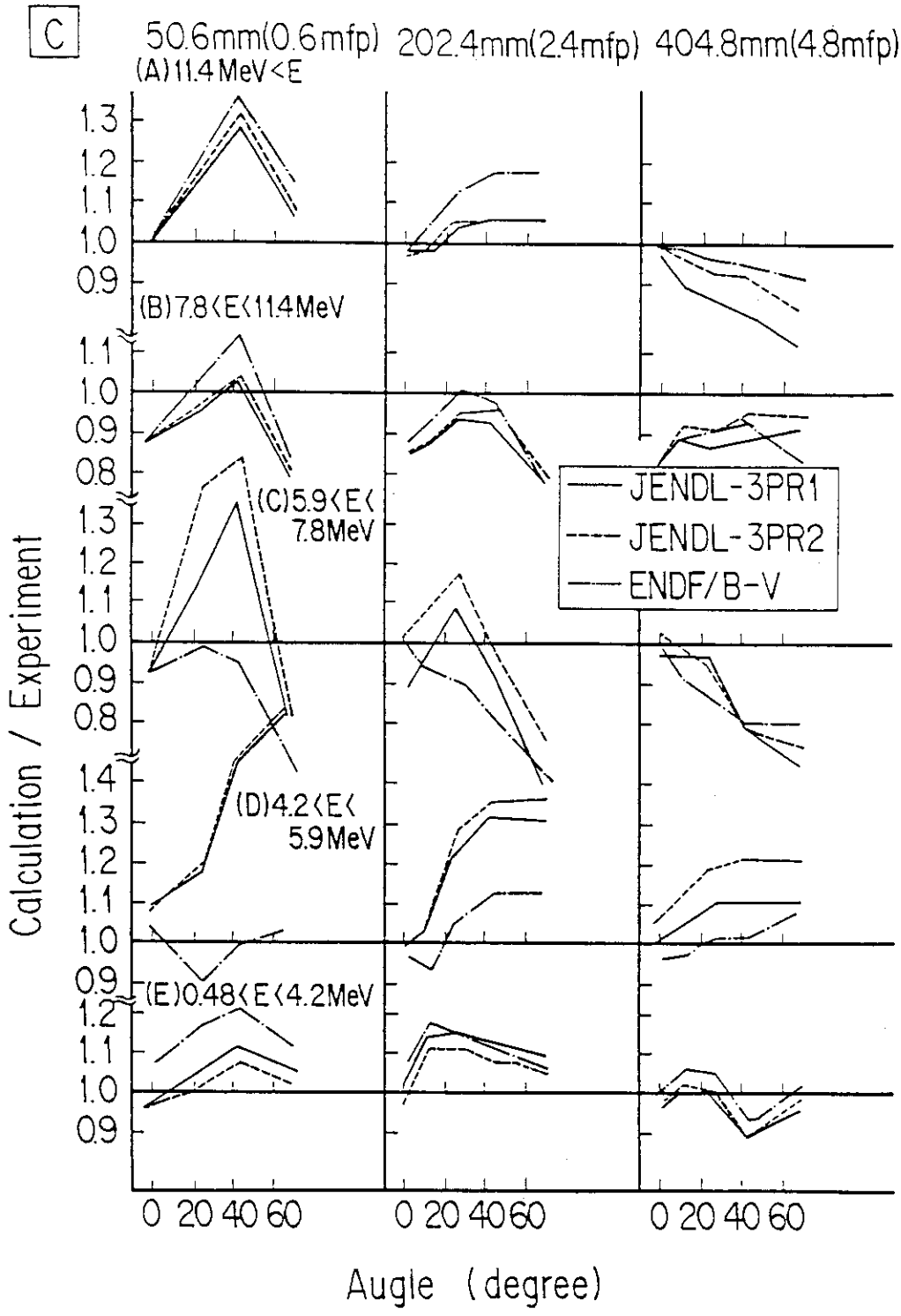

Fig. 4.1.9 Ratios of the calculated-to-measured values as functions of the thickness and the angle for various nuclear data files. Energy regions are (A) above 11.4 MeV, (B) 7.8 < E < 11.4 MeV, (C) 5.9 < E < 7.8 MeV, (D) 4.2 < E < 5.9 MeV and 0.48 < E < 4.2 MeV.

4.2 Beryllium Slabs

4.2.1 Introduction

Beryllium is an important material as a neutron multiplier in a fusion blanket design. There are many design studies [1]-[5] proposing beryllium neutron multiplier. In those designs, the accuracy of tritium breeding ratio estimation is required to be within 2 %.[6] This requires, in turn, small uncertainty of the nuclear data used in the designs. Youssef et al.[7] pointed out that for a $LiAlO_2$/Be water-cooled blanket, 82 % of the total uncertainty in the tritium production estimate from ^6Li is due to the (n,2n) reaction of beryllium. Furuta et al. [8] also showed that for a Li_2O/Be water-cooled blanket, the SAD (Secondary Angular Distribution) sensitivity of the beryllium elastic cross section is ten times as large as that for ^7Li. These studies suggest that the nuclear data of beryllium, especially secondary neutron emission spectra and angular distributions, contribute significantly to the uncertainty of reactor design calculations.

A number of cross section measurements [9]-[12] and integral experiments [13,14] have been made on beryllium. Recently, Li_2O/Be blanket experiments [15] were conducted at JAERI (Japan Atomic Energy Research Institute), based on JAERI/US-DOE collaborative program. The analysis of the experiment was performed with data which Shibata newly evaluated for beryllium for JENDL-3PR1[16] using some results of recent cross section measurements. However, there exists a discrepancy between the measured tritium production rates and those calculated with JENDL-3PR1 at the beryllium-Li_2O boundary. Thus supplementary information on beryllium is desired to interpret the experiment.

Measurements for beryllium slabs of 50.8 mm and 152.4 mm thick, which correspond to 0.9 and 2.7 mean free path for 15 Mev neutrons, respectively, were performed in the energy range from 15 Mev down to 50 keV. The experimental results were analyzed by the Monte Carlo calculation codes MORSE-DD[18] and MCNP[19] and the present nuclear data files JENDL-3PR1, ENDF/B-IV[20] and LANL[21] were tested.

4.2.2 Measurement

The experimental assembly was made up in pseudo-cylindrical slab shape by stacking rectangular beryllium blocks with 50.8 mm square base and the 50.8 mm or 101.6 mm heights. The beryllium blocks were supplied by Argonne National Laboratory. The assembly was supported by thin-walled aluminum square tubes in the same manner as the graphite experiment. The average density of beryllium blocks used was 1.837 Mg/m^3; Be purity was 98.92 wt % and the contaminant was principally BeO. The thicknesses of the assemblies measured were 50.8 mm and 152.4 mm, corresponding to 0.9 and 2.7 mean free paths. In both cases, the area equivalent radius was 315 mm.

Time-of-flight spectra were measured using the 1/16 ^{241}Am bias and ^{133} Ba bias to obtain the energy spectrum down to below 100 keV, so that the repetition period of the pulsed deuteron beam was set to 4 μs. Then the time spectra to 4 μs were obtained through low bias spectrum acquisition, while the time spectra to 1.5 μs were obtained through high bias acquisition. Figure 4.2.1 shows the typical time spectra obtained by the present time-of-flight measuring system for the beryllium slab assembly.

4.2.3 Results

The energy spectra of angular neutron fluxes obtained here are shown in Figs. 4.2.2 and 4.2.3 for two thicknesses. The results in the figures are presented only with statistical errors. For the 50.8 mm-thick assembly, the measurement at the angle of 12.2 degree was not performed because the target was included in the effective measured area. The energy spread of the elastic peak at 0 degree for the 50.8 mm-thick assembly was about 8 %.

A peak due to parasitic $^{2}D(d,n)^{3}He$ reaction neutrons was seen at ∿3 MeV in the 0-degree case only of the 50.8 mm-thick assembly. Three peaks due to scattering are recognized in the obtained spectra: They correspond to elastically scattered neutrons, and inelastically scattered neutrons at the 2.43 MeV cluster level and the 6.76 MeV level. Two apparent dips also can be seen. They are caused by the neutrons removed by elastic scattering at the resonance of ∿2.8 MeV and ∿620 keV.

Figures 4.2.4 presents angular dependences of the measured flux. The energy spectra integrated over the following energy ranges were grouped depending on the reaction types that contributes to each energy range:

(A) E_n > 10 MeV: The group is composed of neutrons scattered by elastic and 2.43 MeV cluster level reactions.

(B) 2 < E_n < 10 MeV: The group is composed of neutrons scattered by high inelastic level reactions.

(C) 0.5 < E_n < 2 MeV: The group is composed of neutrons scattered by continuum level reaction and second step emission neutrons of (n,2n) reaction.

(D) 0.1 < E_n < 0.5 MeV: The group is mainly composed of multiply scattered neutrons.

The 0-degree fluxes have different characteristics from the other angles, since they include the uncollided flux. In the figures, the values exclusive of the uncollided flux are shown as black symbols, as obtained from the Monte Carlo calculation described.

The figures show that the integrated flux in the region (A), corresponding to elastically scattered neutrons, is large in the forward direction, and that anisotropy of these neutrons is enhanced in the 152.4 mm-thick(2.7 mfp) assembly. The integrated fluxes in the other groups have isotropic dependence, though those of the 2.7 mfp case are apt to decrease with the angle. The values of the integrated fluxes for the 2.7 mfp case for groups other than (A) are of the same order as those for the 0.9 mfp case, regardless of the assembly thickness. These facts can be explained from the multiple-scattering effect; elastically scattered neutrons decrease with the measuring angle, since multiple scattering increases with that angle, i.e., as the penetration length increases, while the fluxes in the lower energy range are compensated by neutrons slowing down from the region (A).

4.2.4 Discussions

Comparison with calculations

One of the calculational analyses was carried out by using the Monte Carlo code MORSE-DD[18] which was modified from the MORSE-CG[27] code. The MORSE-DD code uses a double-differential form cross section

library of 125 groups for the group-to-group scattering matrix so as to accurately express the angular distribution and energy-angle correlation from an original file. The nuclear data library used was DDXLIB1[18] whose beryllium cross section was taken from evaluated nuclear data files JENDL-3PR1[16] and ENDF/B-IV[20] by using the PROF-DD[28] processing code.

Calculations were also done by using the MCNP[19] code with the BMCCS2 library that includes Be reaction cross sections evaluated by Young and Stewart[21] at Los Alamos National Laboratory. The fluxes of both calculations were accumulated to achieve good statistics, less than 5 % fsd (fraction of standard deviation).

The source neutron spectrum emitted from the target was reproduced with a 90 group structure above 0.05 MeV from the measured one. An isotropic distribution was assumed for source neutrons, based on the measured angular dependence of the emission rate. The source intensity was normalized to the integration of the forward spectrum over a 4π solid angle, i.e., 1.086.

Results calculated with three nuclear data files and two Monte Carlo codes were compared to the measurements. Typical results of calculations are compared with the experimental results in Figs. 4.2.5-4.2.6. The results with three nuclear data files at 0 degrees show fairly good agreement as a whole. The ENDF/B-IV is, however, slightly lower in the energy range between 0.2 and 2 MeV. In contrast to the forward direction, there exist large differences among three results at 24.9 degrees. Here the JENDL-3PR1 underpredicts the flux from 2 to 10 MeV and below 0.5 MeV. The ENDF/B-IV also underestimates the flux from 0.1 to 2 MeV. On the other hand, the LANL overestimates the flux around 1 MeV and 6 MeV. Moreover, all three results for the elastic peak present lower values than those of the experiment. As for the 66.8 degree case in Fig.4.2.6, agreement is better than for the 24.9 degree case, but still there are some differences. The JENDL-3PR1 and LANL underestimate the flux below 0.5 MeV and the ENDF/B-IV does so from 0.3 to 1 MeV. The elastic peak obtained from each file is also lower than the experimental one.

The results at 0 degrees for the 152.4 mm-thick (2.7 mfp) slab show larger differences among the files than the 50.8 mm (0.9 mfp) case as seen in Fig. 4.2.6. Especially below 2 MeV, the JENDL-3PR1

and the ENDF/B-IV predict the flux lower than the experiment; this tendency differs from the 0.9 mfp case. At the other angles, the results of all three data files show the same trends as the 0 degree case. The elastic peaks predicted by all three files are lower than the experiment at all angles except 0 degrees.

Ratio of the calculations to the experiment

The calculated-to-measured value ratios (C/E) for the three nuclear data files are shown in Figs. 4.2.7 for various energy groups described in Sec. 4.2.3. They correspond to 50.8 (0.9 mfp) and 152.4 mm-thick (2.7 mfp) slab, respectively. In the 0.9 mfp case, these C/E comparisons show directly the validity of nuclear data of Be at 14.8 MeV in the files. The C/E trends are almost independent of angle in the comparisons except for the elastic reaction group. The high energy neutrons in the region (A) shows the same trend for all files where the discrepancy of nuclear data increases with angle. This suggests that: (1) The data of the angular dependence for 14.8 MeV elastic cross section or for the total scattering cross section below 14.8 MeV are not adequate; (2) Since the integrated fluxes below 10 MeV are almost independent of angle (See Fig. 4.2.4), these C/E discrepancies are caused by the inadequate inelastic total cross sections in the evaluated files. The comparison of the double differential cross sections[16] in Fig. 4.2.8 is consistent with the present C/E comparisons, namely, the underestimations of the fluxes with the JENDL-3PR1 in the region (B) and with the ENDF/B-IV in the region (C) can be attributed to the small values of the 6.76 MeV level cross section, and of the higher continuum level cross sections as pointed out by Houge[10], respectively. The LANL, which includes many pseudo-levels in the inelastic cross section[21], always overpredicts the flux as shown in the regions (B) and (C), i.e., the values of those levels are rather large. In the region (D), while the LANL shows agreement within 10 %, the JENDL-3PR1 and the ENDF/B-IV are too small due to the unbalance of level configuration mentioned above.

The result of thickness increase are distorted by multiplly scattered neutrons in the same way as discussed in the graphite slab experiment. Down-scattering propagates the higher energy discrepancy to the lower energy range with elastic and inelastic cross sections.

Therefore, the C/E trends are similar to the 0.9 mfp slab case for the higher energy range in the region (A) and (B). On the other hand, the trends of C/E for the lower energy ranges of (C) and (D) in Figs. 4.2.7 combine neutrons down-scattered by inelastic reactions from the energy range above threshold energy and primary reaction neutrons in the lower energy range itself. Thus the changes of trends from the 0.9 mfp to 2.7 mfp results in the region (C) for the JENDL-3PR1 and in the region (D) for the LANL seem to be consistent.

The C/E discrepancies are of the same order for both slabs, hence, the flux spectrum shape can be interpreted by the above considerations. Most of the reasons for the discrepancy in the 2.7 mfp slab can be attributed to the primary reactions of 14.8 MeV incident neutrons. From the viewpoint of an integral experiment on beryllium, the discrepancies due to the primary reaction by 14.8 MeV neutrons are too large to discuss the problems for the thicker slab. The result of the 2.7 mfp slab could provide benchmark test for the reaction in the 1-10 MeV range, when the nuclear data for 14.8 MeV neutrons are accurate enough to interpret satisfactorily the flux spectra for the 0.9 mfp slab.

4.2.5 Conclusion

We have measured the angular neutron flux from 50.8 mm- and 152.4 mm-thick beryllium slab assemblies. The measured spectra were obtained in the energy range below 100 keV with an error less than $\sim$ 5%; the measuring angle was varied between 0 and 66.8 degrees. Experimental results show an isotropic dependence for the neutron emission spectra except for elastic scattered neutrons.

The experiment was also analyzed by using Monte Carlo codes with three kinds of nuclear data files. It can be concluded from the comparisons between the measurements and the calculations that:

1. The C/E trends of the three nuclear data files, i.e., JENDL-3PR1, ENDF/B-IV, and LANL differ among themselves, except those corresponding to the elastic peak.
2. Discrepancies of the three files from the experiment range about 20-30 %, as a whole.
3. The discrepancies noted for the high-energy region can be attributed to the angular dependence of the elastic reaction for 14.8 MeV.

4. The representation of the inelastic total cross sections for 14.8 MeV neutrons in JENDL-3PR1 and ENDF/B-IV , such as 6.76 MeV and higher levels, are not accurate enough to reproduce the leakage spectrum.

Consequently, the above inadequacy of the beryllium cross section affects the estimation of high threshold reactions, e.g., tritium production by ^{7}Li, activation of structural materials ... etc., in a fusion blanket design. The representation of the inelastic and (n,2n) reactions should be re-evaluated.

References

1) Abdou M. A., Wittenberg L. J. and Maynard C. W.: Nucl. Technol., 26, 400 (1975).
2) Cheng E. T. and Conn R. W.: Nucl. Sci. Eng., 62, 601 (1977).
3) Wong C. P. C., Bourque R. F., Cheng E. T., Creedon R. L., Maya I., Ryder R. H., and Schultz K. R.: Fusion Technol., 8, 114 (1985).
4) Maki K.: Fusion Technol., 8, 2655 (1985).
5) Moir P. W., Lee J. D., Maninger R. C., Neef W. S. Jr., and Sherwood A. E.: Fusion Technol., 8, 133 (1985).
6) Abdou M. A.: "Tritium Breeding in Fusion Reactors," ANL/FPP/TM-165, Argonne National Laboratory, (1982).
7) Youssef M. Z. and Abdou M. A.: Fusion Technol., 9, 286 (1986).
8) Furuta K., Oka Y and Kondo S.: Nucl. Eng. Design/Fusion, 3, 287 (1986).
9) Drake C. M., Auchampauch G. F., Arthur E. D., Ragan C. E., and Young P. G.: Nucl. Sci. Eng., 63, 401 (1977).
10) Houge H. H., Bonbehren P. L., Epperson D. H., Glendinning S. G., Lisowski P. W., Nelson C. E., Newson H. W., Purser F. O., Tornow W., Gouid C. R., and Seagondollar W.: Nucl. Sci. Eng., 68, 38 (1978).
11) Baba M., Sakase T., Nishitani T., Yamada T., and Momota T.: "The Interaction of Fast Neutrons with ^{9}Be," Proc. Conf. Nuclear Physics/Reactor Data, Harwell, United Kingdom Atomic Energy Authority, p.198 (1978).
12) Takahashi A., Yamamoto J., Murakami T., Oshima K., Oda H., Fujimoto F., and Sumita K.: "Measurement of Double Differential

Neutron Emission Cross Sections with 14 MeV Source for D. Li, Be, C, O, Al, Cr, Fe, Ni, Mo, Cu, Nb, and Pb," Proc. Int. Conf. Nuclear Data for Science and Technology, Antwerp, Belguim, September 6-10, 1982, CONF-820906, p.360, D. Riedel Publishing Company (1982).

13) Wong C., Anderson J. D., Brown P., Hansen L. F., Kammerdiener J. L. , Logan C., and Pohl B.: "Livermore Pulsed Sphere Program: Program Summary Through July 1971," UCRL-51144, Lawrence Livermore National Laboratory (1971).

14) Basu T. K., Nargundkar V. R., Cloth P., Filges D., and Tacznowski S.: Nucl. Sci. Eng., 70, 309 (1979).

15) Nakamura T. and Abdou M. A.: "Summary of Recent Results for JAERI/US Neutronics Phase I Experiment," Proc. 7th Topical Meeting on the Technology of Fusion Energy, Reno, Nevada, June 15-19, 1986, Fusion Technol., 10, 541 (1986); and Trans. Am. Nucl. Soc., 52, 106 (1986).

16) Shibata K.: "Evaluation of Neutron Nuclear Data of ^{9}Be for JENDL-3," JAERI-M 84-226, Japan Atomic Energy Research Institute (1984).

17) Oyama Y. and Maekawa H.: "Measurement of Angle-Dependent Neutron Spectra from Lithium-Oxide Slab Assemblies by Time-of-Flight Method," JAERI-M 83-195, Japan Atomic Energy Research Institute (1983).

18) Nakagawa M. and Mori T.: "MORSE-DD, A Monte Carlo Code Using Multi-Group Double Differential Form Cross Section," JAERI-M 84-126, Japan Atomic Energy Research Institute (1984).

19) Los Alamos Radiation Transport Group (X-6): "MCNP-A General Monte Carlo Code for Neutron and Photon Transport," LA-7396-M, Los Alamos National Laboratory Revised (April 1981).

20) ENDF/B Summary Documentation, BNL-NCS-17541 (ENDF-201),2nd Edition, compiled by D. Garber (1975).

21) Young P. G. and Stewart L.: "Evaluated Data for n+^{9}Be Reactions," LA-7932-MS, Los Alamos National Laboratory (1979).

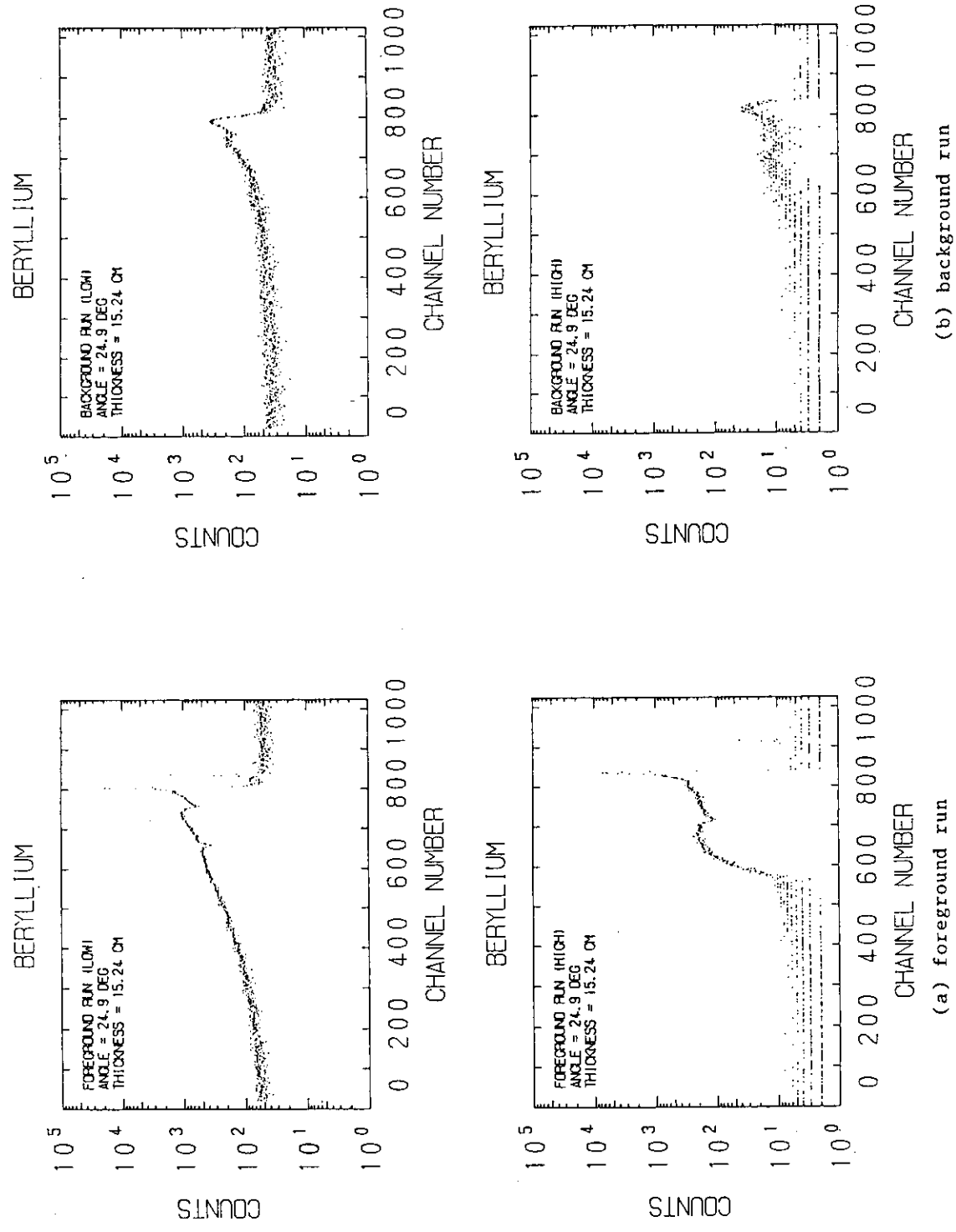

(a) foreground run (b) background run

Fig. 4.2.1 Typical time spectra observed on the beryllium slab

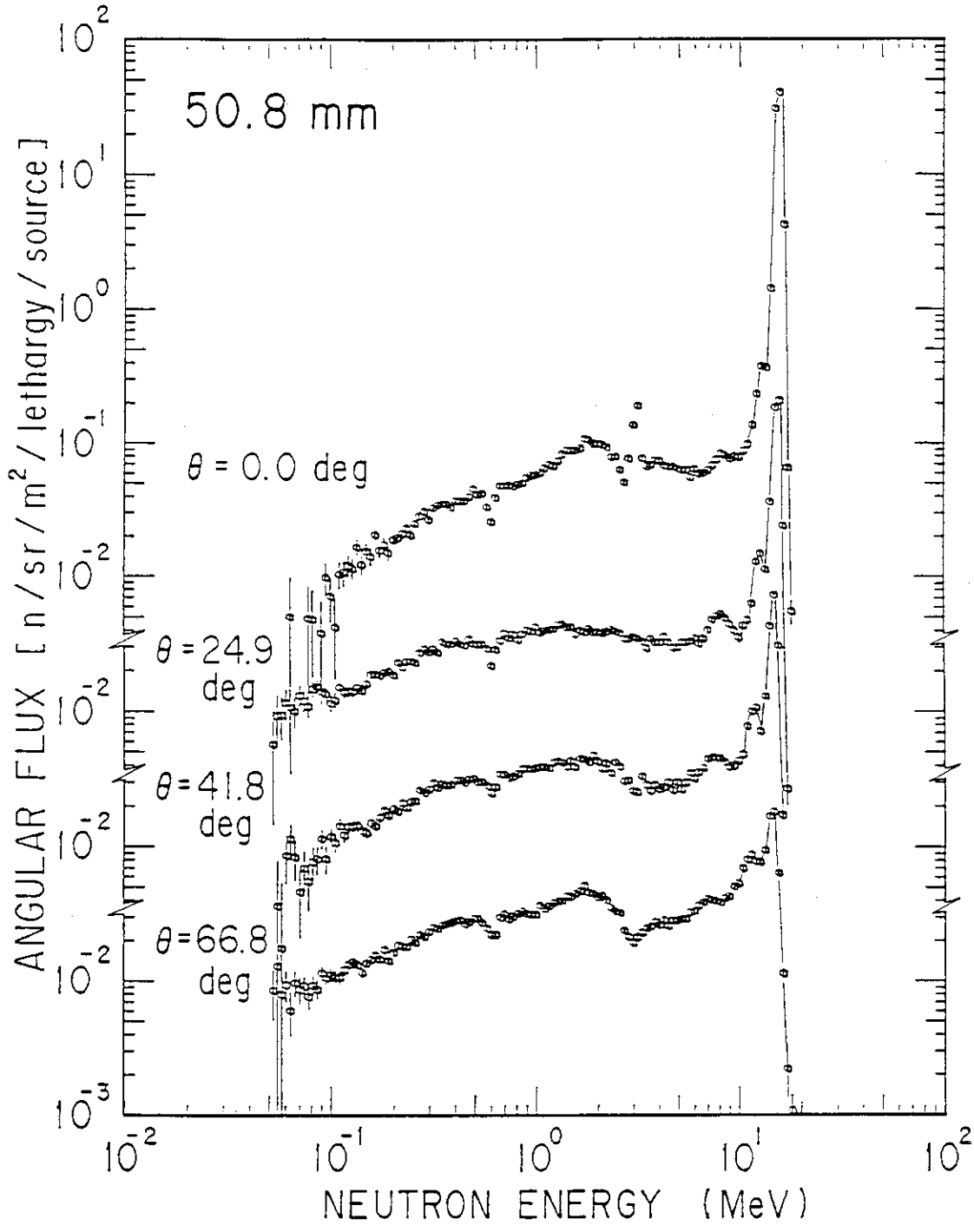

Fig. 4.2.2 Measured spectra of angular flux for the 50.8 mm-thick beryllium assembly. Error bar includes only statistical error due to neutron counts.

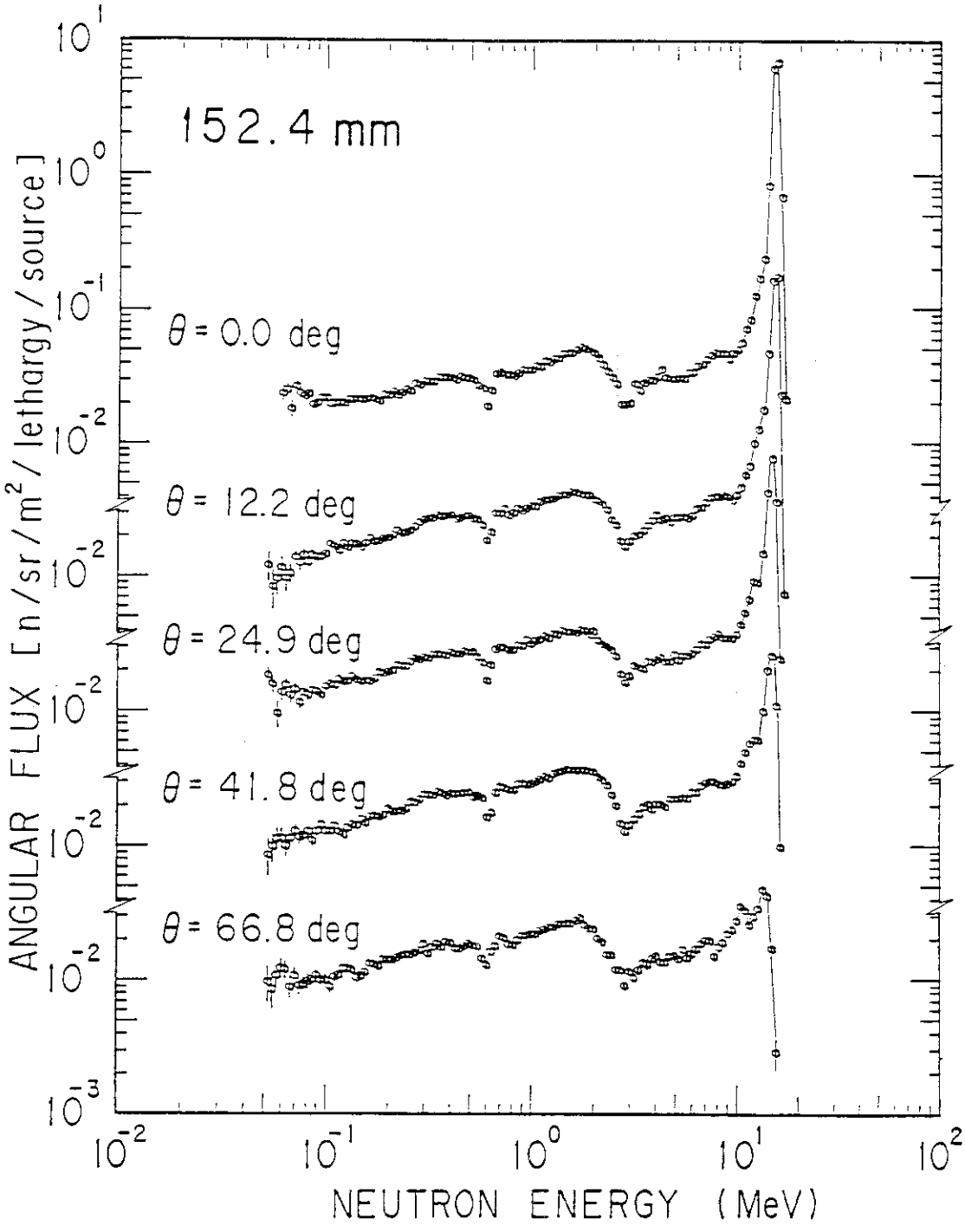

Fig. 4.2.3 Measured spectra of angular flux for the 152.4 mm-thick beryllim assembly. Error bars includes only statistical error due to neutron counts.

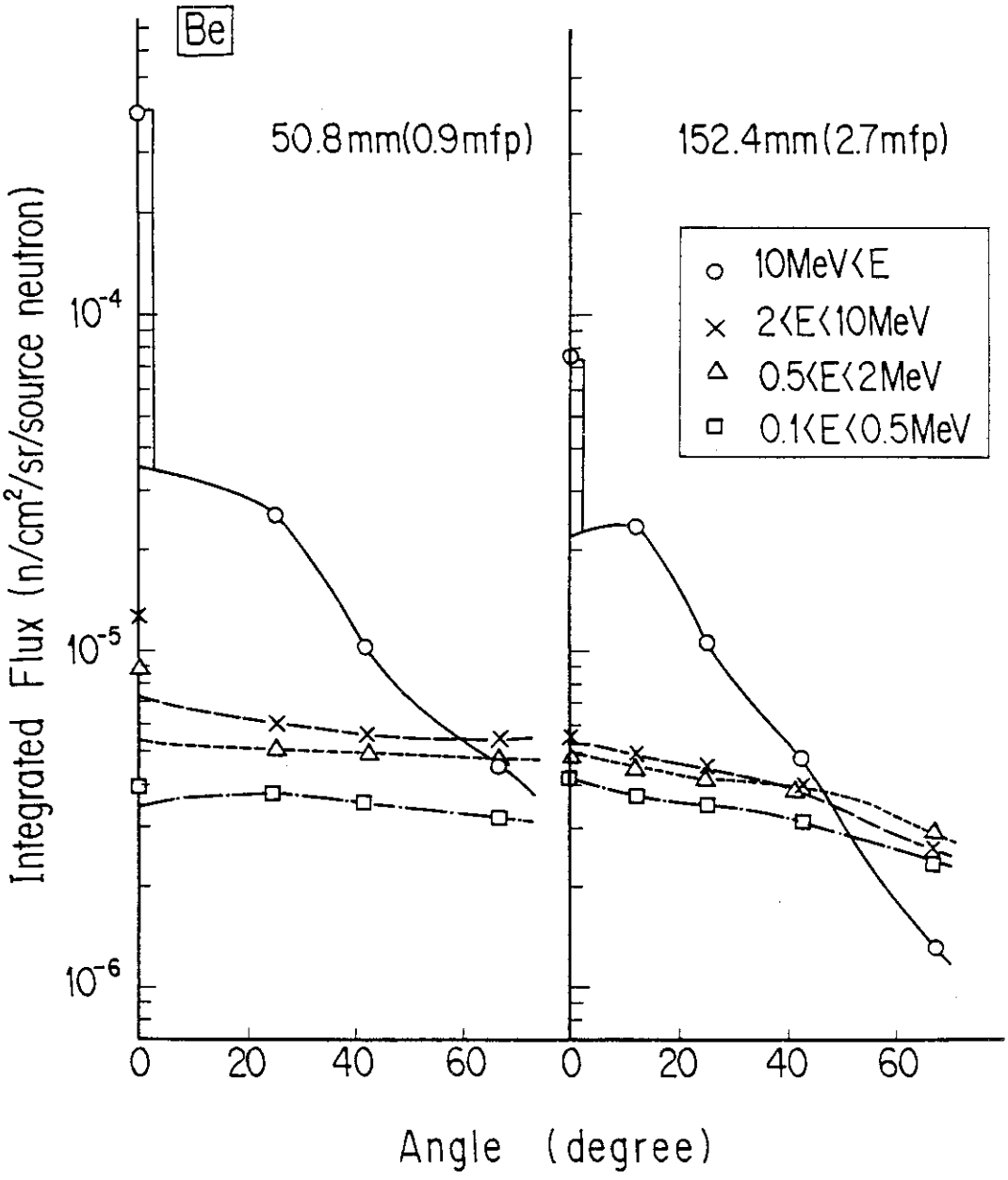

Fig. 4.2.4 Measured flux integrated over four energy ranges vs. measuring angle. Black symbols show the collided flux: The uncollided flux calculated by the MCNP code is subtracted from the measured value. Lines are only for eye-guide.

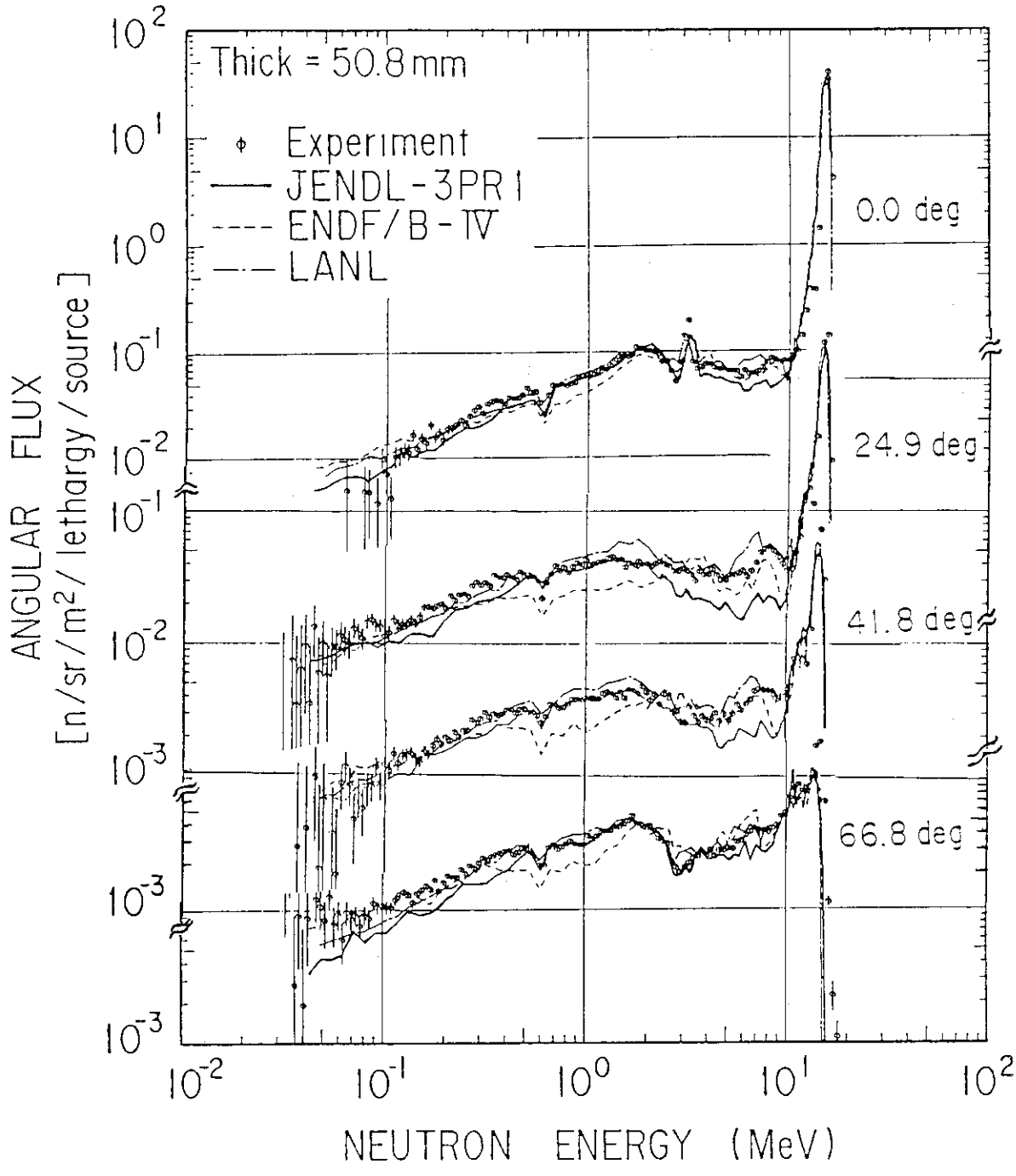

Fig. 4.2.5 The comparison between the measured and the calculated results for the angular flux of the 50.8 mm-thick assembly.

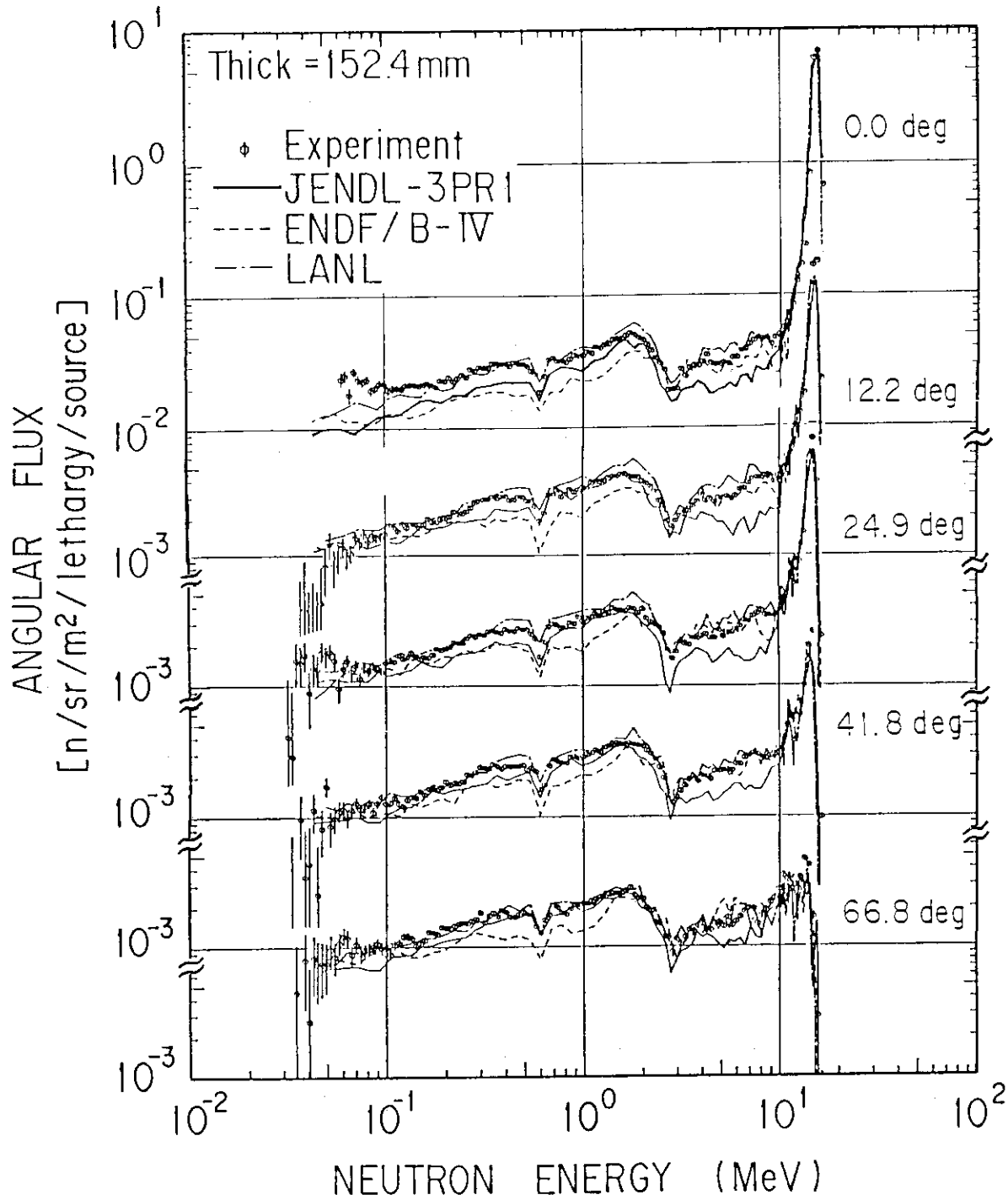

Fig. 4.2.6 The comparison between the measured and the calculated results for the angular flux of the 152.4 mm-thick assembly.

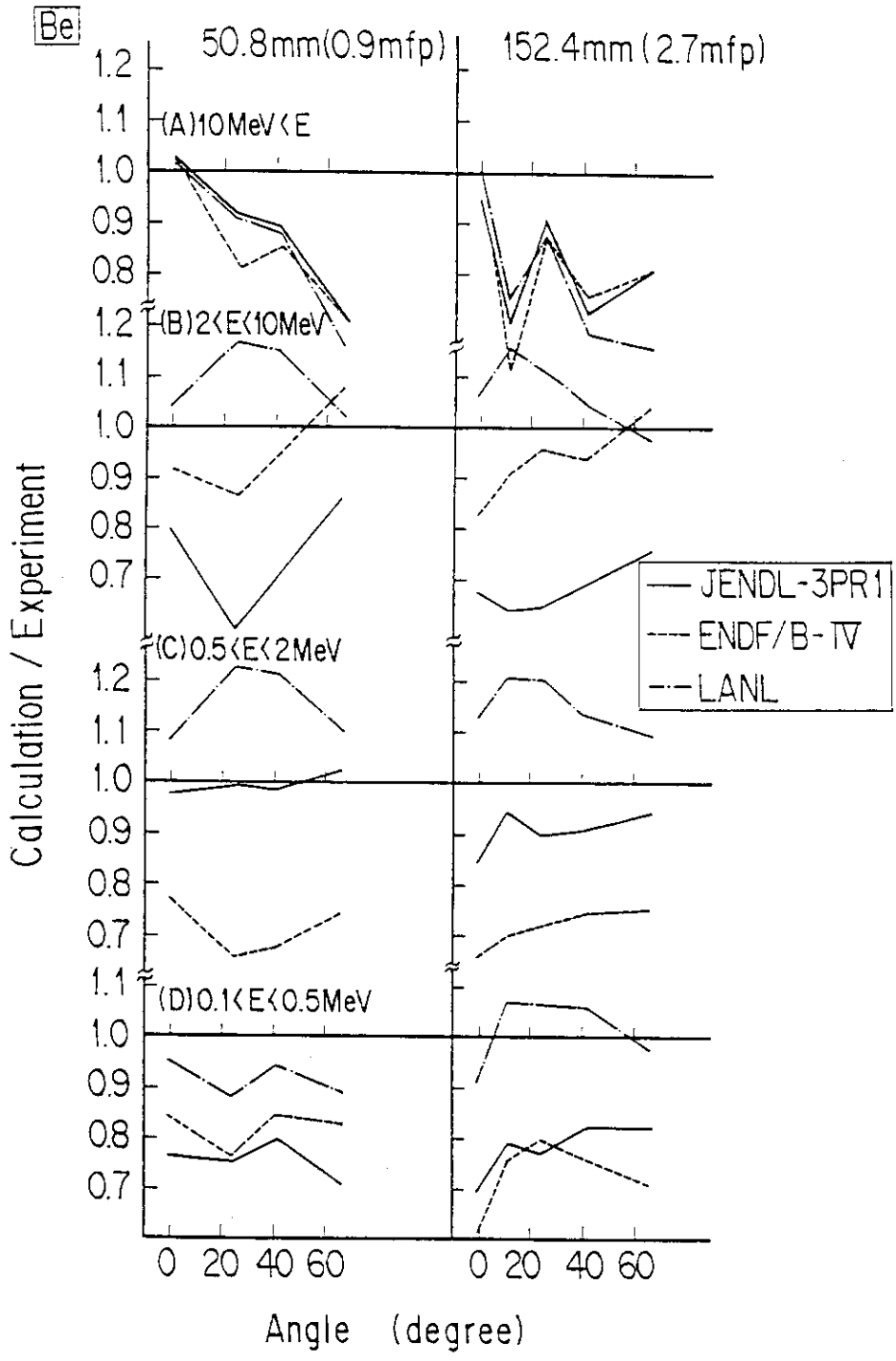

Fig. 4.2.7 Ratios of the calculated-to-measured values as functions of the thickness and the angle for various nuclear data files. Energy regions are (A) above 10 MeV, (B) 2< E < 10 MeV, (C) 0.5 < E < 2 MeV and (D) 0.1 < E < 0.5 MeV.

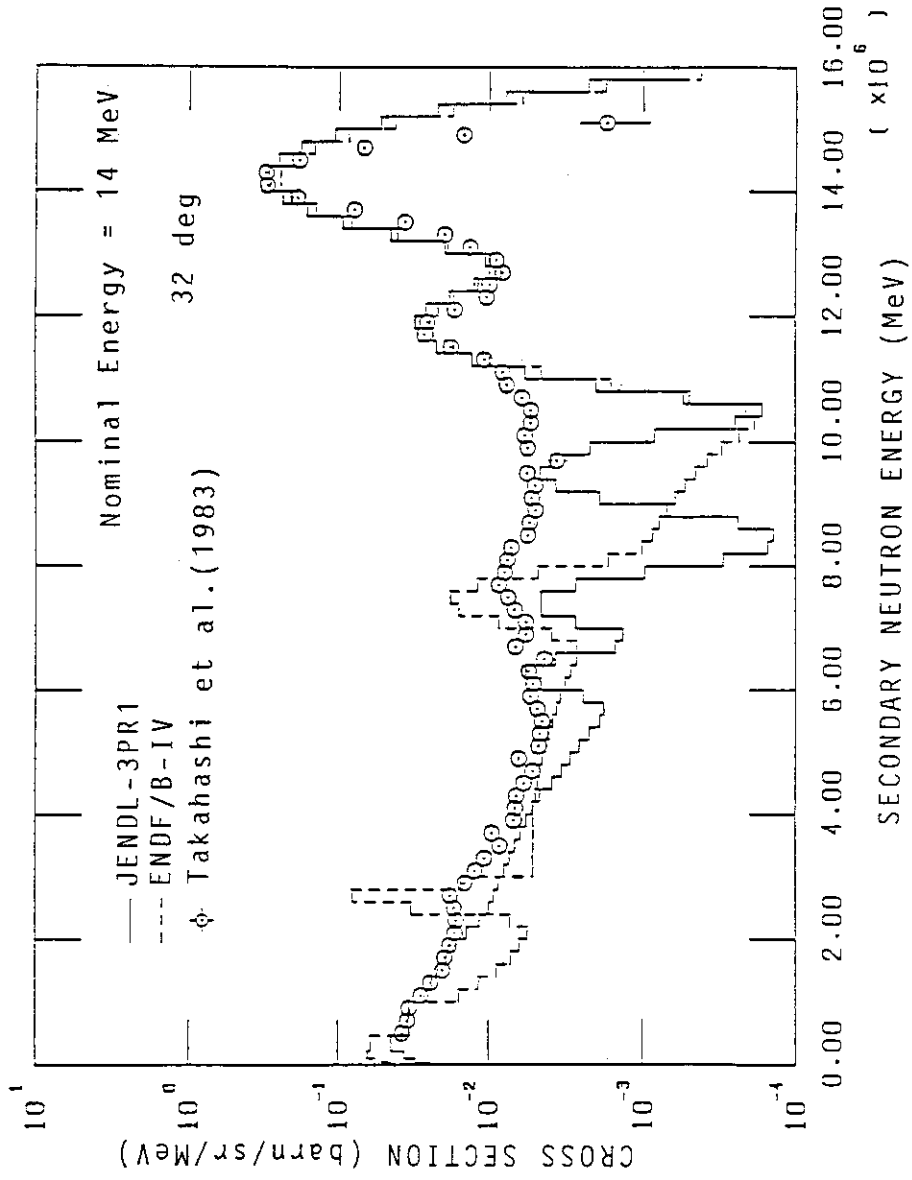

Fig. 4.2.8 Comparison of double-differential cross section for nominal 14 MeV neutrons.[16]

4.3 Lithium-Oxide Slab

4.3.1 Introduction

In nuclear designs of D-T fusion reactor blankets, the tritium breeding ratio and nuclear heating rate should be accurately predicted[1] since they have strong influence on the feasibility of the overall design. Tritium is produced by the $^{7}Li(n,n'\alpha)T$ and $^{6}Li(n,\alpha)T$ reactions, which also dominate nuclear heating by energy deposition in the blanket. Therefore, materials containing lithium, e.g, lithium-oxide (Li_2O) or lithium-aluminate (Li_2AlO_3) have been proposed for breeding blanket fabrication.

Recently several cross section measurements[2]-[5] have been performed on lithium for high energy neutrons (around 14 MeV). Based on those recent measurements, the nuclear data on ^{7}Li and ^{6}Li also have been newly evaluated, for purpose of fusion reactor design, in a new compilation of JENDL-3[6]-[8]. Hence, it is very useful to provide integral experiments which can assess cross section information for neutrons produced by a D-T fusion reaction.

In the present study, angular fluxes on the surface of lithium-oxide slabs were measured as functions of thickness and angle. Lithium-oxide is the most promising material in the conceptual design of the reactor proposed by JAERI (Japan Atomic Energy Research Institute).[9] The measurement was initially performed in 1983.[10] That result showed large discrepancies with increasing angle and thickness because the shielding was not sufficient to obtain a good signal-to-background ratio. Hence, a new measurement has been carried out with some improvement of shielding and extension of the measuring energy range.

The experimental results were analyzed by the MCNP code and compared with the calculated results using the nuclear data of JENDL-3PR1 and -3PR2.

4.3.2 Measurement

The experimental assembly was constructed of lithium oxide (Li_2O) blocks in a pseudo-cylinder with an area-equivalent diameter of 628 mm and the thicknesses of 48, 200, and 400 mm, corresponding to 0.6, 2.5

and 5.0 mean free paths for 14.8 MeV neutrons, respectively. The Li_2O blocks were supported by thin-walled, square aluminum tubes in the manner described previously.

The Li_2O blocks used in the experiment were rectangular prisms made in two sizes with a base 50.6 mm x 50.6 mm and heights of 50.6 mm and 203 mm (Fig.4.3.1). They were manufactured by putting one, two and four bricks in a 0.2 mm-thick stainless steel box and then sealed by electron beam welding to protect them from the humidity. The Li_2O bricks were made from Li_2O powder by cold-pressing to a size of 49 mm x 49 mm x 50 mm. The density of Li_2O bricks was 75.5% of the theoretical density of 2.02 Mg/m^3. Results of a chemical analysis of the bricks are summarized in Table 4.3.1.

Since the blocks have a small void where the steel cladding is welded, as shown in Fig. 4.3.2, the assemblies were arranged so as to keep voids outside the assembly by the block configuration shown in Fig. 4.3.3. The homogenized nuclide densities of this assembly configuration are given in Table 4.3.2., obtained by averaging the densities of the Li_2O bricks and the stainless steel wall.

4.3.3 Results

Time-of-flight spectra were measured using the 1/16 ^{241}Am bias and the ^{133}Ba bias to extend the energy spectrum down to below 100 keV, and thus include the 250 keV elastic resonance of ^{7}Li. The repetition period of the pulsed deuteron beam was set to 4μ; the time spectra to 4 μs and 1.5 μs were obtained from the low and high biases, respectively. Figure 4.3.4 shows typical time spectra obtained for the lithium-oxide slab assembly by the present system. Measuring angles were 0, 12.2, 24.9, 41.8 and 66.8 degrees.

Angular neutron flux spectra are shown in Figs. 4.3.5 - 4.3.7 for three thicknesses of the slab. The results in the figures are presented only with statistical errors. For the 48.0 mm-thick (0.6 mfp) assembly, the measurement at the angle of 12.2 degree was not performed because the target was included in the effective measured area. The spectra below 100 keV for the 0.6 mfp-thick assembly may be slightly suspect due to the poor signal-to-background ratio.

A peak due to parasitic $^{2}D(d,n)^{3}He$ reaction neutrons was seen at about 3 MeV, especially at 0 degrees. A peak around 8 MeV is caused by

inelastic scattering from the 4.63 MeV level of ^{7}Li. The depressions at 4 MeV and 250 keV are due to elastic scattering resonances of ^{7}Li; other depressions around 1 MeV and at 450 MeV are due to the elastic resonances at 1.7 MeV, 1.3 MeV, 1 MeV and 440 keV of ^{6}Li, respectively. The energies of these peaks and dips agree within 5 % between the measurements and the predictions by those cross sections. The spectra below 10 MeV become flat with increasing the thickness.

Figure 4.3.8 show the measured neutron energy spectra grouped into five regions by energy integration to examine the angular dependence. Neutrons in those energy groups can be related to the following reactions of ^{7}Li for 14.8 MeV source neutrons:

(A) E_n > 10.7 MeV; composed of neutrons scattered by the elastic level and the inelastic level of 0.478 MeV,

(B) 6.2 MeV < E_n < 10.7 MeV; composed of neutrons scattered by the inelastic level of 4.63 MeV,

(C) 1.0 MeV < E_n < 6.2 MeV; composed of neutrons scattered by the inelastic reactions of higher and continuum levels,

(D) 252 keV < E_n < 1.0 MeV; composed of neutrons emitted by the (n,2n) reaction,

(E) 97 keV < E_n < 252 keV; composed of neutrons emitted by the (n,2n) reaction and and affected by the large resonance of 250 keV.

In the above classification, it should be noted that the 0-degree flux strongly reflects the total cross section, which directly affect neutron transmission.

From the figure, the angular dependence of the region (A) and the others show similar trends to the graphite case; the angular dependence is unchangeable for increase of the slab thickness. The fluxes of the 0.6 mfp and 2.5 mfp slabs are almost the same order except the forward flux of region (A) for the 0.6 mfp case.

From the 0.6 mfp case, it is suggested from the energy regions from 252 keV to 10.7 MeV that the scatterings by the second level of ^{7}Li (Q_2 = - 4.63 MeV) and the inelastic levels of oxygen are very isotropic.

4.3.4 Discussions

Comparison of the MCNP calculation with the experiment

The measured angular fluxes were analyzed by the MCNP[11] code, in the previous experiments. Cross sections were retrieved from FSXLIB[12] which was produced by the NJOY[13] code. The cross sections of ^{7}Li and ^{6}Li were compared between calculations using the nuclear files of JENDL-3PR1 and -3PR2. Other nuclear data were taken from JENDL-3PR1 for ^{16}O and ENDF/B-IV for Fe, Ni, Cr and Mn. Nuclide densities used were taken from Table 4.3.2 for each slab. The calculational procedures are the same as the beryllium case.

The results, calculated by the MCNP code using the nuclear data files JENDL-3PR1 and -3PR2, were compared with the measured results. Comparisons at each measuring angle are shown in Figs. 4.3.8-4.3.10 for the three slabs. The measured spectra in the energy range below 100 keV are not reliable due to the poor statistics. The energies of depressions differ slightly from the calculation, yet within the experimental error.

The results calculated by both files show fairly good agreement over the whole energy range of the spectra and for all three slabs. However, distinct differences are seen at the energies around 8 MeV and below 250 keV which correspond to neutrons emitted by the 4.63 MeV level scattering and by the (n,2n) reaction, respectively. In the former energy region, the JENDL-3PR2 agrees well but the JENDL-3PR1 underestimates the flux, while in the latter region both JENDLs slightly underestimate the flux. This difference between the two files, however, disappears with increasing the thickness as well as the graphite case.

Ratio of the calculations to the experiment

The angle and thickness dependence of the calculated-to-measured value ratio (C/E) between JENDL-3PR1 and -3PR2 is shown in Fig. 4.3.11 for the fluxes integrated by the above regions. The angular dependence of the discrepancies of the C/E is not significant. However, the discrepancy in the region (A) increase with angle for the thicker slab. On the other hand, the thickness dependence shows an improvement of the C/E for region (E) in the JENDL-3PR1 result. This also can be attributed to compensation by slowing-down neutrons from region (A) in the same way as discussed in the graphite.

The JENDL-3PR1 underestimates the flux by 30 %for regions (B) and

(E), and overestimates the flux by over 10 % for region (C). In contrast to the JENDL-3PR1, the JENDL-3PR2 shows excellent agreement except for region (A). From those tendencies of the C/E values, it may be concluded that:

(1) The JENDL-3PR1 is incorrect for the cross section of the second level, and the emission spectrum of the (n,2n) reaction. The 4.63 MeV level-scattered neutron component should increase at the angles 0 to 67 degrees. The emission spectra of the (n,2n) reaction should increase for the lower energy ranges.

(2) The JENDL-3PR2 is better than the JENDL-3PR2 because of improvement of the angular dependence of 4.63 MeV level scattering and adoption of pseudo-levels for continuum levels. (See Table 4.3.3) However, it is still inadequate. Overestimation of the 0-degree flux and its increase with the thickness suggests that the total cross section of JENDL-3PR2 should be higher. Predicted inelastic scattering at the 4.63 MeV level is still too low for large angles. Since a decrease of the elastic reaction would result in an improvement of the angular dependence for the 5.0 mfp slab, it is suggested to increase the (n,2n) cross section, so as to produce an increase in the total cross section.

4.3.5 Conclusion

Angular fluxes from lithium-oxide slabs with three thicknesses were measured at angles from 0 to 66.8 degrees in the energy region from 15 MeV to below 100 keV for 14.8 MeV incident neutrons. The corresponding fluxes were calculated by the Monte Carlo code MCNP to assess the nuclear data files JENDL-3PR1 and -3PR2.

The results of this comparison show that the JENDL-3PR2 is superior to the JENDL-3PR1 below 10.7 MeV but worse above 10.7 MeV. However, the flux below 252 keV which is contributed by the (n,2n) reaction is still deviated from the measured one. Especially at 0 degrees, the discrepancy of C/E above 10.7 MeV increase with the slab thickness.

From the view point of the integral experiment, the cross sections on lithium-oxide in the JENDL-3PR2 are sufficient for estimation of tritium production by ^{7}Li and the other threshold reactions in a fusion blanket design. However, the total or elastic

cross section of ^{7}Li is insufficient where the JENDL-3PR1 is conversely better at 0 degrees. Since the C/E deviation due to the error in the total cross section is multiplied by mean free path with increasing the penetration length, the total cross sections of ^{7}Li and oxygen should be evaluated with an accuracy less than 1 % especially for estimation of the tritium breeding ratio.

References

1) Abdou M. A.: "Tritium Breeding in Fusion Reactors," ANL/FPP/TM-165, Argonne National Laboratory, (1982)
2) Houge H. H.: et al., Nucl. Sci. Eng., 69, 22 (1979)
3) Baba M., et al., " Neutron Scattering from ^{7}Li at Incident Energies of 5.1, 6.6 and 15.4 MeV," Proc. Int. Conf. Nuclear Cross Sections for Technology, Knoxiville, 1979, pp.43 (1980)
4) Takahashi A., et al.: J. Nucl. Sci. Technol., 21 , 577 (1984)
5) Chiba S., et al.: ibid., 22, 771 (1985)
6) Shibata K. and Kikuchi Y.: " Evaluation of Nuclear Data for Fusion Neutronics," Proc. Int. Conf. Nuclear Data for Basic and Applied Science ," Santa Fe, New Mexico, 1985, pp.1585 (1986)
7) Shibata K.: "Evaluation of Neutron Data of ^{6}Li for JENDL-3," JAERI-M 84-198 (1984)
8) idem.: "Evaluation of Neutron Data of ^{7}Li for JENDL-3," JAERI-M 84-204 (1984)
9) Sako K., et al.: "Conceptual Design of a Gas-Cooled Tokamak Reactor," Proc. Symp. Fusion Reactor Design Problems, CONF-740131, pp.27-49, IAEA (1974); see also JAERI-M 5502 (1973)
10) Oyama Y., et al.: "Measurement of Angle-Dependent Neutron Spectra from Lithium-Oxide Slab Assemblies by Time-of-Flight Method," JAERI-M 83-195 (1983)
11) Los Alamos Radiation Transport Group (X-6): "MCNP-A General Monte Carlo Code for Neutron and Photon Transport," LA-7396-M, Los Alamos National Laboratory Revised (April 1981)
12) Kosako K.: private communication (1987); "Cross Section Libraries for Analysis of Experiment at FNS," to be published in JAERI-M report
13) MacFarlane R.E., et al.: "The NJOY Nuclear Data Processing System: User's Manual," LA-7584-M (ENDF/-272) (1978)

Table 4.3.1 Chemical analysis of Li_2O bricks.

Element	Content (%) $
Li	> 99.8
Na	< 0.001
K	< 0.003
Ca	0.01
Al	0.011
Si	0.016
Fe	0.011

$ weight %

Molecule	Content (%) $
LiOH	< 0.1
Li_2CO_3	< 0.1

$ weight %

Isotopic Contents	
^6Li	7.406 ± 0.003 atom %
^7Li	92.594 ± 0.003 atom %

Table 4.3.2 Homogenized atomic densities of the compositions of Li_2O assembly

Material	Element	Atomic Density (x 10^{24} atoms/cm^3)	
		48 mm Assembly	200/400 mm Assembly
Li_2O	^7Li	5.3379-2*	5.3707-2
	^6Li	4.2782-3	4.3044-3
	O	2.8829-2	2.9006-2
stainless steel	Fe	1.5571-3	1.0976-3
	Ni	1.8369-4	1.2948-4
	Cr	4.2231-4	2.9769-4
	Mn	3.3091-5	2.3326-5

* read as 5.3379 x 10^{-2}

Table 4.3.3 Lithium-7 cross section for 15 MeV neutrons in the nuclear files

Reaction	JENDL-3PR1	JENDL-3PR2
total	1422 mb	1379.4 mb
elastic	1023 mb	980.6 mb
inelastic		
0.478 MeV	56.1 mb	56.1 mb
4.63 MeV	79.8 mb	79.8 mb
continuum	183.0 mb	24 pseudo-levels from 2.5 to 13 MeV 186.8 mb
(n,2n)	70.1 mb	70.1 mb

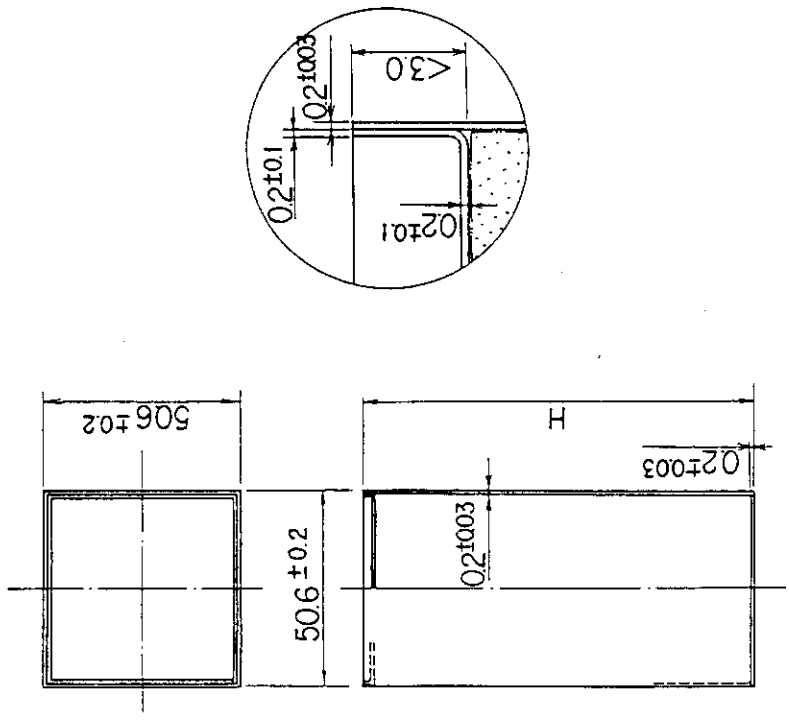

Fig. 4.3.2 Dimensions and structure of the lithium-oxide block.

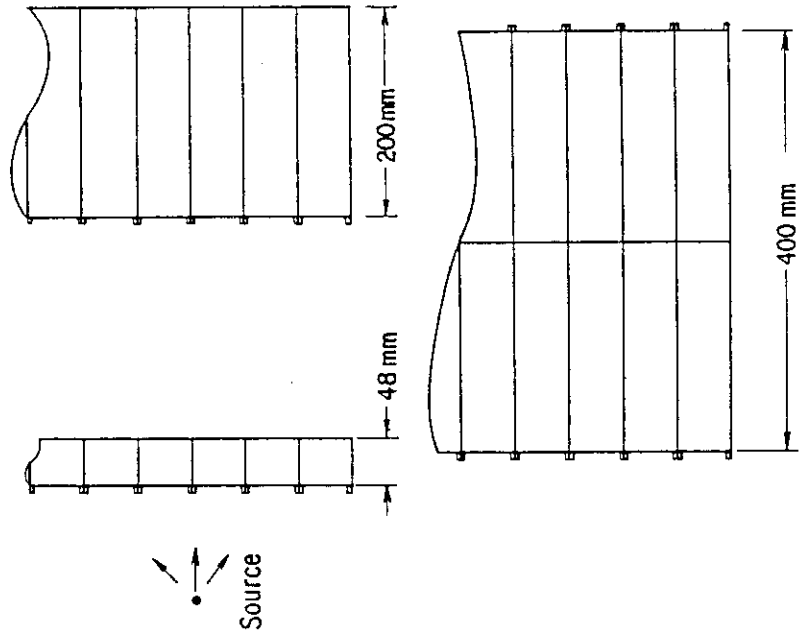

Fig. 4.3.1 Configuration of lithium-oxide blocks for three slabs.

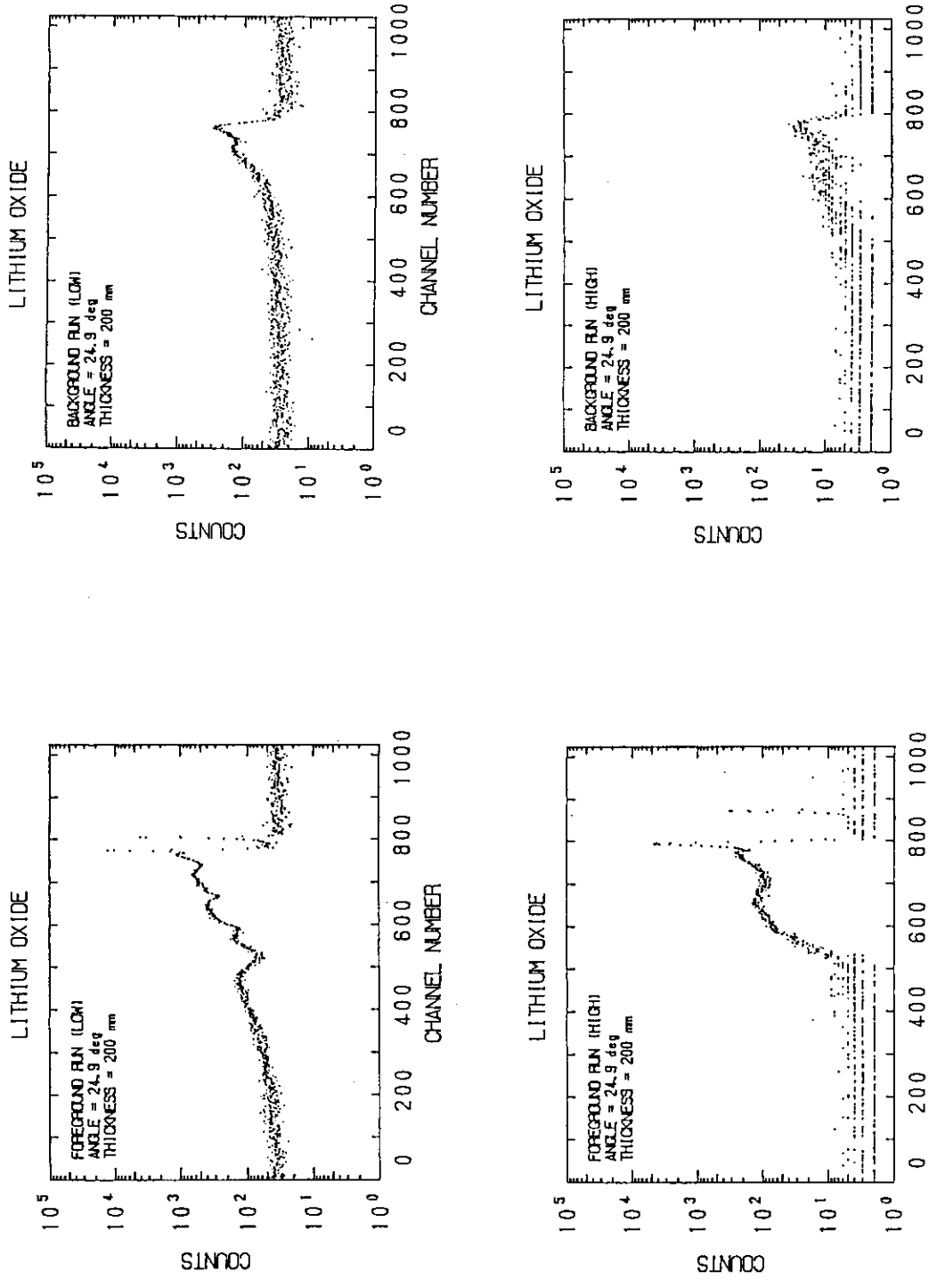

(a) foreground run (b) background run

Fig. 4.3.3 Typical time spectra observed on the lithium-oxide slab

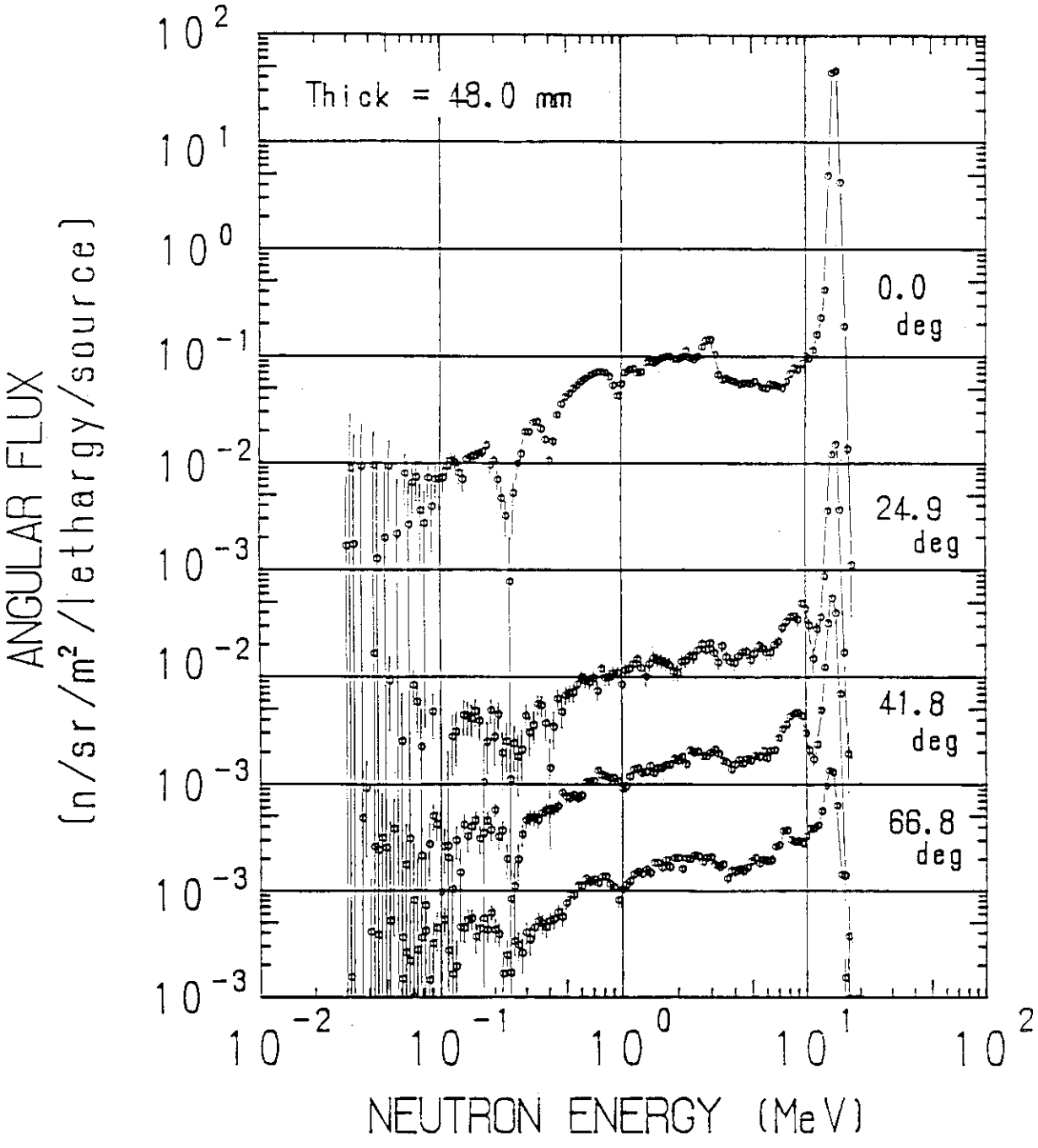

Fig. 4.3.4 Measured spectra of angular flux for the 48.0 mm-thick lithium-oxide assembly. Error bar includes only statistical error due to neutron counts.

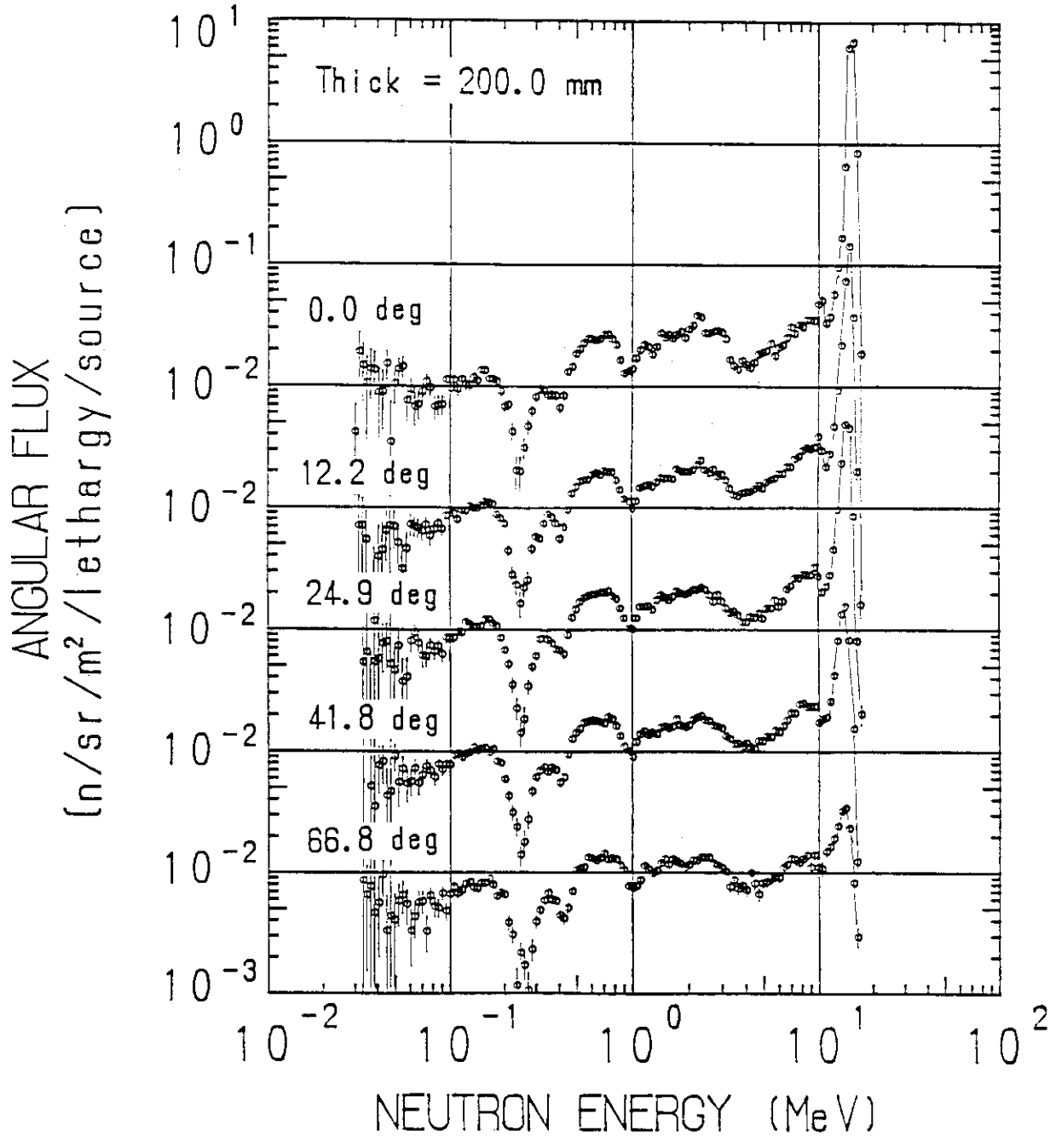

Fig. 4.3.5 Measured spectra of angular flux for the 200.0 mm-thick lithium-oxide assembly. Error bar includes only statistical error due to neutron counts.

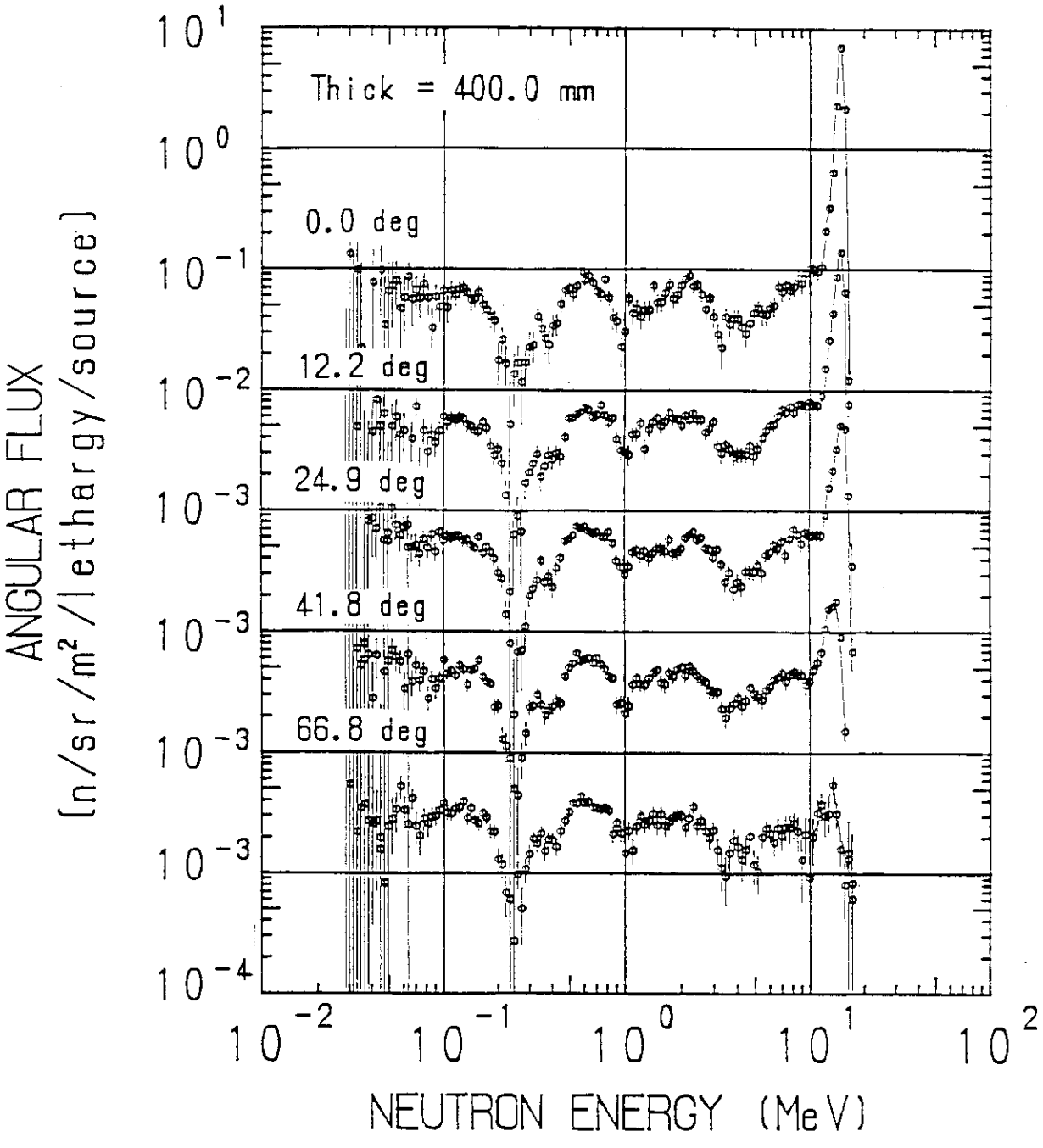

Fig. 4.3.6 Measured spectra of angular flux for the 400.0 mm-thick lithium-oxide assembly. Error bar includes only statistical error due to neutron counts.

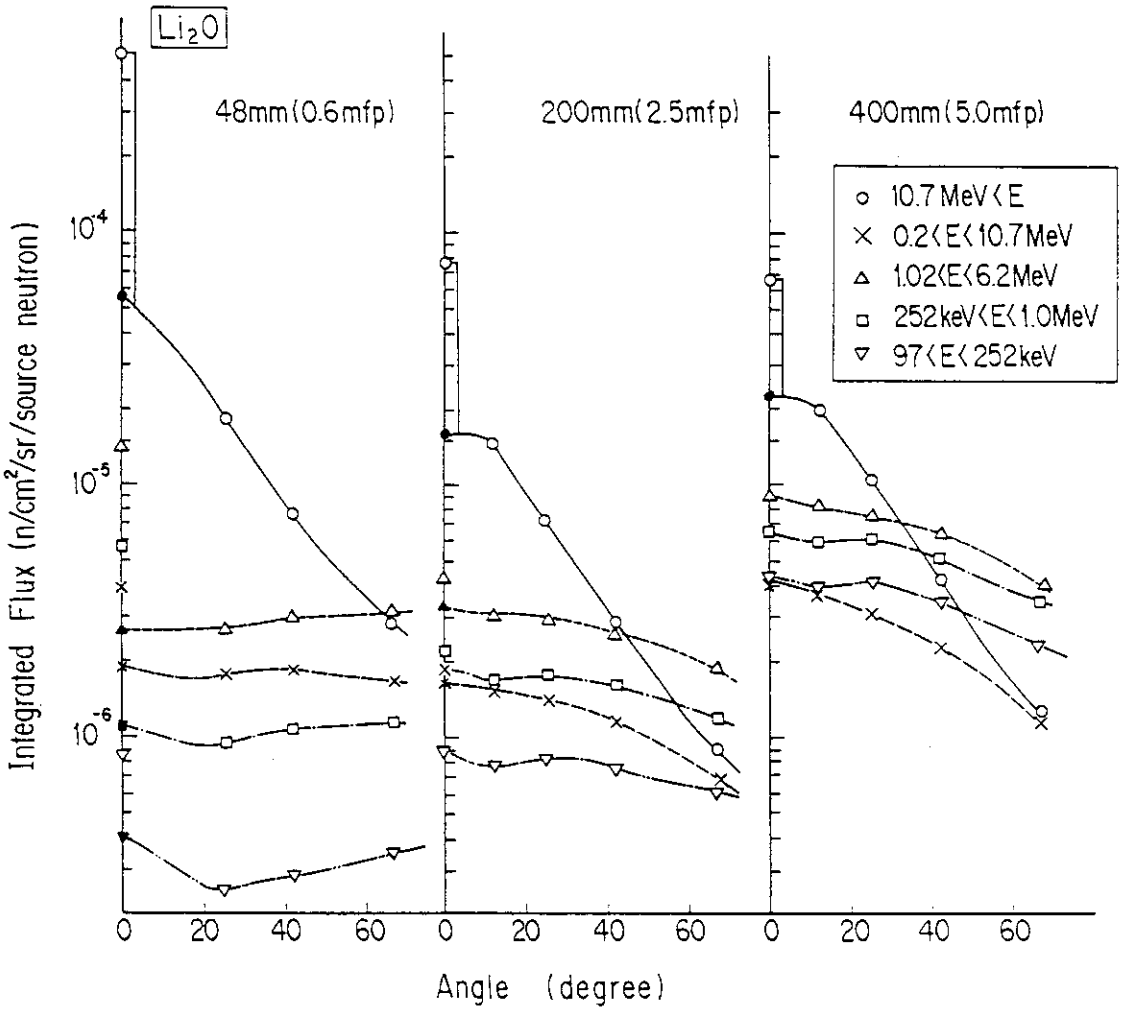

Fig. 4.3.7 Measured flux integrated over four energy ranges vs. measuring angle. Black symbols show the collided flux: The uncollided flux calculated by the MCNP code is subtracted from the measured value. Lines are only for eye-guide.

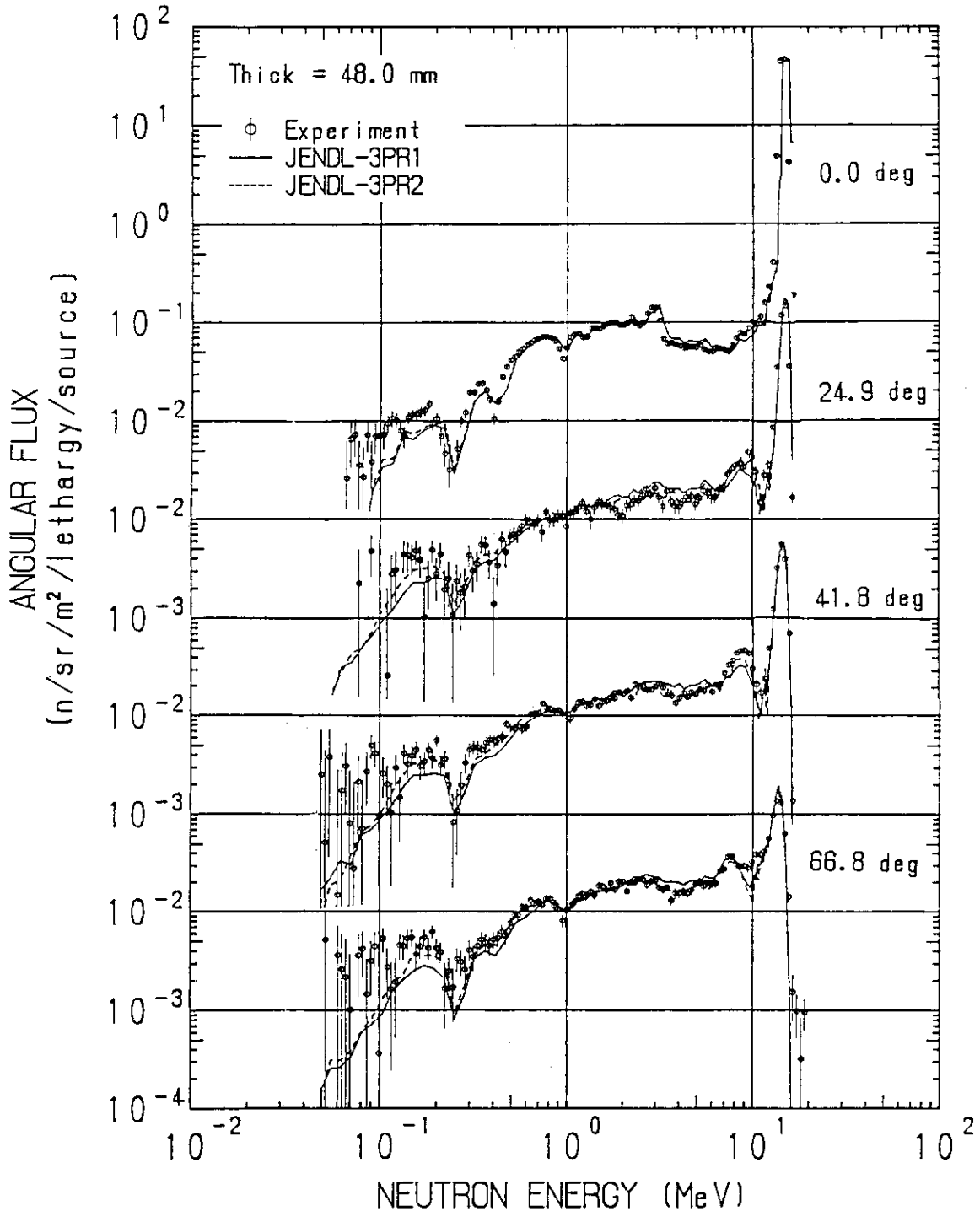

Fig. 4.3.8 Comparison of the experiment with the calculated spectra for the 48.0 mm-thick slab.

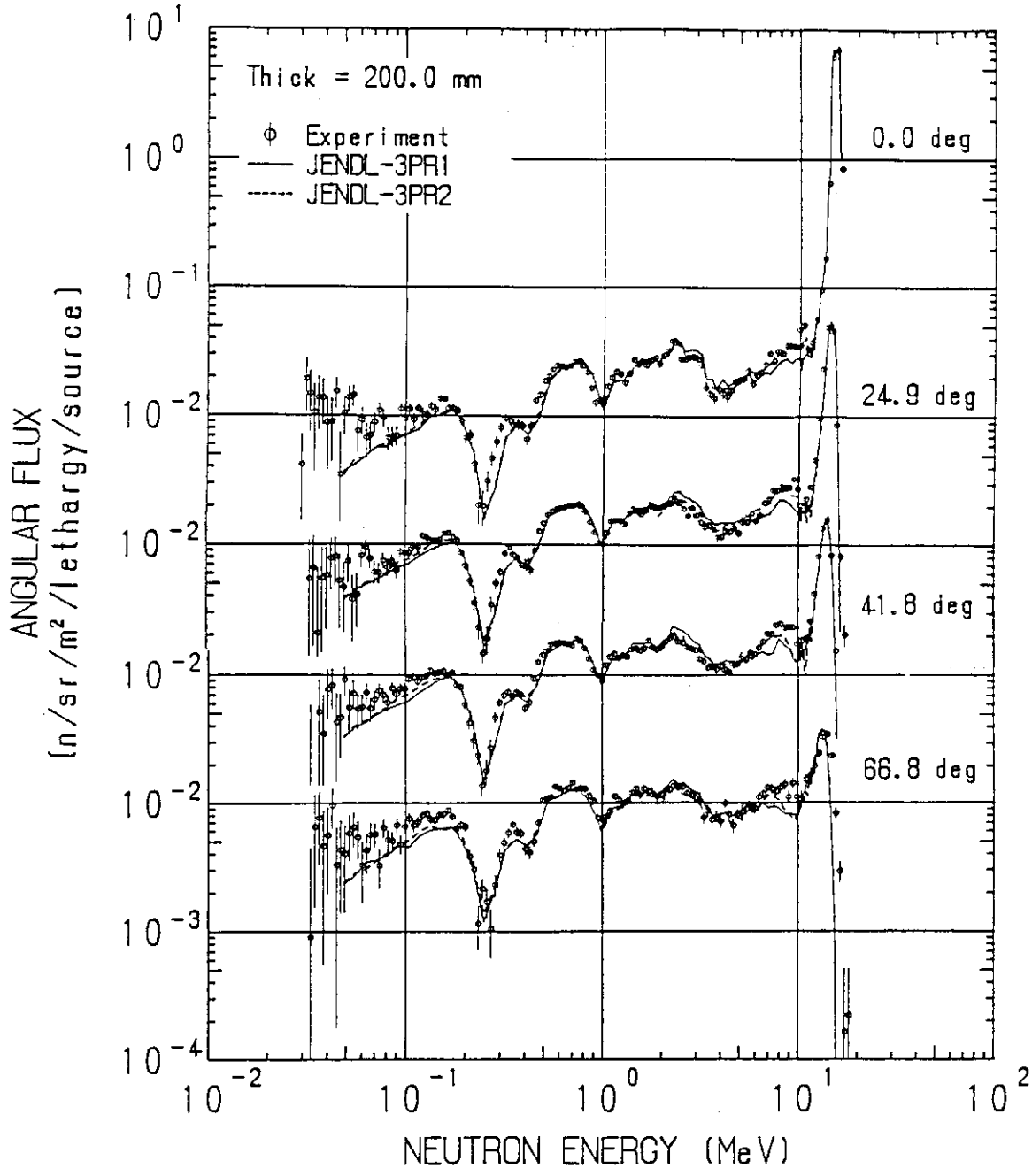

Fig. 4.3.9 Comparison of the experiment with the calculated spectra for the 200.0 mm-thick slab.

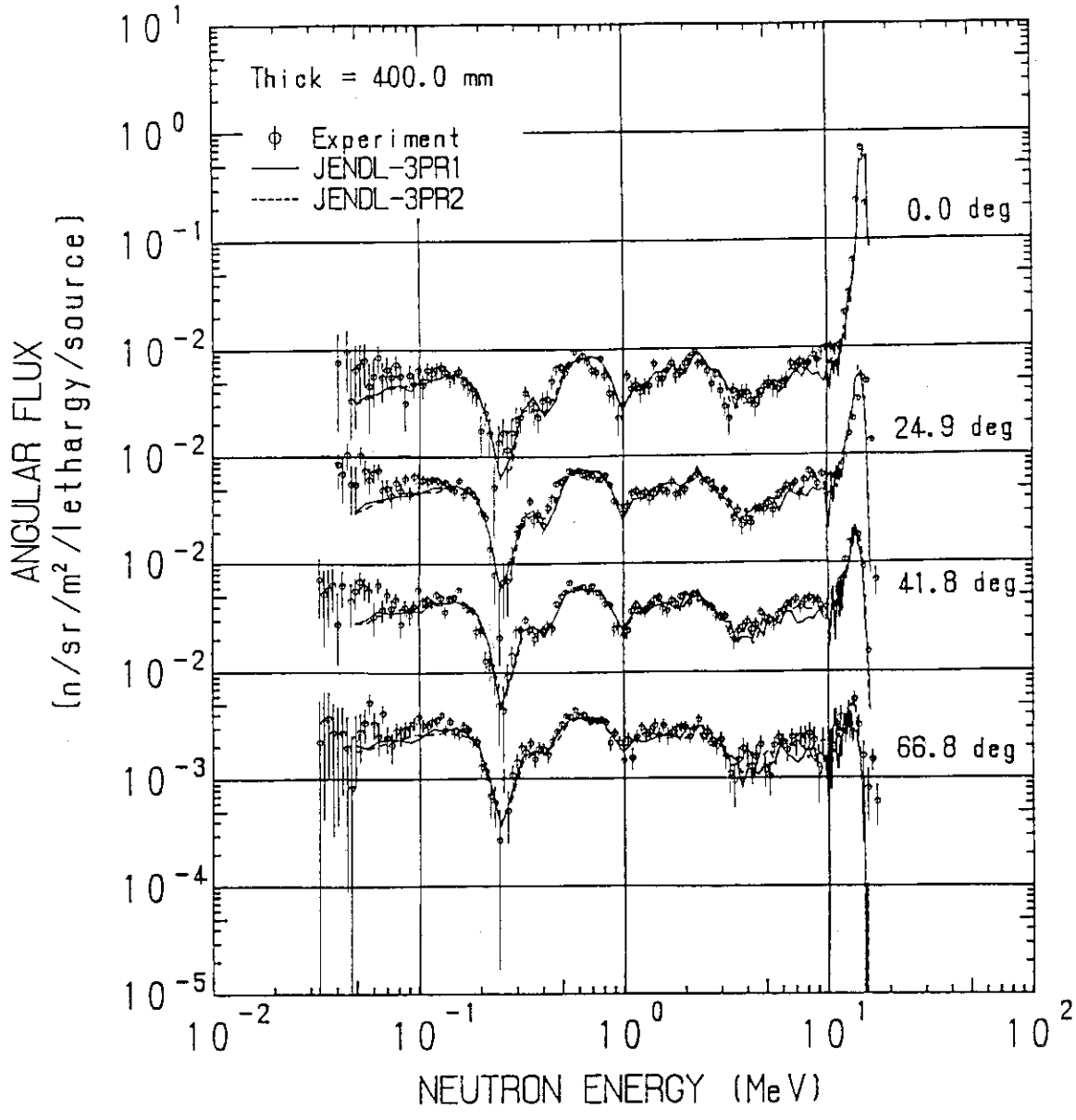

Fig. 4.3.10 Comparison of the experiment with the calculated spectra for the 400.0 mm-thick slab.

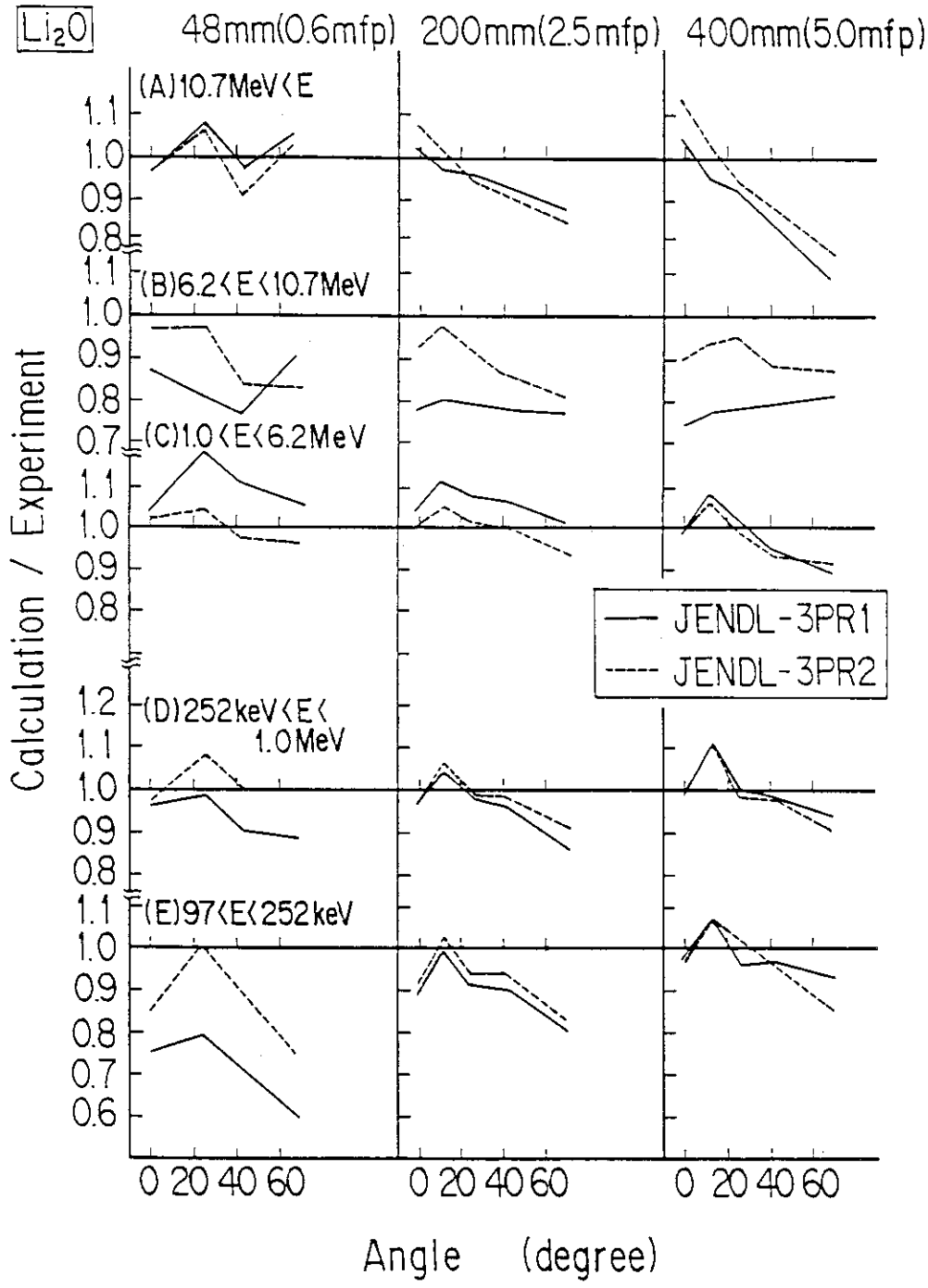

Fig. 4.3.11 Ratios of the calculated-to-measured values as functions of the thickness and the angle for various nuclear data files. Energy regions are (A) above 10.7 MeV, (B) 6.2< E < 10.7 MeV, (C) 1.0 < E < 6.2 MeV, (D) 252 keV < E < 1.0 MeV and (E) 97 < E < 252 keV.

APPENDIX Calculational Models for Analyses

A.Model for MORSE-DD Calculations

The point detector estimator and angular flux options were used in the calculations by the MORSE-DD code. This calculational model is shown in Fig. A.1.1 The detector was set at the same distance from the assembly as the experimental arrangement. The detector position was fixed on the z-axis and the neutron source and assembly were rotated according to the measuring angle.

By definition in Fig. A.1

$$\phi_{cal} = N/(\Delta\Omega' \cdot S_n), \qquad (A.1.1)$$

where $\Delta\Omega' = A_s/L^2$, and N = neutrons passing through the point P. Replacing A_d/L^2 by the solid angle $\Delta\Omega$ subtended by the detecting area A_d to the center of the assembly,

$$\phi_{cal} = (N \cdot A_d)/(\Delta\Omega \cdot S_n \cdot A_s). \qquad (A.1.2)$$

Thus the calculated flux in this model is exactly equivalent to the definition of the measured flux. Note that the calculation excludes the air-attenuation effect, since the experimental results were already corrected for this attenuation.

B.Model for MCNP Calculations

The point detector estimator was also used in the MCNP calculations, and the calculations for 5 angles were done simultaneously with the model as shown in Fig. A.2 Since the definition of the effective measured area, A_s, described in chap. 3, includes the scattered-neutron and the dull-edge effects of the collimator, the detector-collimator system can be simulated effectively by an ideal collimator with an aperture A_s and a point detector. This ideal collimator was modeled by no-importance regions in which neutron histories were immediately terminated. This region surrounded a cylinder with radius corresponding to the effective measured area A_s. The calculated flux was reduced to the measured quantity by multiplying L^2/A_s for each detector position.

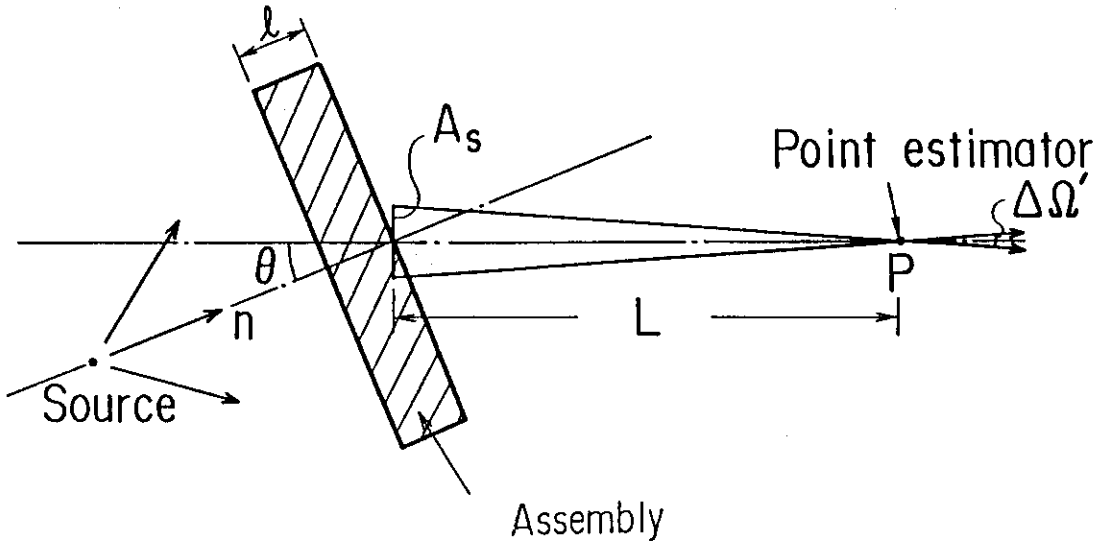

Fig. A.1 Model for the MORSE-DD calculations. The detector is set on the z axis, and the source and the slab assembly are rotated corresponding to the angle of the measured flux.

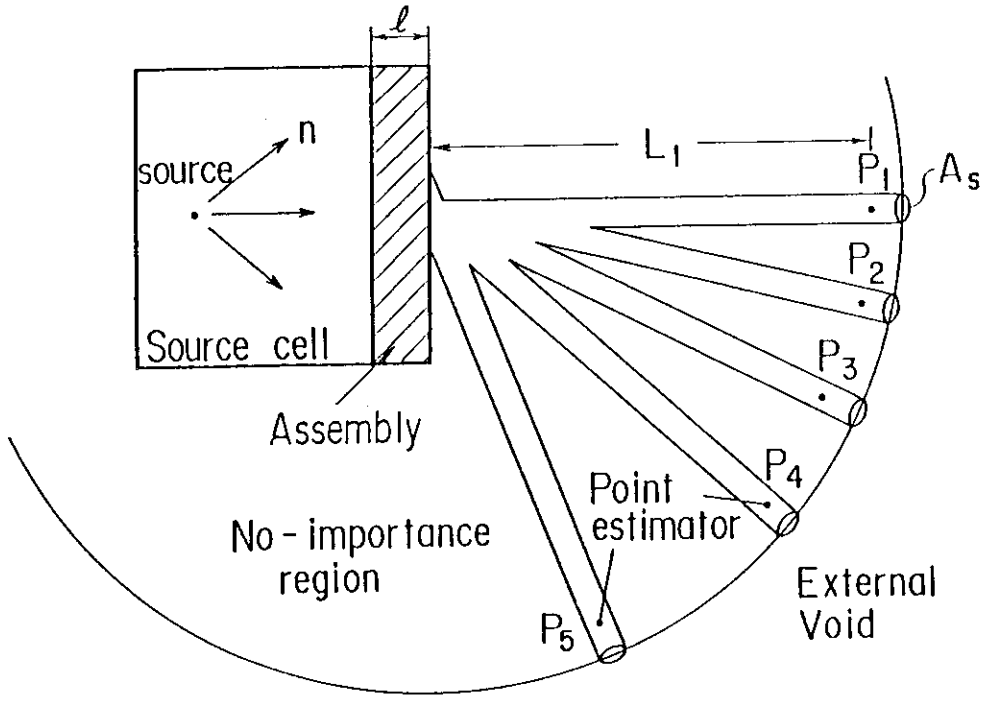

Fig. A.2 Model for the MCNP calculations. The five detectors are located at the same time, and the no-importance region

5. Conclusions

An experimental method for measuring the angular neutron flux emitted from the rear surface of cylindrical slabs of varying thickness, was developed and the current nuclear data files and Monte Carlo calculation system were assessed to through comparison between the measured and calculated results. The experimental arrangement was specifically designed to identify the cross sectional error affecting the neutron transport in the bulk material. General characteristics of the angular flux examined by Monte Carlo calculations and analysis of flux contributions showed that: the angular flux for a thin slab represented the second emission spectra of the initial reaction of the 14.8 MeV incident neutrons; and the internal neutron flux closely related to the angular dependence of the angular flux.

A neutron time-of-flight system was used to measure the energy spectrum of the angular flux in the energy range below 100 keV. In order to obtain the efficiency accurately for a wide energy range, the neutron detection with an NE213 scintillation detector was implemented by a novel 'two-bias' method, which excluded carbon response for neutron detection. Effectiveness of the method was verified by a measurement of low-energy neutrons emitted from a graphite pile.

The detector shield and collimator were designed to limit the measurement in the central area of the rear surface of slab. The effective measured area was determined by a calculation and confirmed experimentally using the DT neutron source and the ^{252}Cf source.

The angular fluxes were measured for graphite, beryllium and lithium-oxide slabs. The measurements were carried out for two or three thicknesses at five angles (0, 12.2, 24.9, 41.8 and 66.8 degrees). the result of measurements was compared with that of calculations with the Monte Carlo code MCNP or MORSE-DD which simulates the experimental assembly and facilitates direct examination of the nuclear data files.

The newly evaluated nuclear data files, JENDL-3PR1 and -3PR2, were assessed through comparison with the other files, e.g., ENDF/B-IV as follows:

1) Carbon: the JENDL's data on elastic, and the 2nd and 3rd inelastic reactions showed large discrepancies at 20-40 degrees. The inelastic cross section data of ENDF/B-V was

better.

2) Beryllium: the discrepancies of JENDL-3PR1 were ranging in 20-30 % as a whole. Discrepancies for high-energy neutrons can be attributed to the incorrectly represented angular dependence of the elastic reaction. Representation of the inelastic level of 6.76 MeV also provided inadequate spectrum.
3) Lithium and oxygen in the Lithium-oxide, the JENDL-3PR2 showed an improvement compared with the JENDL-3PR1. However, the total cross section of JENDL-3PR2 was worse than that of the JENDL-3PR1.

From a view points of a fusion reactor design, it is pointed out on the present evaluated nuclear data JENDLs and Monte Carlo calculation that:

1) The calculational predictions of neutronic parameters related to high threshold reactions for graphite will give 5 % agreement with the experiment.
2) For lithium-oxide, the the JENDL-3PR1 might give good results for the neutronic parameters because of lower total cross section of the JENDL-3PR2.
3) For beryllium, the data has still much problems at present. It should be re-evaluated.

To sum up, a series of the measurements of the neutron angular flux as functions of thickness and angle on a slab assembly produced much information of neutron transport which could not be obtain from a neutron transmission experiment. Moreover, a diagram of thickness and angle dependence for the integrated flux in the interested energy regions were very useful to judge the validity of nuclear data files and calculational method used in a fusion reactor design. In addition, the required accuracies will be clarified from a practical view point for the design. Thus, the data obtained here can be very useful for a benchmark test of the new evaluated nuclear data file JENDL-3 being compiled in 1988.

Acknowledgments

The author thanks Dr. Hiroshi Maekawa who led the author to become interested in the time-of-flight experiment, for his valuable advice on the thesis, to Mr. Seiya Yamaguchi who collaborated on the works with the present author, to Mr. Tomoo Nakamura, Head of Fusion Reactor Physics Laboratory, who always encouraged the author in the study, and to the seniors of the Department of Reactor Engineering, JAERI, who have supported all of the present works.

The author wish to express his gratitude to Professor Kenji Sumita of Osaka University for his guidance and incessant advice in the course of this thesis work. The author also would like to express his appreciation to Professors Tamotsu Sekiya and Noriaki Takahashi of Osaka University for their valuable comments, suggestive discussions, and critical reading of the thesis.

The author is indebted to many people in the course of the present study and would like to express his gratitude to them, especially to Messrs. Kazuaki Kosako and Tooru Fukumoto for assistance of use of computer codes, to Drs. Tomoo Suzuki, Yasushi Seki, Masayuki Nakagawa and Takamasa Mori for their valuable discussions on the points of calculational analysis, and to Drs. Shun-ichi Tanaka and Yujiro Ikeda for making necessary equipments available and for suggestions on the experimental points. To Professor Akito Takahashi and Dr. Junji Yamamoto of Osaka University the author gratefully acknowleges their kind, beneficial, and critical suggestions of the work.

The author greatly appreciates excellent operations and maintenance of the machines at the FNS facility by the staffs, especially by Messrs. Joichi Kusano, Chuzo Kutsukake, Shigeru Tanaka and Yuji Abe.

In addition, thanks are also due to Dr. Karl Porges of Argonne National Laboratory for his careful reading of English manuscript, and to Misses Noriko Sootome, Miyako Noguchi and Akemi Endou for their help in typing and compiling the manuscript.